

AD-A159 228

EXPLORATORY DEVELOPMENT ON ADVANCED EDDY CURRENT COIL  
EXCITATION AND SIGN. (U) SOUTHWEST RESEARCH INST SAN  
ANTONIO TX J L FISHER ET AL. APR 85 AFMNL-TR-85-4025

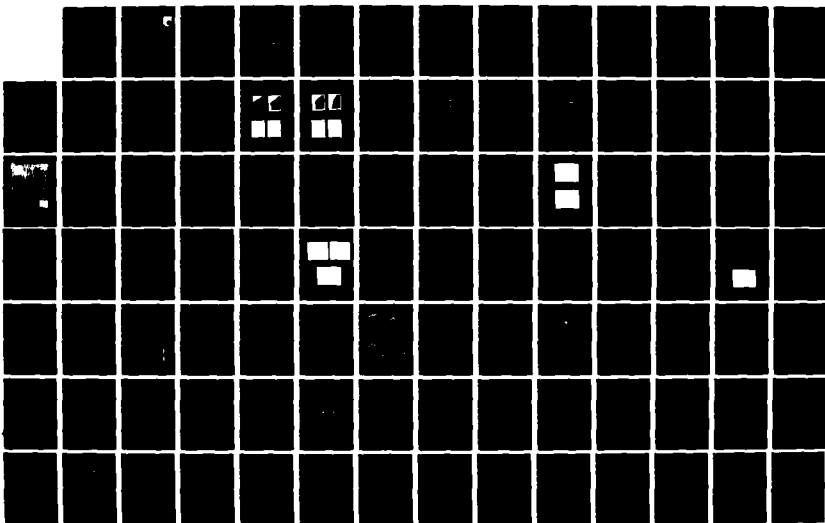
272

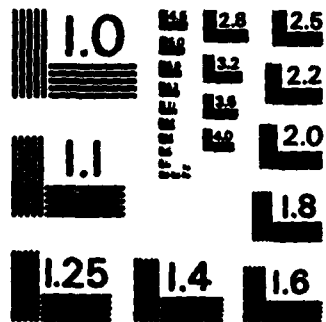
UNCLASSIFIED

F33615-81-C-5036

F/G 14/2

NL





MICROCOPY RESOLUTION TEST CHART  
NATIONAL BUREAU OF STANDARDS - 1963 - A

AD-A159 228

(2)

AFWAL-TR-85-4025

EXPLORATORY DEVELOPMENT ON ADVANCED EDDY CURRENT  
COIL EXCITATION AND SIGNAL PROCESSING



Jay L. Fisher  
Dr. R. E. Beissner  
James E. Doherty

Southwest Research Institute  
6220 Culebra Road  
San Antonio, Texas 7824

April 1985

Approved for public release; distribution unlimited.

MATERIALS LABORATORY  
AIR FORCE WRIGHT AERONAUTICAL LABORATORIES  
AIR FORCE SYSTEMS COMMAND  
WRIGHT-PATTERSON AIR FORCE BASE, OHIO 45433

DTIC  
ELECTE  
SEP 18 1985  
S  
A A

DTIC FILE COPY

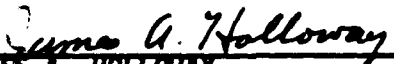
85 09 18 001

**NOTICE**

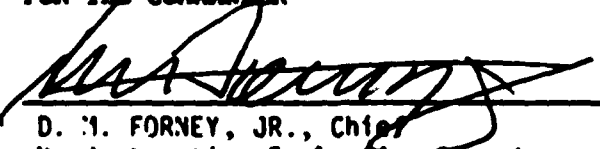
When Government drawings, specifications, or other data are used for any purpose other than in connection with a definitely related Government procurement operation, the United States Government thereby incurs no responsibility nor any obligation whatsoever; and the fact that the government may have formulated, furnished, or in any way supplied the said drawings, specifications, or other data, is not to be regarded by implication or otherwise as in any manner licensing the holder or any other person or corporation, or conveying any rights or permission to manufacture use, or sell any patented invention that may in any way be related thereto.

This report has been reviewed by the Office of Public Affairs (ASD/PA) and is releasable to the National Technical Information Service (NTIS). At NTIS, it will be available to the general public, including foreign nations.

This technical report has been reviewed and is approved for publication.

  
\_\_\_\_\_  
JAMES A. HOLLOWAY  
Nondestructive Evaluation Branch  
Metals and Ceramics Division

FOR THE COMMANDER

  
\_\_\_\_\_  
D. I. FORNEY, JR., Chief  
Nondestructive Evaluation Branch  
Metals and Ceramics Division

"If your address has changed, if you wish to be removed from our mailing list, or if the addressee is no longer employed by your organization please notify AFMIL/MLLP, W-PAFB, OH 45433 to help us maintain a current mailing list".

Copies of this report should not be returned unless return is required by security considerations, contractual obligations, or notice on a specific document.

**REPORT DOCUMENTATION PAGE**

1a. REPORT SECURITY CLASSIFICATION <b>UNCLASSIFIED</b>		1b. RESTRICTIVE MARKINGS	
2a. SECURITY CLASSIFICATION AUTHORITY		3. DISTRIBUTION/AVAILABILITY OF REPORT Approved for public release; distribution unlimited.	
2b. DECLASSIFICATION/DOWNGRADING SCHEDULE			
4. PERFORMING ORGANIZATION REPORT NUMBER(S)		5. MONITORING ORGANIZATION REPORT NUMBER(S) AFI/AL-TR-85-4025	
6a. NAME OF PERFORMING ORGANIZATION Southwest Research Institute	6b. OFFICE SYMBOL (If applicable)	7a. NAME OF MONITORING ORGANIZATION AFI/AL/MLLP	
6c. ADDRESS (City, State and ZIP Code) 6220 Culebra Road San Antonio, TX 78284		7b. ADDRESS (City, State and ZIP Code) Wright-Patterson AFB, OH 45433-6533	
8a. NAME OF FUNDING/SPONSORING ORGANIZATION	8b. OFFICE SYMBOL (If applicable)	9. PROCUREMENT INSTRUMENT IDENTIFICATION NUMBER F33615-81-C-5036	
8c. ADDRESS (City, State and ZIP Code)		10. SOURCE OF FUNDING NOS.	
		PROGRAM ELEMENT NO. 62102F	PROJECT NO. 2418
		TASK NO. 05	WORK UNIT NO. 16
11. TITLE (Include Security Classification) <b>EXPLORATORY DEVELOPMENT ON ADVANCED EDDY CURRENT COIL EXCITATION AND SIGNAL PROCESSING (II)</b>			
12. PERSONAL AUTHOR(S) Fisher, Jay L., Beissner, Dr. R. E., Doherty, James E.			
13a. TYPE OF REPORT Final Report	13b. TIME COVERED FROM 9 Jan 81 to 9 Jan 84	14. DATE OF REPORT (Yr., Mo., Day) 1985 Oct	15. PAGE COUNT 131
16. SUPPLEMENTARY NOTATION			
17. COBATI CODES		18. SUBJECT TERMS (Continue on reverse if necessary and identify by block number)	
FIELD	GROUP	SUB GR.	Nondestructive evaluation; pulsed eddy current; surface and subsurface flaws. <i>ef</i>
20	0	3	
11	0	6	
19. ABSTRACT (Continue on reverse if necessary and identify by block number)			
<p>The purpose of this program was to achieve improvements in eddy current performance by analytical and experimental exploratory development of the pulse mode of coil excitation as a means of evaluating surface and near-surface defects in low-conductivity materials used in gas turbine engine components.</p> <p>The program successfully demonstrated that the pulsed eddy current approach is capable of detecting flaws as small as 0.010 inch by 0.005 inch in a T1-6-4 surface. In addition results indicate that this approach offers a promising way to estimate the depth of surface-breaking flaws.</p>			
20. DISTRIBUTION/AVAILABILITY OF ABSTRACT UNCLASSIFIED/UNLIMITED <input checked="" type="checkbox"/> SAME AS RPT. <input type="checkbox"/> DTIC USERS <input type="checkbox"/>		21. ABSTRACT SECURITY CLASSIFICATION UNCLASSIFIED	
22a. NAME OF RESPONSIBLE INDIVIDUAL <i>James G. Holloway</i> J. A. Holloway		22b. TELEPHONE NUMBER (Include Area Code) (513) 255-5309	22c. OFFICE SYMBOL AFI/AL/MLLP



## TABLE OF CONTENTS

	<u>Page</u>
<b>LIST OF ILLUSTRATIONS</b> . . . . .	iv
<b>1. INTRODUCTION AND SUMMARY</b> . . . . .	1
1.1 Background . . . . .	1
1.2 Objectives . . . . .	2
1.3 Summary of Results . . . . .	3
1.4 Report Summary . . . . .	3
<b>2. BREADBOARD SYSTEM DEVELOPMENT</b> . . . . .	5
2.1 System Description . . . . .	5
2.2 Flaw Specimens . . . . .	5
2.3 Flaw Detection Experiments . . . . .	7
2.4 Evaluation Results . . . . .	7
2.5 Additional Probe Development . . . . .	12
<b>3. MODEL DEVELOPMENT AND EXPERIMENTAL VERIFICATION</b> . . . . .	19
3.1 Introduction . . . . .	19
3.2 Effects of Probe Geometry . . . . .	19
3.3 Effects of Flaw Geometry . . . . .	23
3.4 Comparison with Experiment-Zero Crossing . . . . .	23
3.5 Slot Tip Effects - Theory . . . . .	31
3.6 Slot Tip Effects - Experiments . . . . .	36
3.7 Conclusion . . . . .	39
<b>4. ADVANCED SYSTEM DESIGN</b> . . . . .	42
4.1 Breadboard Development . . . . .	42
4.2 Probe Development . . . . .	44
4.3 Evaluation Results . . . . .	50
<b>5. COMPARISON WITH C-W RESULTS</b> . . . . .	54
<b>6. CONCLUSIONS AND RECOMMENDATIONS</b> . . . . .	61
<b>7. REFERENCES</b> . . . . .	62

### APPENDICES

- A Analytical Models
- B An Alternative Approach for Computing Eddy Currents:  
    Case of the Double-Layered Plate
- C Probe Design Studies
- D Voltage to Current Converter
- E Flaw Specimens

## LIST OF ILLUSTRATIONS

<u>Figure</u>		<u>Page</u>
1	A Pulsed Eddy Current Test System . . . . .	6
2	Transmitted Pulse Shape and Frequency Spectrum as a Function of Pulse Rise Time . . . . .	8
3	Detector Scans from Ti 6-4 Block with EDM Notches . . . . .	10
4	Edge Resolution Scans from a Ti 6-4 Block with EDM Notches . . . . .	11
5	Spatial Resolution Scans from Ti 6-4 Block with 1.25 x .9 mm EDM Notches . . . . .	13
6	Change in Inductance of a Ferrite Core Coil with Different Shielding Material . . . . .	14
7	Improved Ferrite-Wound, Not-to-Scale, Ferrite- and Copper-Shielded Probe with Cylindrical Symmetry . . . . .	17
8	Toroidal-Wound Probe . . . . .	17
9	Comparison of Normal Component of Magnetic Field in Air . . . . .	18
10	Simplified Model of Pulsed Eddy Current Probe . . . . .	20
11	Geometry for Detailed Model . . . . .	21
12	Comparison of Calculated and Measured Fields from a Pulsed Eddy Current Coil in Air . . . . .	22
13	Calculated Signals from <u>Point Flaws</u> at Various Depths Below the Surface for a 1 nsec Gaussian Pulse . . . . .	24
14	Point Flaw Signal Peak Amplitude as a Function of Flaw Depth for Different Pulse Widths . . . . .	25
15	Confirmation of the Existence of a Liftoff-Insensitive Amplitude Crossing Point . . . . .	27
16	Calculated Response Function for a .25 x .15-mm (10 x 5-mil) Slot . . . . .	29
17	Calculated Response Function for a 1.0 x .50-mm (40 x 20-mil) Slot . . . . .	29

**LIST OF ILLUSTRATIONS (Cont'd)**

<u>Figure</u>		<u>Page</u>
18	Calculated and Measured Zero-Crossing Times as a Function of Flaw Depth . . . . .	31
19	Flaw Response Based on an Integrated Point Flaw Model . .	33
20	Flaw Response Based on a Crack Tip Model, for the Same Input Pulse as Used in Figure 18 . . . . .	34
21	Signal Propagation Paths for Open and Closed Cracks . . .	35
22	Received Pulse in the Absence of a Flaw (a) Received Pulse With Probe Positioned to Maximize the Flaw Signal (b) . . . . .	37
23	Flaw Signal Peak Arrival Time Vs Flaw Depth as Measured (x's) Agrees With the time Required for an Eddy Current Pulse to Diffuse to the Crack Tip (solid curve) . . . . .	38
24	Ideal Current Waveforms for Achieving Time-Domain Separation of Surface Signals and Flaw Depth Information . . . . .	40
25	Modified Pulsed Eddy Current Test System . . . . .	43
26	Input Voltage Waveform (Bottom Trace) and Output Current Waveform (1 Ampere per Division) of the Voltage-to-Current Amplifier . . . . .	44
27	Probe Current (Upper Trace) Follows Input Voltage (Lower Trace) Better When a Probe With a Higher Resonant Frequency [(b), 14.3 MHz] Probe is Used than When a Lower Resonant Frequency Probe [(a), 6 MHz] is used . . . . .	45
28	The Variation of Observed Inductance of a Single Transmitter Coil as a Function of Frequency When Measured with Short Leads and with 2 Feet of Different Coaxial Cables . . . . .	47
29	Actual Current Waveform and Power Spectrum Obtainable with a 10-MHz Probe . . . . .	48
30	Magnitude of the Fourier Transform of the Ideal Transmitter Current Waveform T is the Duration of the Ramp Portion . . . . .	49
31	No-Flaw Receiver Signal Used in a Series of Flaw Depth Measurement Tests . . . . .	51

LIST OF ILLUSTRATIONS (Cont'd)

<u>Figure</u>		<u>Page</u>
32	Receiver Flaw Minus No-Flaw Signal, for Different Depth Notches . . . . .	52
33	Inverse of the Slope of the Decay Portion of Flaw Waveforms Shown in Figure 32 . . . . .	53
34	Conventional Eddy Current Scans of Flaws A Through D on the Surface Flaw Detection Standard (E Is Not Detectable) . . . . .	55
35	Plan View Representation of the Vertical (Minimum Liftoff Effect) Component of the Impedance Plane Display for the Same Flaws as in Figure 34 . . . . .	56
36	Plan View Representation of the Vertical (Minimum Liftoff Effect) Component of the Impedance Plane Display for Flaws G, H, I, and J . . . . .	58
37	Peak Vertical Signal Response from Conventional Eddy Current Examination . . . . .	59
38	Conventional Eddy Current Scan of the Same Flaws as in Figure 36 Using an Air-Bearing Probe Developed by SwRI for RFC . . . . .	60
39	Simplified Model of Pulsed Eddy Current Probe . . . . .	65
40	Field Calculated 0.025 mm in Front of the Model Probe Shown in Figure 39 . . . . .	66
41	Time-Dependent Field Alongside a Probe with a 0.25-mm Thick Shield . . . . .	68
42	Comparison of the Analytic Approximation to the Exact Expression of Current Density . . . . .	71
43	Geometry Used in Probe Design Studies . . . . .	80
44	Effect of the Ferrite Core Size . . . . .	81
45	Effect of the Coil-to-Shield Distance . . . . .	82
46	Effect of the Transmitter Liftoff . . . . .	83
47	Effect of the Copper Shield . . . . .	84

LIST OF ILLUSTRATIONS (Cont'd)

<u>Figure</u>		<u>Page</u>
48	Flaw Response Functions for Differential Sensors . . . .	85
49	Schematic Illustration of Time-Dependent Signal Features . . . . .	87
50	Schematic of Voltage to Current Converter . . . . .	90

## 1. INTRODUCTION AND SUMMARY

### 1.1 Background

Turbine engine component life-management technology now being developed under a "retirement-for-cause" (RFC) approach requires a reliable method for detecting and characterizing defects. For the most part, the present high-resolution techniques for defect detection applicable to rotating components such as discs and spacers involve single-frequency eddy current examination. As evidenced by component performance, procedures based on these techniques have effectively screened out components having life-limiting defects. However, these simple defect detection approaches will not satisfy the more stringent needs of RFC programs. New methods that provide accurate sizing of defects must be developed.

PEC examination has been suggested as a possible approach to satisfy RFC program needs. PEC inspection consists of generating a pulse of current in an excitation coil, and then noting the characteristics of the signal in a receiver resulting from eddy currents excited in the examination material. This is in contrast to conventional eddy current examination, in which the excitation is a continuous wave of one or more discrete frequencies. Another difference is that with conventional eddy current examination, as generally practiced, the change in impedance of a single (excitation) coil is the measured parameter.

There are several possible advantages that a PEC system may have over a conventional eddy current system. First, pulsed operation is inherently a wideband signal excitation technique, and thus includes a wide range of frequencies without the need to explicitly generate each frequency. This fact is of interest because electromagnetic field penetration into a conducting material varies with frequency due to the well-known skin effect, and therefore more information may theoretically be obtained by using more frequencies. Second, there is time-domain information available in PEC testing; the pulse and each frequency band within it appear at specific instances in time after traveling through the examination material, because the propagation velocity of electromagnetic fields in conducting material is also a function of frequency. Third, pulsed operation coupled with a low duty factor (pulse repetition rate times pulse duration) for the transmitter probe allows the use of relatively high energy excitation pulses. For example, a typical duty factor of 0.1 percent achieved by using 1-microsecond long pulses at a repetition rate of 1000 pulses per second permits high energy excitation pulses of 500 volts maximum and 5 amperes maximum with an average power dissipation of less than 2.5 watts.

Although the technique of PEC examination has existed for some time, it has not found wide application, a fact that is particularly true for the low conductivity metals of interest in this project. Historically, only simple approaches have been used to extract information from PEC testing. One approach has been to simply measure the peak amplitude from a differential receiver coil (1); discontinuity in the material under test is indicated when the amplitude varies. Other approaches are based on the

observation that there exist certain points in the curve of output response to an induced pulse that do not change significantly when one variable, such as liftoff, is changed, but do change significantly in the presence of a defect. These points were explained by Waidelich in 1958 (2). Other suggested methods have involved sampling the received signal at several different points in time. The amplitudes thus obtained can then be parametrically combined in order to minimize the effect of variations of features not of interest and to maximize the signal due to features of interest (for example, references 3, 4, and 5). This approach is motivated by a desire to obtain available depth sensitivity similar to multifrequency eddy current testing, and takes advantage of the fact that the frequency spectrum varies as a function of time in the received pulse. These and similar approaches that involve sampling at one or several time or magnitude points apparently use only a small fraction of the inherently wideband signal information that is generated.

An additional motivation for new research into PEC testing is that, despite its general promise, PEC instrumentation has generally been developed for high conductivity and/or low magnetic permeability metals. In such material, relatively long risetime (several microsecond) pulses can be used because the propagation time of magnetic disturbance is relatively long; this is not the case for low conductivity nonmagnetic materials used in gas turbine engine disks. Thus, the electronics and probes for these materials must have a substantially greater bandwidth. Solid state power electronics has improved within the last ten years, enough so that precise control of pulses in this frequency range at reasonable cost is now feasible.

## 1.2 Objectives

The overall objective of this project was to develop and evaluate a PEC flaw detection capability that would be an improved means of evaluating surface and near-surface defects in low-conductivity materials used in gas turbine engine components. The specific objective was to optimize a bread-board pulsed eddy current system, including the probes, instrumentation, and signal analysis techniques. A specific goal was the reliable detection of 0.010-inch (0.25-mm) long by 0.005-inch (0.125-mm) wide by 0.005-inch (0.125-mm) deep surface-breaking flaws that are of interest for RPC purposes. An ultimate goal is the reliable detection and sizing of flaws of this size and larger, for both surface-breaking and subsurface flaws, and discrimination of such defects from various geometric configurations such as edges and corners.

The principal tasks of the SuRI approach to accomplish the program objectives were as follows:

### 1.1 Analytical Modeling and Probe Optimization

Develop a simplified model for predicting PEC response and apply to probe design optimization. Develop a more detailed analytical model extending classical solutions for coil excitation functions to the transient case, for use in identifying signal features associated with defect characteristics.

**Task II. Assembly of an Experimental Pulsed Eddy Current Breadboard System**

Fabricate reference defect specimens for system evaluation. Fabricate optimized probes, assemble a pulse generator, assemble a pulse receiver, and develop signal processing approaches. Conduct experiments to verify the analytical models. Verify the performance of the experimental breadboard system.

**Task III. Comparison of the Pulsed Breadboard System With the State-of-the-Art Continuous-Wave Eddy Current System**

Compare the results of the pulsed breadboard system with continuous-wave instruments. Provide recommendations for further exploratory development of the PEC approach.

**1.3 Summary of Results**

The breadboard PEC system successfully detected the target-size flaws. Initial results of the theory correctly predicted the field distribution from sample probes, in the absence of a flaw. Therefore, emphasis was placed on the possibility of using unique features of PEC to investigate flaw characterization. It was found that the simple theoretical models, obtained by integrating point flaw model fields over the depth of target-size defects, was not capable of quantitatively predicting the dependence of received pulse with flaw size. Investigations determined that the probable cause of the discrepancy is that the integrated point flaw model ignores the Kahn effect -- the tendency of eddy currents to be concentrated at the tip and to be depleted at the surface of a surface-breaking flaw. It was realized that this effect, if properly detected and used, could provide information about flaw depth, since the time that it would take the signal from the tip-concentrated eddy currents to appear at the surface would be characteristic of the depth of the source of concentration. This effect was modeled by the use of subsurface point flaws. Experiments confirmed the correlation with depth. In order to enhance this type of measurement, a new breadboard system was constructed. The new system included a unique pulser that allowed precise control of the excitation coil current. The pulse was arranged to minimize eddy current excitation during the detection period of the pulse cycle, in order to enhance the signal-to-noise ratio of the depth information. The existence of this flaw depth information in agreement with the crack tip model was confirmed.

**1.4 Report Summary**

In Section 2, the initial breadboard system is described and successful detection of target flaws is shown. Section 3 presents the model development, including the prediction of the field distribution from the transmitter probe and the use of signal characteristics to predict flaw depth. Comparison with experimental data is presented. It is shown that crack-tip eddy current concentration (Kahn effect) must be included in the model in order to predict flaw depth effects and to agree with experimental results. A pulse shape to enhance the depth information is presented.

Section 4 describes the breadboard system as modified to take maximum advantage of the flaw depth information. Experimental results show agreement with predictions in Section 3.

Section 5 presents tests on target flaws using conventional continuous-wave eddy current examination equipment. It is shown that its detection capability is comparable to that of the initial breadboard system, but its use in defect characterization is more uncertain.

Section 6 concludes the text with recommendations for further development of the pulsed eddy current method.

## 2. BREADBOARD SYSTEM DEVELOPMENT

### 2.1 System Description

Two different breadboard systems were developed during this project. The primary components of each system include a mechanical scanner, pulse generator, signal processor, display unit, and probes. The first system, described in this section, was designed to test basic concepts in probe design and flaw detection. Except for the probes, this system was constructed of commercially available elements. The schematic layout is shown in Figure 1. The Velonex pulse generator is capable of supplying variable amplitude pulses, with peak output up to 400 volts into a nominal 200 ohm load. The pulse width is variable from 0.1 to 300 microseconds.

Signal reception from the receiver coil is accomplished using a general purpose low-noise differential preamplifier, with a linear frequency response from DC to 50 MHz. In addition to amplification, the preamplifier may be used to provide a low-impedance (50 ohm) load to the receiver probe. This load may be thought of as providing impedance matching. In the time domain observations that have been made in this project, the load is important in reducing the circuit Q (quality factor) of the probe-receiver circuit to near unity so that its response to a rapid voltage change is well-damped.

A significant feature of the system for flaw detection is the boxcar averager with a sampling gate. By using a fixed-delay gate sample (a fixed time interval of signal duration at a fixed time relative to the pulsed trigger) and averaging the samples over many pulse repetitions, unwanted noise can be substantially reduced. The integrating function of the instrument accumulates DC output in direct proportion to the average of the signal within the gate interval. The output signal is thus reduced to a single value of amplitude at each spatial location. The gate placement can be dictated by the greatest change of amplitude on the waveform as the probe passes over the artificial flaws. The output is then sent to an X-Y recorder or to a single channel chart recorder for archiving and further analysis.

### 2.2 Flaw Specimens

Three flaw specimen reference standards were manufactured for this project. Detailed data sheets in Appendix E show the exact flaw layout with the specified and measured flaw sizes. Each standard consists of a block of Ti-6-4 that is 5 inches (12.7 cm) long by 2 inches (5.1 cm) wide and 0.25 inch (6.4 mm) thick. Each block contains a series of EDM notches. The notches are all 0.005-inch (0.13 mm) wide. They range in length from 0.050 inch (1.25 mm) to 0.010 inch (0.25 mm) and in depth from 0.050 inch (1.25 mm) to 0.003 inch (0.08 mm). The defects are arranged to allow six sets of continuous data:

- (1) Equal lengths, incremented depths.
- (2) Equal depths, incremented lengths.

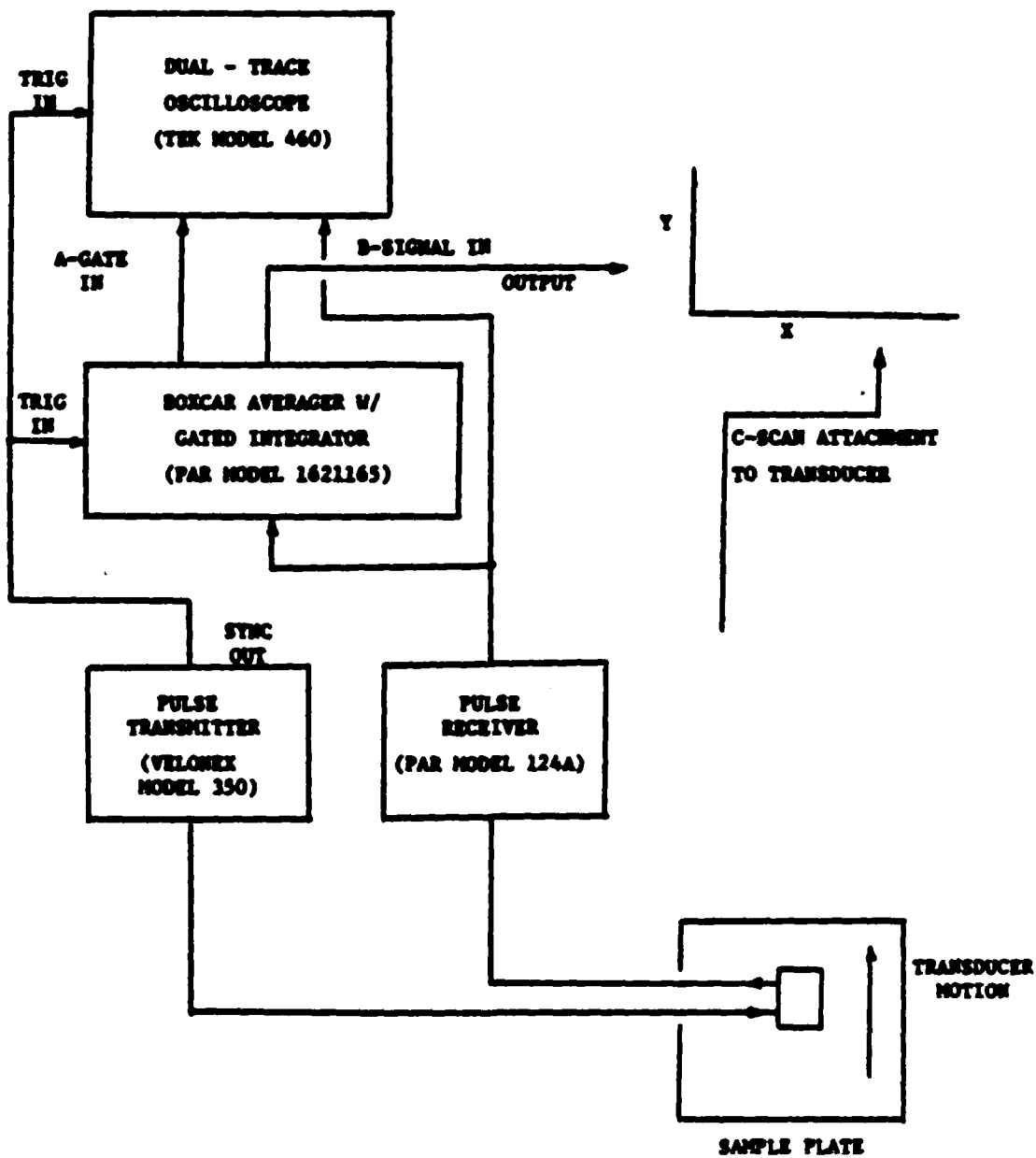


Figure 1. A Pulsed Eddy Current Test System. This breadboard system has been constructed using commercially available elements.

- (3) Different lengths and depths, with constant aspect ratio.
- (4) Parallel pairs of notches with various separation distances.
- (5) Notches parallel to the block edge at different distances from the edge.
- (6) Notches perpendicular to the block edge at different distances from the edge.

### 2.3 Flaw Detection Experiments

The probes for the flaw detection experiments consisted of a single transmitter and a pair of matched receiver coils. Both the transmitter and receiver coils were encased in separate copper tubing and placed coaxially next to each other. The transmitter and receiver coils were wound on separate ferrite cores and each encased in a 6 mm diameter copper tubing with a 0.9 mm wall thickness. The transmitting coil was wound using 50 turns of #32 gage magnet wire.

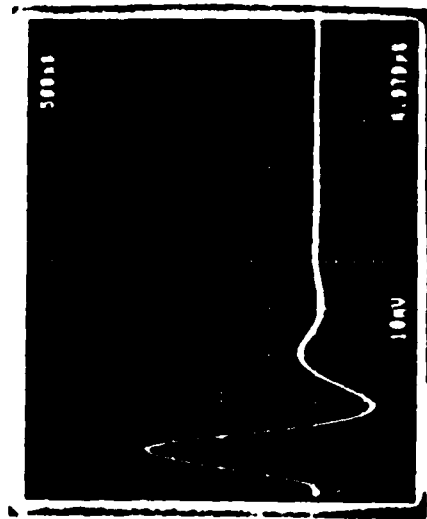
A bipolar pulse from the Velonex pulser was used to excite the transmitter. The risetime of the examination pulse was chosen by examining the frequency content of the excitation current. Figure 2 shows the effect of pulse shape and frequency content as the rise time of the current pulse changed from 100 nanoseconds to 20 nanoseconds. The excitation voltage of 500 volts was applied at a pulse rate of 300 cycles per second. The resultant pulse width ranged from 500 nanoseconds to 1 microsecond. A risetime of 150 nanoseconds was chosen in order to provide a flat, wide bandwidth signal. This pulse has a reasonably flat frequency response out to 1.2 MHz.

The receiver coils consisted of a pair of 150 turn, #40 coils wound on a single ferrite core to form a differential receiver probe. The receiver coils, as well as the transmitting coil, were encased in the 6 mm copper tubing.

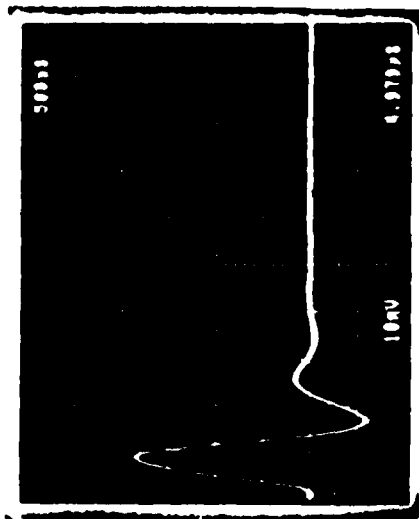
### 2.4 Evaluation Results

The probe described above was scanned across the surface of the manufactured flaw specimens. Figure 3 indicates test results obtained using a titanium 6-4 surface flaw specimen. The smallest flaw detectable is 250 microns long by 125 microns deep. In each case, the probe was oriented such that a line between the transmitter and receiver coils was parallel to the notch length.

Figure 4 indicates the edge resolution capability of the PEC probe, using data from the edge resolution standard. This standard has 1.25 mm long by 0.9 mm deep notches oriented perpendicular to the edge of the plate at various distances from the edge (as described in Appendix E). The closest distance at which a notch was detected was 1.25 mm from the edge of the plate.



250 n SEC



200 n SEC

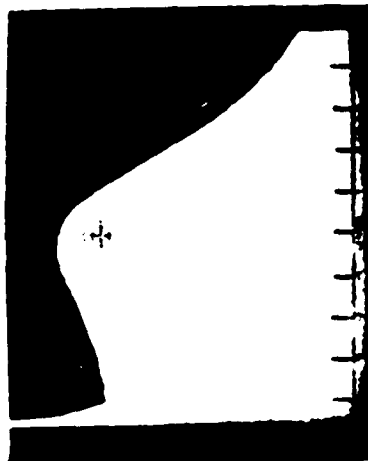
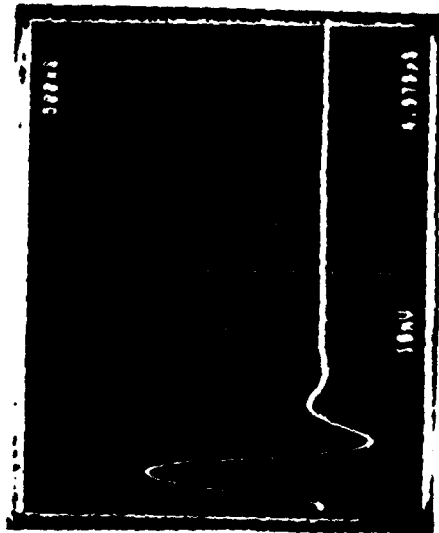
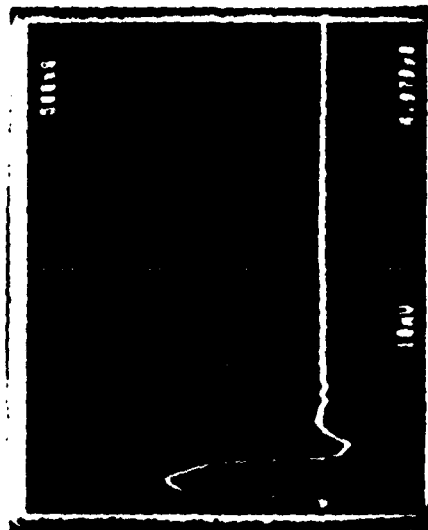


Figure 2. Transmitted Pulse Shape and Frequency Spectrum as a Function of Pulse Rise Time. A 6-mm diameter probe with a 0.9-mm wall was used. For low rise-time pulses, the probe shows a resonant peak.

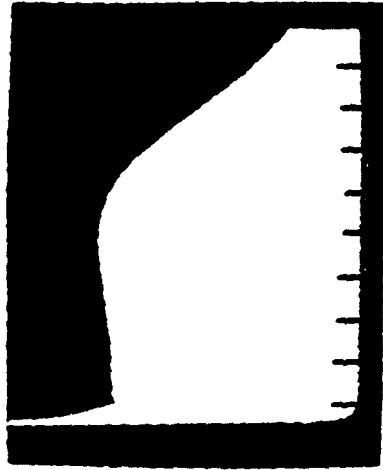


150 n SEC



100 n SEC

1 AMP 1 DIV



0.2 MHz 1 DIV

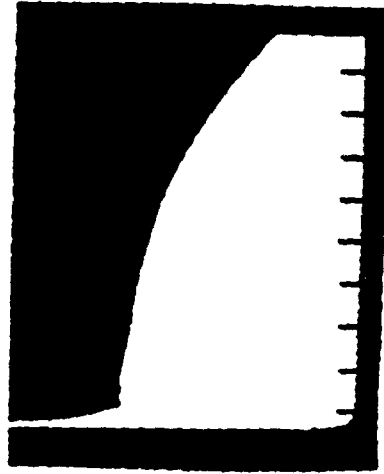


Figure 2 (Cont'd). Transmitted Pulse Shape and Frequency Spectrum as a Function of Pulse Rise Time. A 6-mm diameter probe with a 0.9-mm wall was used. For low rise-time pulses, the probe shows a resonant peak.

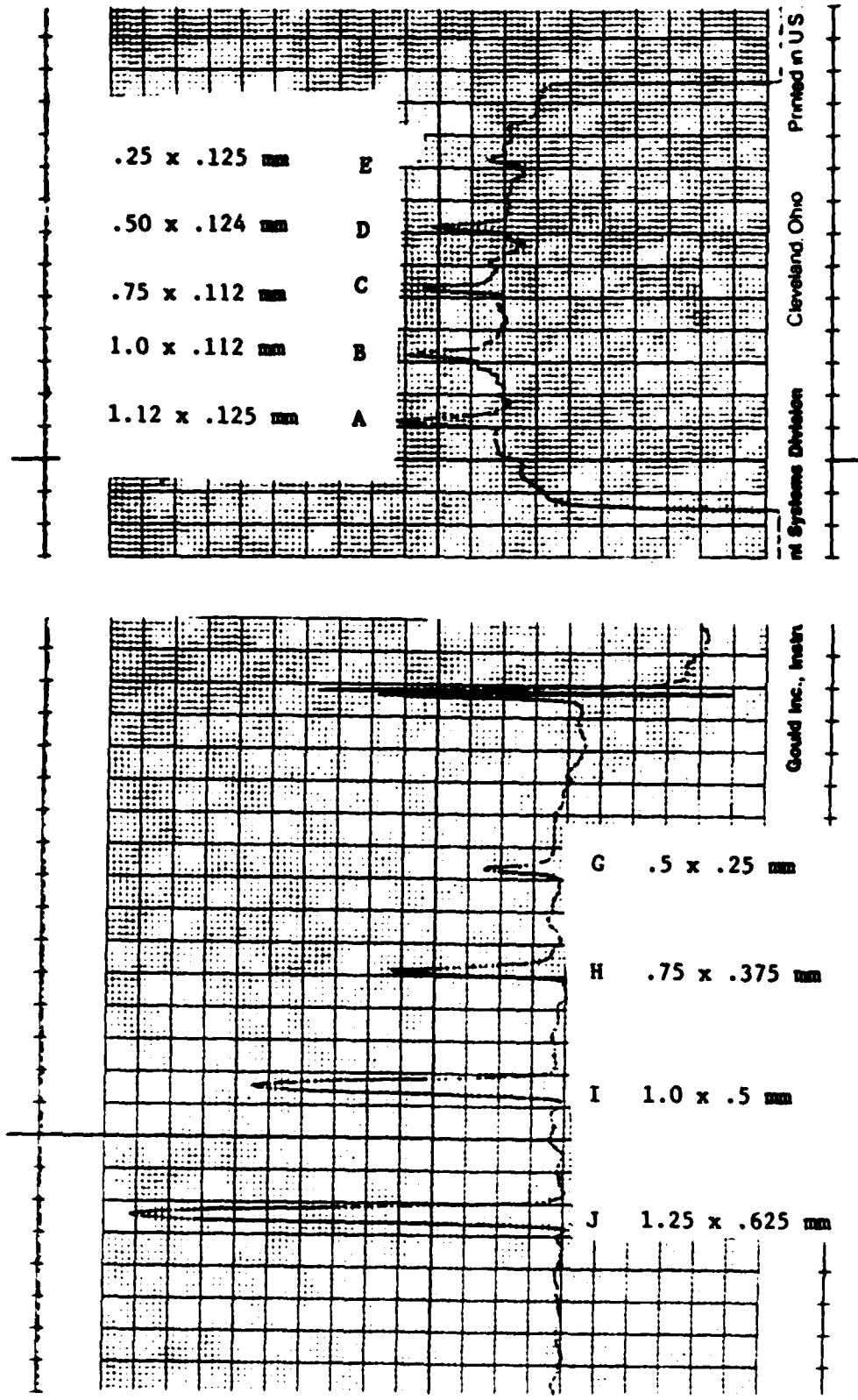


Figure 3. Detector Scans from Ti 6-4 Block with EDM Notches. The smallest flaw detected was .25 mm long by .125 mm deep. All notches are .125 mm wide.

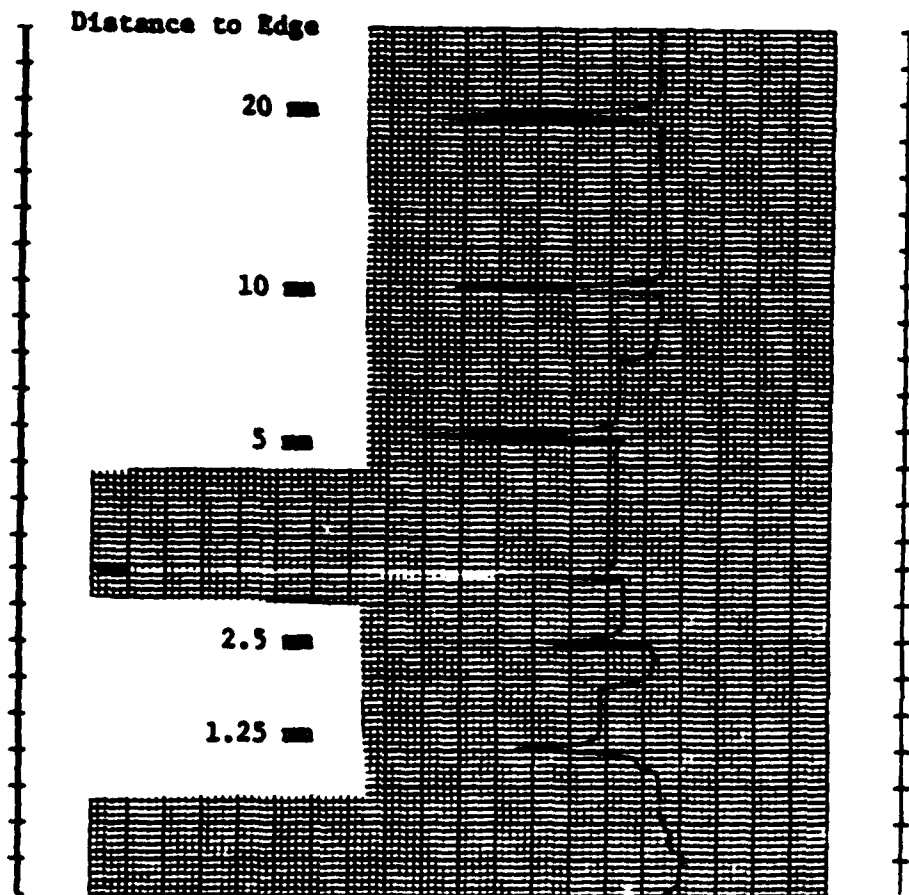


Figure 4. Edge Resolution Scans from a Ti 6-4 Block with EDM Notches. Notches are 1250  $\mu\text{m}$  long and 250  $\mu\text{m}$  deep. These data are taken using the same probe used in Figure 3. All notches are detected.

Figure 5 indicates the results of the spatial resolution test obtained with the same PEC probe. The specimen scanned contains sets of EDM notches, 1.25 mm long by 0.9 mm deep by 0.125 mm wide, arranged parallel to each other at various spacings, as indicated in the figure. As can be seen, it is not possible to separate two flaws that are closer than 2.5 mm with this probe. Probes with smaller diameters, however, can separate flaws spaced as close as 1.25 mm. These are described in the next section.

## 2.5 Additional Probe Development

Early probes were designed with simple geometries to match the modeling capability described in the following section. These probes demonstrated that the basic flaw detection goals of the program could be met. However, the spatial resolution capability of these probes was only marginal. Therefore, additional probe development was concerned with improving this capability. The basic approach was to minimize the electromagnetic footprint of the transmitting coil on the inspection surface. This may be accomplished by making the probe smaller, of course, and by using a probe design with better focusing capability. Both of these approaches, especially the former, tend to reduce the magnetic field amplitude in the desired inspection area.

One way to provide a smaller footprint without sacrificing size is to improve shielding. Figure 6 shows the effect of different shielding material and lack of shielding. The probe consists of 50 turns of #36 gage wire wound around the ferrite core. The apparent inductance as a function of frequency is shown for the coil unshielded, and shielded with copper, aluminum, steel, and ferrite. The inductance produced is directly proportional to the amount of energy created in the magnetic field generated by the probe. Since the magnetic energy density is proportional to the square of the magnetic field intensity, a reduction in magnetic field volume and proportional increase in flux density causes an increase in total energy and therefore inductance. A decrease in inductance may be caused by an increased magnetic volume, but also by a reduction of intensity due to increased generation of eddy currents in the probe. Copper, steel, and aluminum provide shielding by generating eddy currents that cancel the primary field. Since ferrite is a poor conductor, it does not generate an opposing magnetic field; rather it provides a low reluctance path for the magnetic field lines exterior to the probe core between the top of the core and the inspection material. The figure shows that at the relatively high testing frequencies of interest in this project, eddy current losses in copper, aluminum, and steel cause a substantial loss in magnetic field energy, even though the magnetic volume must be severely reduced. These losses increase as the frequency increases. On the other hand, the ferrite shielding increases the inductance by a factor of approximately 1.8 over the entire frequency range of interest. It is concluded that ferrite shielding is quite useful in concentrating the magnetic field energy, and that highly conducting material, while of use for low frequency eddy current testing is not as desirable at the higher frequencies appropriate to examination of poorly conducting alloys.

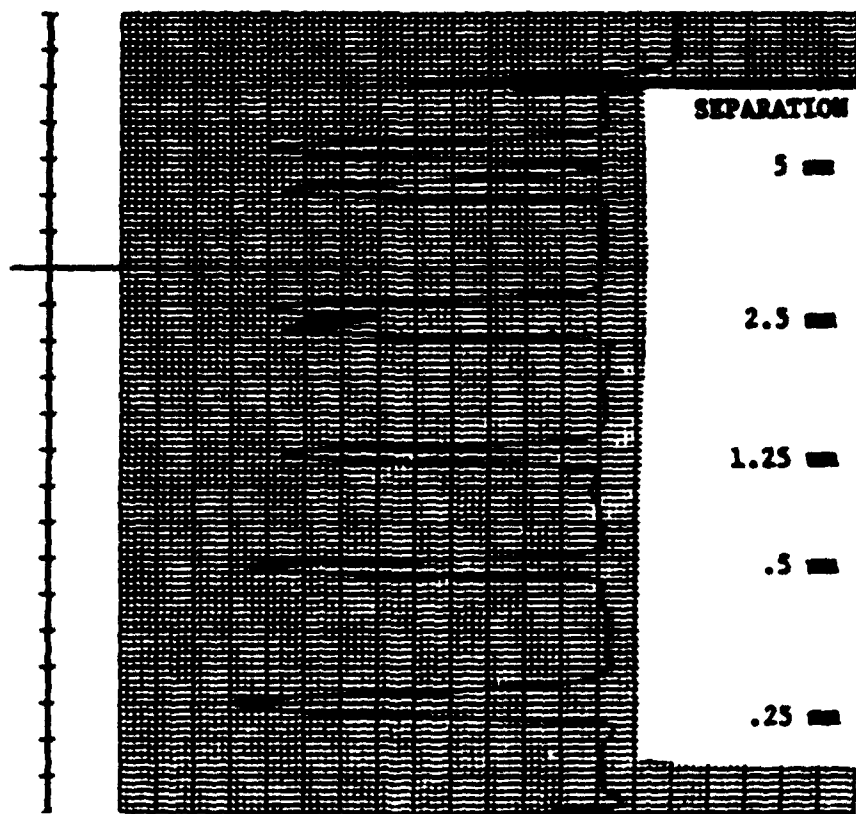


Figure 5. Spatial Resolution Scans from Ti 6-4 Block with 1.25 x .9 mm EDM Notches. Notches spaced closer than 2.5 mm can not be distinguished.

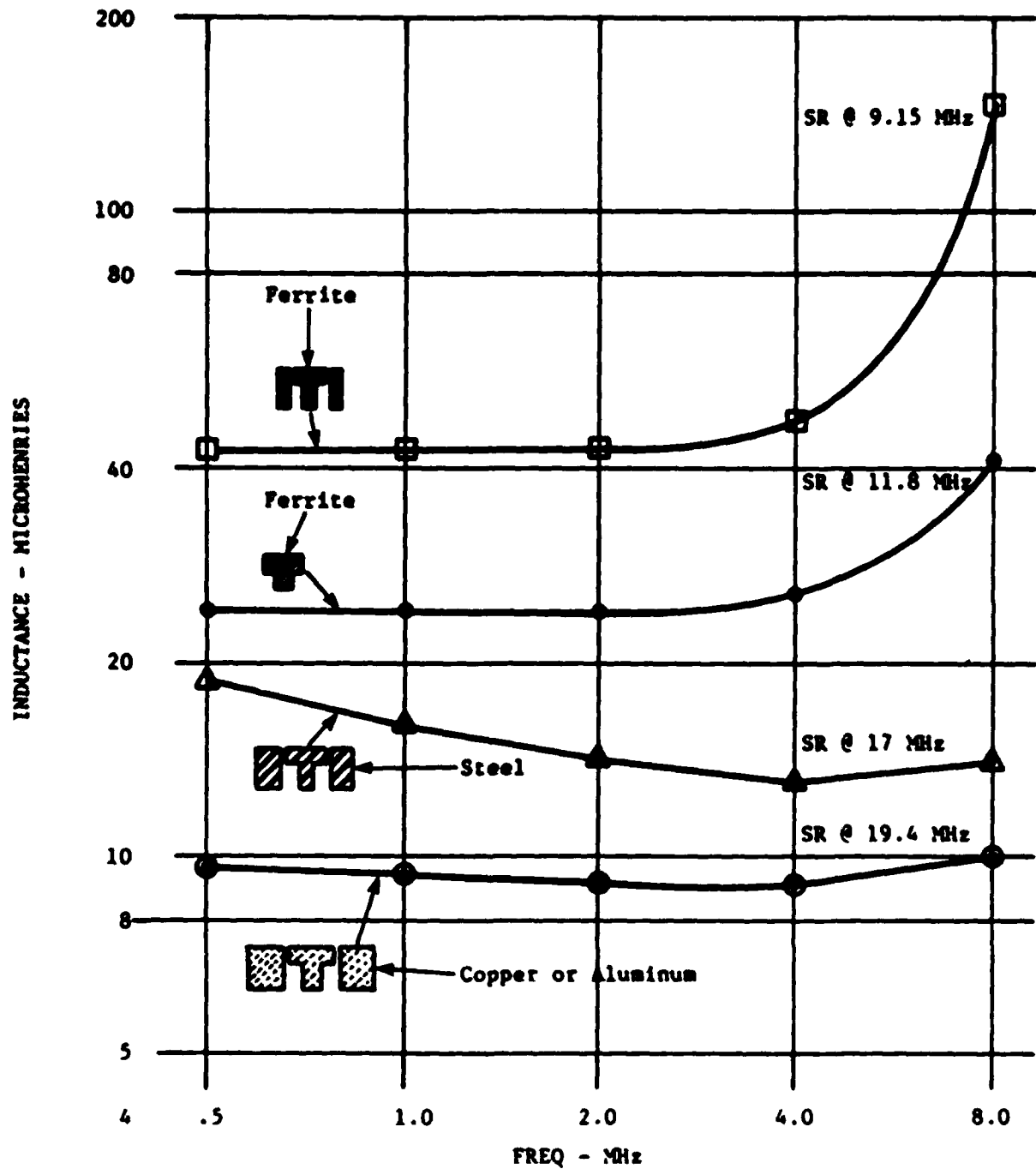


Figure 6. Change in Inductance of a Ferrite Core Coil with Different Shielding Material. Only ferrite shielding increases the magnetic field energy, indicating a strong concentrating effect without decreasing the field intensity.

In order to obtain quantitative measurements of the focusing ability of copper versus ferrite shielding, measurements were taken of the normal magnetic field produced after passage through two different thicknesses of titanium for two probes with the same size ferrite core. The amplitude of the normal component of the field was measured by a small (1 mm diameter) sensing coil, as a function of distance along one axis at the surface opposite the transmitter, for thickness of 1.3 and 3.2 mm. Results for the footprint size, as indicated by the distance over which the amplitude is at least half the maximum amplitude, are shown in Table 1. It is seen that the ferrite shielding, in addition to providing greater field strength, has a footprint approximately the same as the copper-shielded probe at the small thickness, but which increases only 29 percent compared to 47 percent through the entire thickness of titanium, so that the final footprint is 20 percent less than that of a similarly sized copper-shielded probe.

Table 1

FULL WIDTH OF HALF MAXIMUM NORMAL FIELD IN THROUGH TRANSMISSION

<u>Ti Thickness</u>	<u>Copper-Shielded Probe</u>	<u>Ferrite-Shielded Probe</u>
0.050" (1.27 mm)	3.0 mm	2.8 mm
0.125" (3.18 mm)	4.4 mm	3.6 mm

Two additional improvements have been made to the ferrite shielded probe. It has been found that a layer of copper shielding placed outside of the ferrite can be used to remove stray fields remaining, and thus reduce coupling to the receiver probe. For a sufficiently thick ferrite shield, this additional layer has negligible effect on the probe impedance, but it does reduce the coupling to an unshielded receiver probe. The amount of reduction depends on receiver placement.

A second improvement is the placement of a copper disk around the ferrite core between the core and the shielding at the examination surface side (Figure 7 shows the completed probe design). This disk is used to increase the magnetic reluctance of the air path between the shielding and the core, in order to minimize the number of leakage field lines that pass from the core to the shield, tangential to the inspection surface, without penetrating the surface. In order to prevent eddy currents in the copper disk from also opposing the normally oriented magnetic field, a vertical slit is cut through the entire height of the disk at one circumferential location.

A possible problem with the use of the split ring conducting disk is that a small gap may have a large enough capacitance to allow significant eddy current density to develop in opposition to the primary field. This

problem is greater at higher frequencies, since the capacitive reactance is inversely proportional to frequency. However, measurements taken with this probe design show an increase in the normal component of the magnetic field of 10 percent through a 3.2-mm thick titanium plate, compared to a similar probe without the copper disk.

Another type of transmitting coil that was evaluated used a toroidal gap core. The transmitter geometry is illustrated in Figure 8. The toroidal cores had 0.375-inch outside diameter, 0.187-inch inside diameter, and were 0.125-inch thick. Gap distances ranged from 0.050 to 0.100 inch. Figure 9 shows the normal component of magnetic field for a coaxial probe encased in 6-mm diameter copper tubing, and the same component across the air gap of a toroidal gap core. It was concluded that the shielded coaxial probe offers better focusing than the toroidal gap coil, although with copper shielding, the field intensity of the coaxial probe is approximately one-half that of the toroidal gap coil. With the use of ferrite shielding, this disadvantage is ameliorated. Therefore, it was decided not to pursue this design.

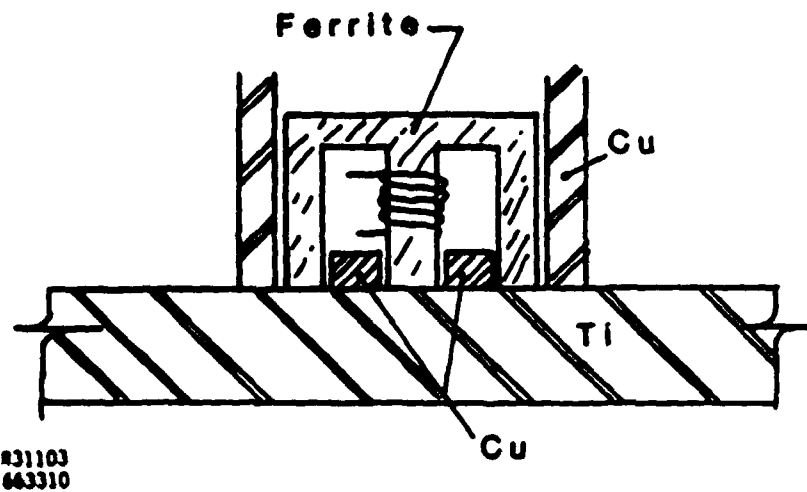


Figure 7. Improved Ferrite-Wound, Not-to-Scale, Ferrite- and Copper-Shielded Probe with Cylindrical Symmetry.

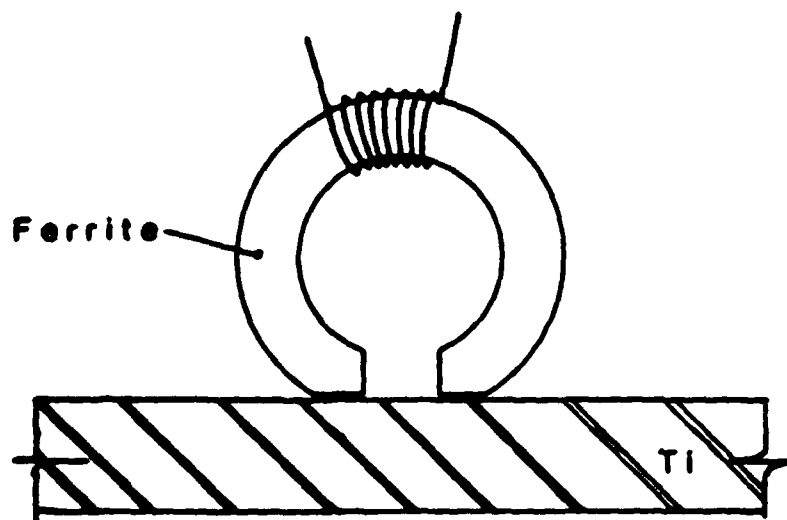


Figure 8. Toroidal-Wound Probe. This probe showed less focusing than cylindrical probes.

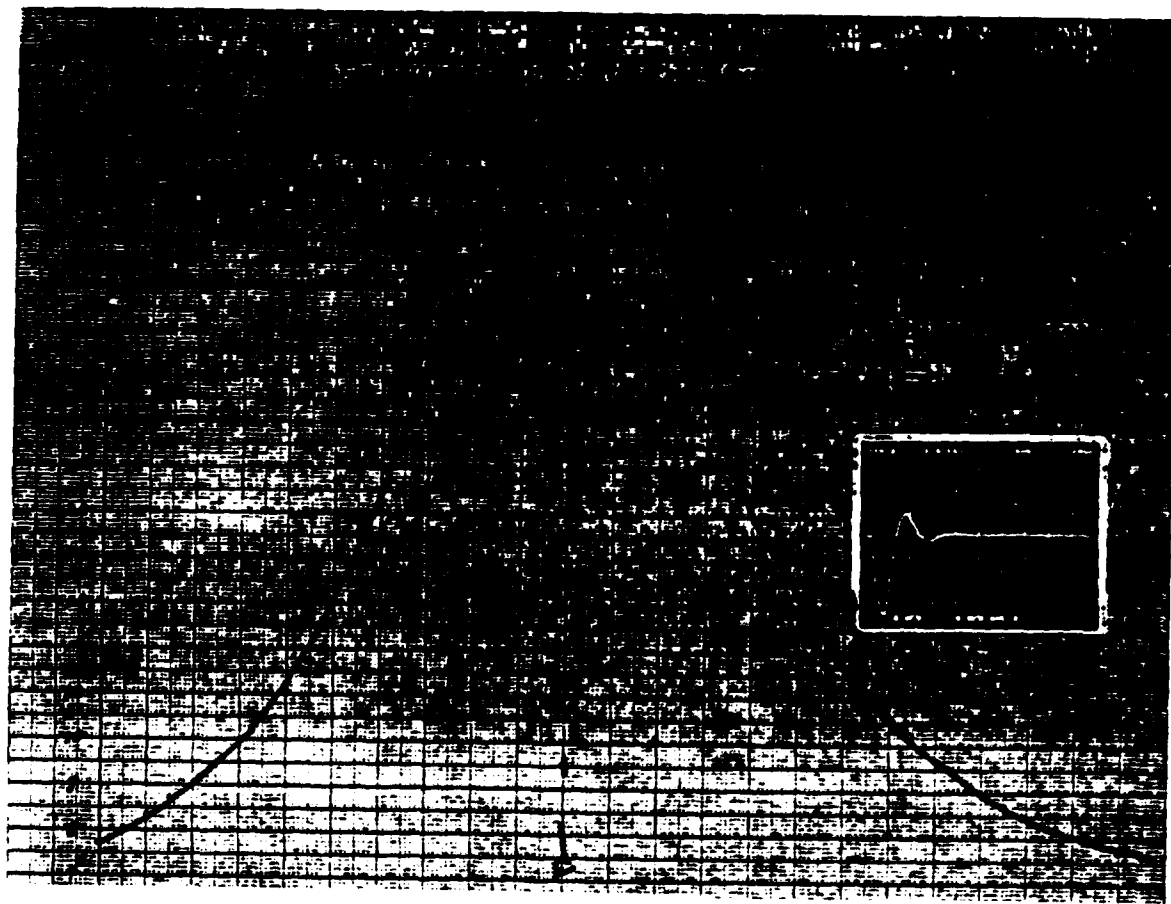
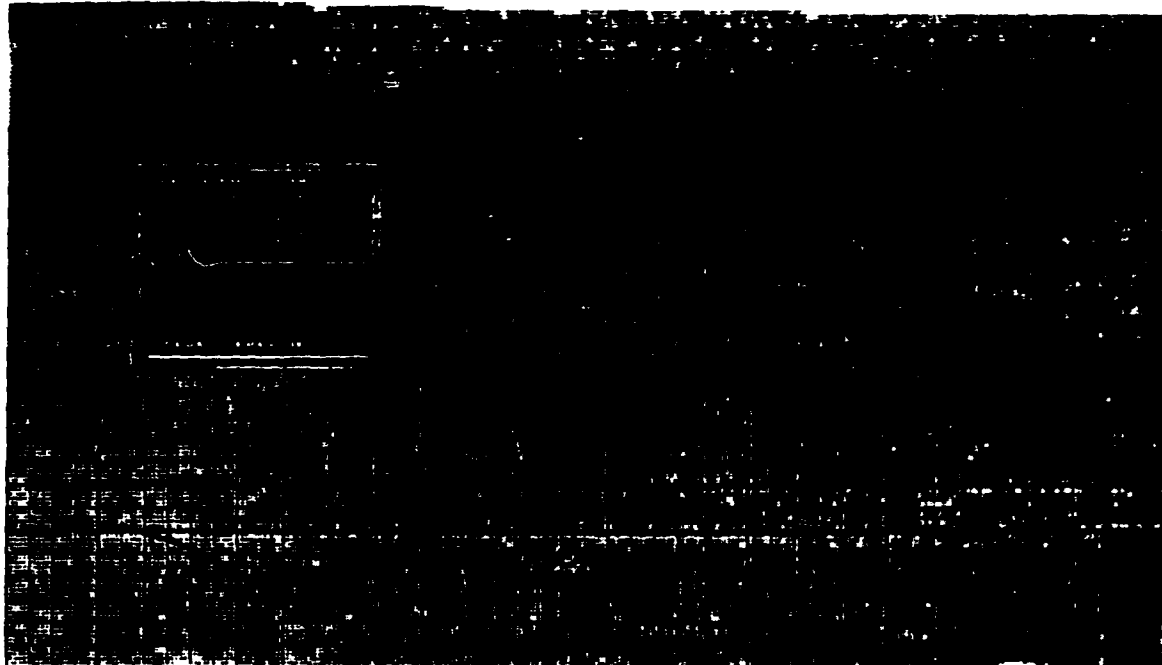


Figure 9. Comparison of Normal Component of Magnetic Field in Air. The top field profile is obtained from a shielded coaxial probe, while the bottom is from a toroidal gap coil. As shown by the insets, similar current pulses were used for both coils. The shielded coaxial probe exhibits less spatial broadening.

### 3. MODEL DEVELOPMENT AND EXPERIMENTAL VERIFICATION

#### 3.1 Introduction

The development of a mathematical model of a pulsed eddy current system was approached in two steps. First, the simplified model illustrated in Figure 10 was developed to explore the effects of probe geometry on the fields produced in the absence of a conducting test piece. The second step included a generalization of the simple model to include:

- (1) A finite coil winding thickness,
- (2) The approximate effect of a ferrite coil,
- (3) A separate, differential receiver coil,
- (4) The change in receiver response caused by the presence of an unflawed specimen, and
- (5) Additional changes caused by the presence of a point flaw.

Parameters included in the detailed model are those shown in Figure 11. A more complete description of both models, along with the results of some exploratory calculations, is given in Appendix A. An alternate model, which required too much computer time for pulsed eddy current analyses but which may be useful for other purposes, is described in Appendix B.

#### 3.2 Effects of Probe Geometry

As a test of the model of the transmitter coil and shield, calculations of the magnetic field in air were performed and compared with experimental data obtained by scanning a small Hall-effect sensor radially across the coil. The result, which is shown in Figure 12, verifies the validity of prediction of fields produced by a shielded excitation coil.

The detailed model was then applied to parametric studies of the effects of probe geometry on the eddy current distribution in a conducting material and on probe response to a hypothetical point flaw. The results of these calculations, which are summarized in Appendix C, show that the effects of probe geometry are similar to those observed with continuous wave eddy current systems. Thus, for example, the calculations show that the eddy current distribution is spatially broadened and increases in intensity as the transmitter coil diameter is increased. Small changes in the coil-to-shield distance produce minor variations in the distribution, though removal of the shield leads to a more diffuse pattern of current flow in the material. Use of a differential sensor leads to improved flaw resolution, as expected, with the maximum signal strength occurring when the flaw is directly below the transmitter coil winding. In summary, then, the model reveals that the influence of probe geometry on pulsed eddy current flaw response is essentially the same as in the continuous

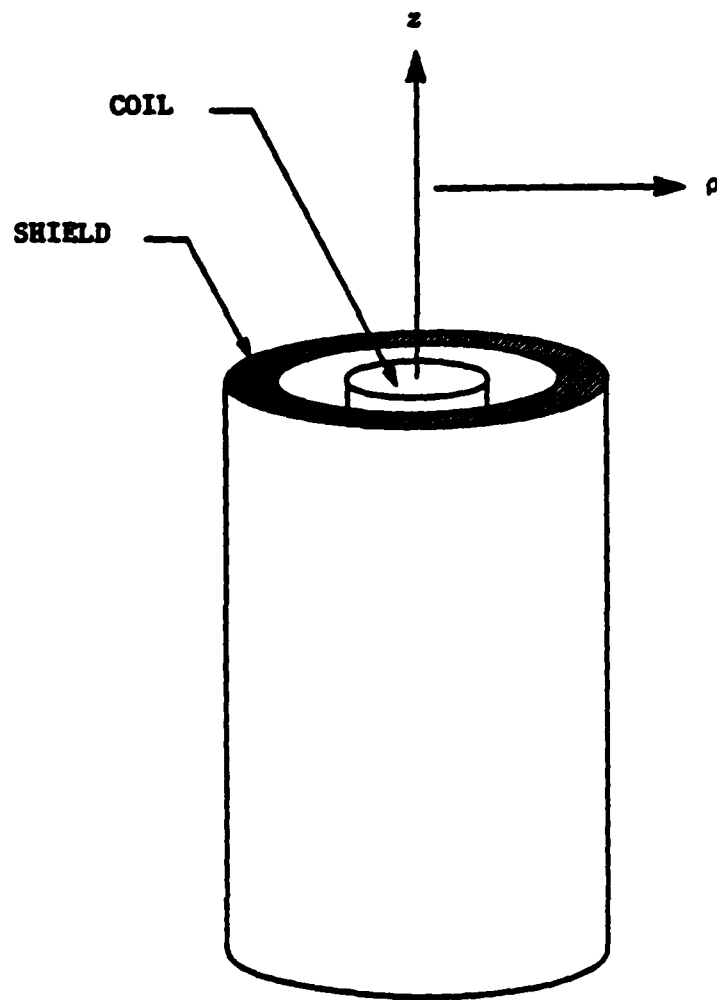


Figure 10. Simplified Model of Pulsed Eddy Current Probe. This model was used to evaluate the field in front of and alongside the probe. The finite current coil is modeled as a current sheet of infinitesimal thickness.



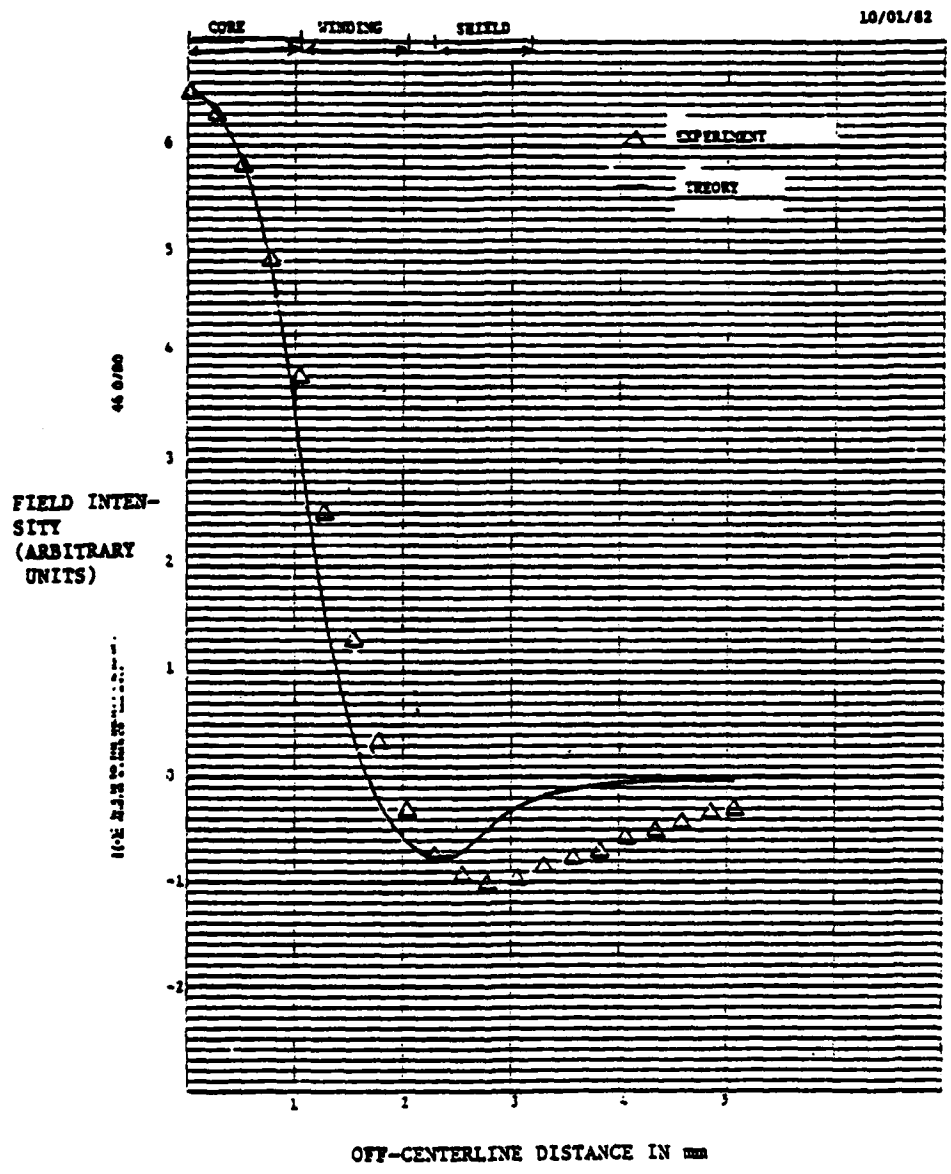


Figure 12. Comparison of Calculated and Measured Fields From a Pulsed Eddy Current Coil in Air

wave case. It follows that, as far as the geometrical aspects of probe design are concerned, experience with continuous wave probes is directly applicable to the design of pulsed eddy current probes.

The distinguishing feature of pulsed eddy current flaw response is, of course, the time dependence of the signal which, hopefully, contains information pertaining to flaw geometry. Thus, while calculations of the influence of probe geometry were needed to determine possible deviations from the continuous wave case, the principal reason for undertaking pulsed eddy current model development was to explore features in time-dependent flaw signals and their relationship to flaw geometry.

### 3.3 Effects of Flaw Geometry

The results of some early calculations of flaw signals are shown in Figures 13 and 14. Figure 13 shows calculated signals from point flaws at various depths below the surface plotted as a function of time (in  $\mu\text{sec}$ ) and normalized to unity at peak value. The important point illustrated here is that flaw signal peak arrival times increase with flaw depth and therefore provide a measure of depth. However, for point flaw depths corresponding to crack tip depths of interest, peak arrival times are of the order of tens of nanoseconds. Thus, if depth information is to be obtained from peak arrival time measurements, input pulse widths or pulse decay times must be extremely short, probably of the order of a few nanoseconds.

Another characteristic of point flaw signals is illustrated in Figure 14. This is a plot of flaw signal peak amplitude as a function of flaw depth for three different pulse widths. The main point to note here is that predicted signal amplitudes decrease by about a factor of 100 in the first 0.1 mm of depth below the surface. Thus, based on these two sets of point flaw calculations, one might expect that signals of interest are very weak compared to signals from near-surface reflections and that the arrival times of interest are of the order of tens of nanoseconds.

However, experimental results for surface-breaking slots of various depths, which will be presented in the next section, show a very definite depth dependence even though the input current waveform was much broader than that used in the calculation shown in Figure 13. This observation, which seemed to be in conflict with model calculations, called for more detailed comparisons between theory and experiment and led, eventually, to a reexamination of one of the basic assumptions inherent in the model.

### 3.4 Comparison With Experiment-Zero Crossing

A series of experiments was carried out in order to compare measured flaw response with theoretical predictions. The parameter measured was zero-crossing time, that is, the time relative to an arbitrary beginning of pulse time that the received signal first crosses below zero amplitude. This measurement was chosen for two reasons. First, it provides an indication of the peak signal arrival time, but is more precisely measured than the peak time itself because the slope of the signal is in general greater at the zero-crossing point. Second, previous theoretical and experimental

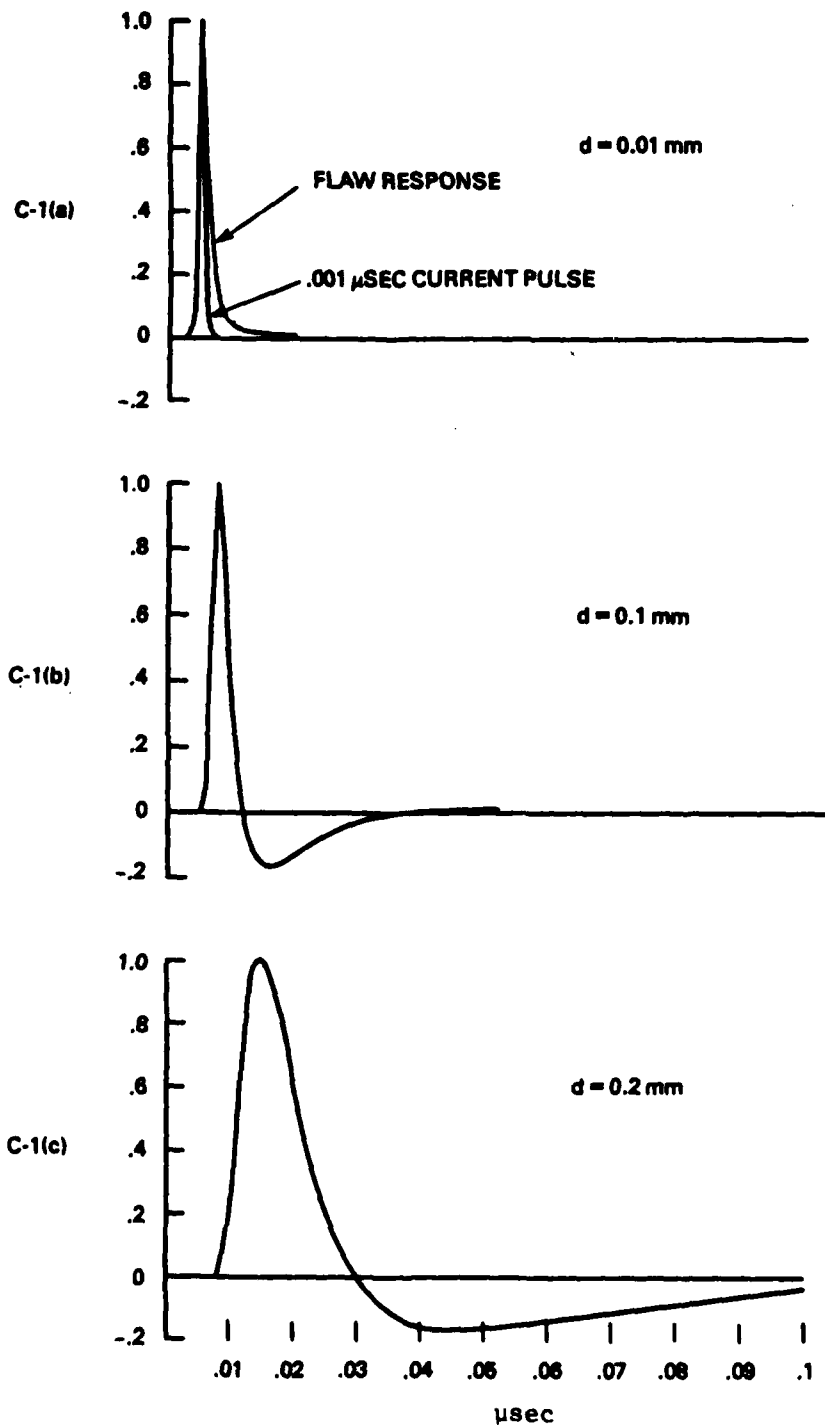


Figure 13. Calculated Signals from Point Flaws at Various Depths Below the Surface, for a 1 nsec Gaussian Pulse. For corresponding crack tip depths of interest, peak signal arrival time is of the order of 10 nsec.

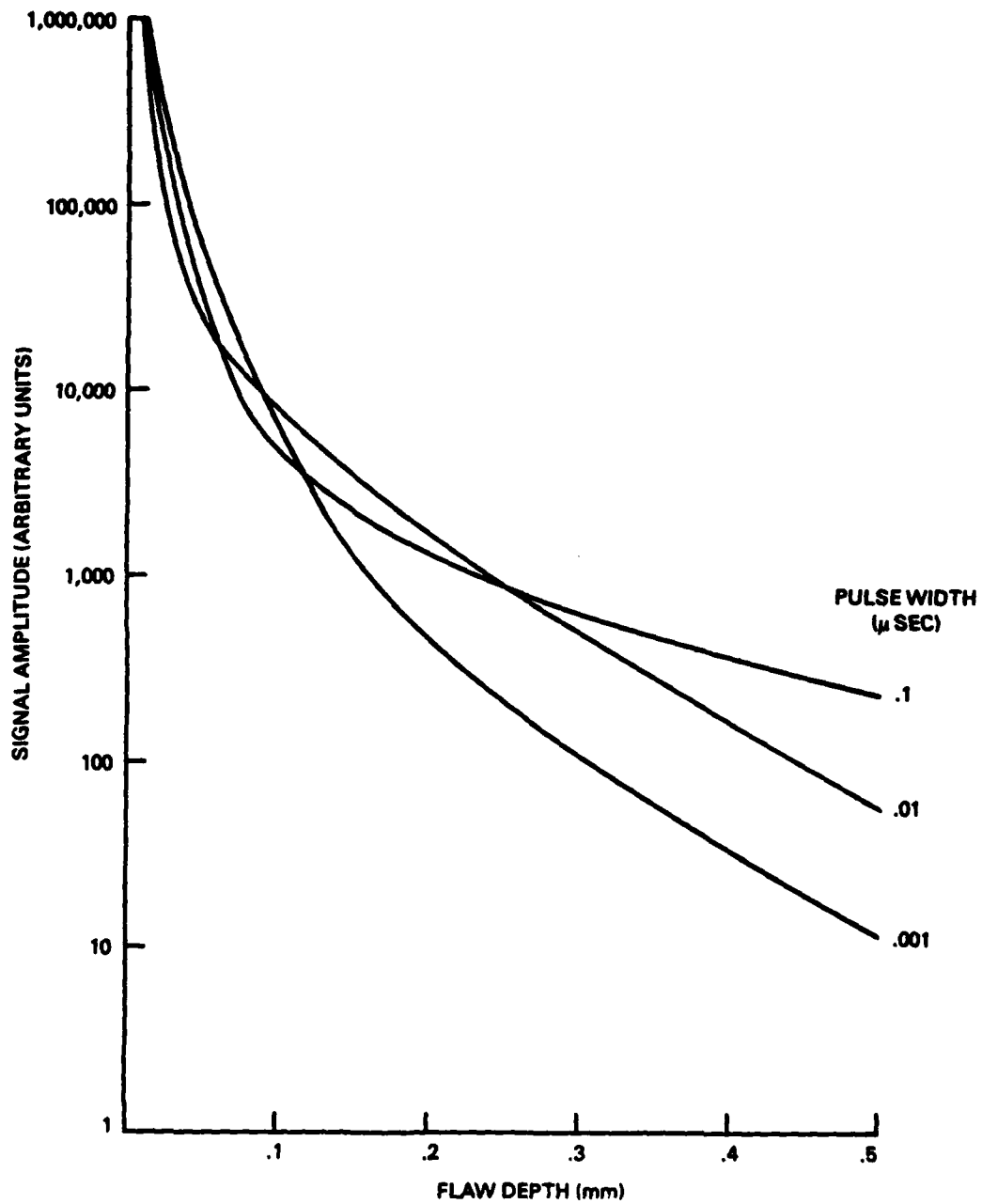


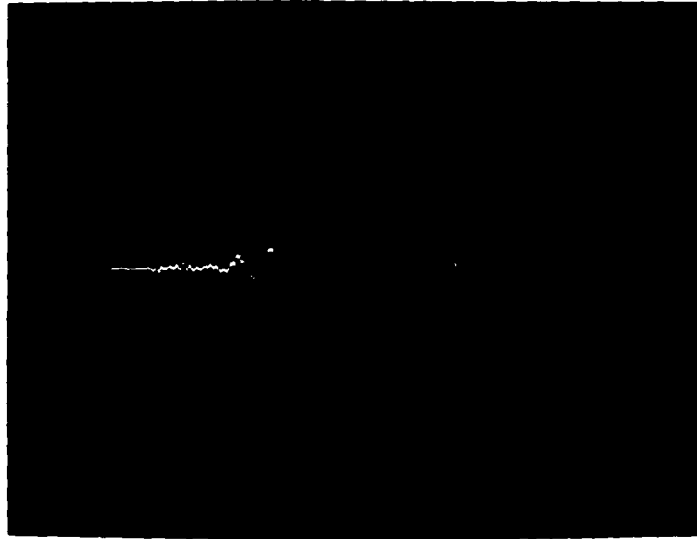
Figure 14. Point Flaw Signal Peak Amplitude as a Function of Flaw Depth, for Different Pulse Widths. Predicted signal amplitude decreases by a factor of approximately 100 in the first .1 mm of depth, indicating very weak signals compared to near-surface reflections for this model.

results have shown that there is in general an amplitude, the time of which is sensitive to the presence of flaws but not to variation in lift-off (2). This second factor can be predicted by assuming that lift-off variation is equivalent to a change in receiver probe resistance and inductance. The simple theory does not guarantee that the amplitude predicted will actually be in the range of amplitude available. However, it was experimentally confirmed that this point exists for the probes in the PEC breadboard system on a titanium sample, as shown in Figure 15. It is observed from this figure that this amplitude crossing point is close to the zero-crossing point. With this justification, a series of experiments measuring zero-crossing time was carried out. A copper-shielded transmitter probe, with differential, shielded receiver coils was used. The results will be presented after a discussion of the theoretical calculations.

In Figure 15(a), the receiver probe signal over Ti-6-4 sample with no flaw, for three different values of lift-off, is shown. Note that at 0.5 amplitude (vertical) divisions, the crossing time is approximately independent of lift-off. In Figure 15(b), the receiver signal over a 1.8 mm deep flaw is shown, again for three different values of lift-off. The lift-off-insensitive crossing point exists and is at the same near-zero amplitude but occurs 160 nanoseconds earlier.

To make direct comparisons between theory and the zero-crossing data described above, it was necessary to modify the analytical model to account for the geometry of the flaws used in the experiment. In making this modification, it was necessary to introduce additional approximations because the basic theory makes use of the assumption that the electric field inside a flaw is proportional to the unperturbed field at the center of the flaw. This can be rigorously justified only in the case of small subsurface flaws such that the unperturbed field does not vary significantly over the surface of the flaw. However, for an extended flaw in a nonuniform field, one might expect the interior field to vary from point to point in a way that is approximately proportional to the spatial variation of the unperturbed field. Thus, as a first approximation to a theory for an extended flaw, the point flaw solution can be simply integrated over the volume of the flaw. The resulting flaw response function that depends on flaw dimensions is multiplied by a scattering factor  $\alpha$ , which is a scalar approximation to the matrix  $\alpha$  defined in Appendix A. Because there is no theory that allows one to calculate the value of  $\alpha$  for a rectangular slot, it was treated as an adjustable parameter in making comparisons with the experiment.

However, in experimental data, the flaw response function alone is not observed, but rather the sum of the signal with no flaw and the change caused by a flaw are observed. Thus, to compare with the experiment, one must add a no-flaw component to the calculated signal. Because the no-flaw signal is lift-off dependent, this amounts to incorporating lift-off dependence as part of the model.



(a)



(b)

Figure 15. Confirmation of the Existence of a Liftoff-Insensitive Amplitude Crossing Point. At top is the no-flaw signal for 3 different values of liftoff. At the bottom is the flaw signal for 3 different values of liftoff, with the crossing point occurring .8 units earlier.

A mathematical model of the response of a pulsed eddy current probe to liftoff variation was therefore developed. The theory is based on a time-dependent generalization of Auld's reciprocity theorem (6); the calculation proceeds in much the same way as in the continuous wave eddy current case. The principal result is the following expression for the change in the impulse response function as the probe is moved from an infinite liftoff distance to liftoff distance  $l$ .

$$\delta\Gamma_l = \text{constant} \cdot \frac{R_1 R_2}{\tau^{3/2}} \int_0^{\infty} e^{-k^2 \tau - 2kl} J_0(kd) J_1(kR_1) \left[ \frac{J_1(kR_2)}{R_2} - kJ_0(kR_2) \right] k dk$$

where  $R_1$  and  $R_2$  are the radii of excitation and differential receiver coils, respectively;  $J_0$  and  $J_1$  are Bessel functions of the first kind of order 0 and 1, respectively; and  $\tau$ , the scaled time, is given by

$$\tau = \frac{t}{\mu\sigma}$$

The response of a pulsed eddy current probe is the convolution of the excitation pulse with an impulse response function which is the sum of  $\Gamma_0$ , the response in air in the absence of a specimen,  $\delta\Gamma_l$ , the change caused by an unflawed specimen at liftoff  $l$ , and  $\delta\Gamma_f$ , the change caused by a flaw. As was noted earlier, the magnitude of  $\delta\Gamma_f$  relative to the other components of the impulse response function is unknown because the calculation of  $\delta\Gamma_f$  is based on a small flaw theory and contains an adjustable parameter to approximately account for finite flaw dimensions. Therefore, the change in response caused by the specimen and flaw can be described by

$$\delta\Gamma = \delta\Gamma_l + \alpha\delta\Gamma_f$$

where  $\alpha$  is an adjustable multiplier.

In the initial set of liftoff-dependent calculations, an exponentially damped sine wave was used as the excitation current, and  $\alpha$  was varied in an attempt to obtain qualitative agreement with experimental data. Typical results are shown in Figures 16 through 17. The dotted curves, which are the same in both figures, are predictions of probe response in the absence of flaws. The dashed curves are flaw-induced changes, and the solid curves are the sums of the dotted and dashed curves. The parameter  $DT$  is one-half the period of the excitation pulse

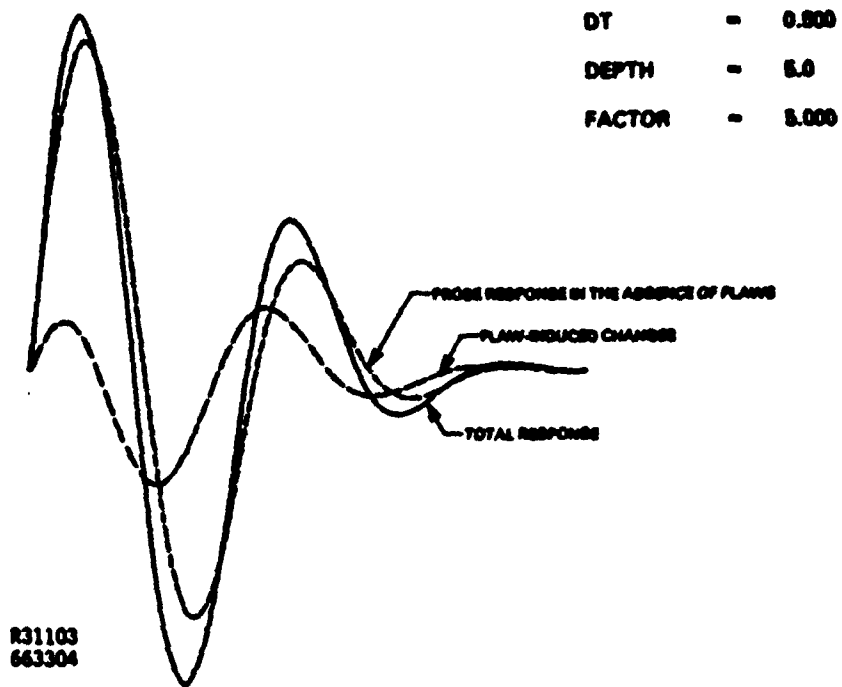


Figure 16. Calculated Response Function for a .25 x .15-mm (10 x 5-mil) Slot.

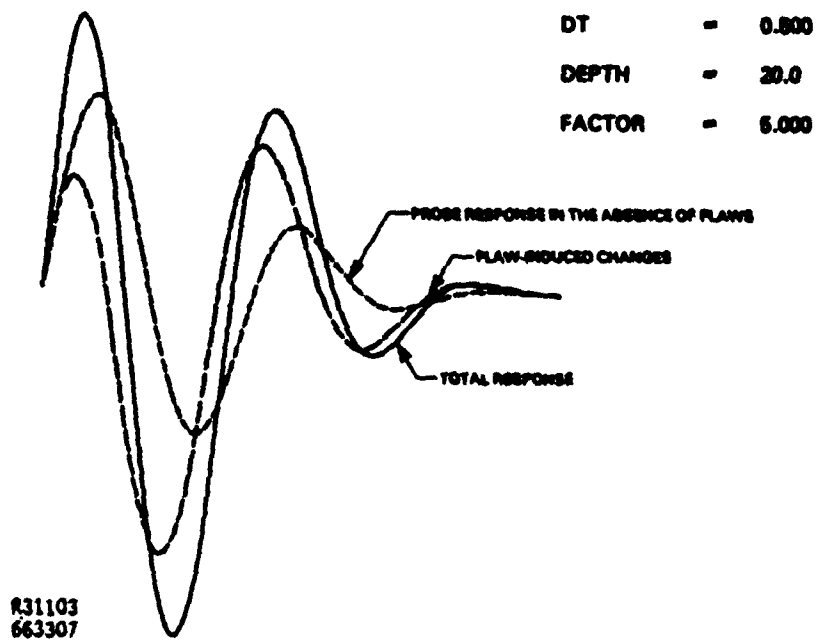


Figure 17. Calculated Response Function for a 1.0 x .50-mm (40 x 20-mil) Slot.

in microseconds, DEPTH is the depth in mils of a rectangular surface slot with length = 2 x DEPTH, and FACTOR is a number proportional to the adjustable parameter  $\alpha$ .

The effect such calculations were designed to explain is the experimentally observed shift in the first zero crossing as a function of flaw size. From the figures, it can be seen that the theory attributes this shift to an increase in the magnitude of the flaw signal relative to the no-flaw signal as flaw size increases. Thus, for example, in Figure 16, the flaw signal (dashed curve) is small compared to the no-flaw signal (dotted curve); and the zero-crossing shift, the difference between the dotted and solid curves, is small. In Figure 17, on the other hand, the flaw signal is much larger compared to the no-flaw signal; and the zero-crossing shift is correspondingly greater. Significantly, these data indicate that the zero crossing is almost entirely determined by the relative magnitudes of the flaw and no-flaw signals; there is no significant change in the shape of the flaw signal as flaw size increases.

Calculated zero-crossing data are plotted in Figure 18 along with experimental data. The calculated times are shifted approximately 0.3  $\mu$ sec to agree with the measured zero-crossing time, about 1.3  $\mu$ sec, with no flaw present. As can be seen from this figure, both theory and experiment show an increase in zero crossing time with decreasing flaw depth, though the functional forms of predicted and measured relationships differ significantly.

To determine if this difference is caused by a poor choice of the adjustable parameter  $\alpha$  that fixes the flaw response amplitude, we allowed  $\alpha$  to vary from about one-half the value used here to a maximum of four times this value. In all cases, the predicted curve was concave upward, as in Figure 18, in consistent disagreement with the concave downward curve determined from experiment.

One possible reason for this discrepancy is that the model does not include the probe response in air in the absence of a specimen, i.e., the term  $T_0$  mentioned above. If this term were added to the calculation, the dotted curves in Figures 16 and 17 would change shape, which could result in a different behavior for the zero crossing time. However, the fact that similar, concave upward curves like that in Figure 18 have been obtained for different excitation waveforms, which also changes the shape of the dotted curve, would seem to indicate that the problem lies with the flaw signal rather than the no-flaw response.

In particular, the fact that this model predicts no significant change in the shape of the flaw signal as flaw size is varied could very well be an artifact of the small flaw approximation which forms the basis for this model of a rectangular slot. From other calculations of the behavior of continuous-wave eddy currents at corners and around crack tips, one expects that there is a depletion of current density near the slot on the surface of the specimen, and an enhancement of current density at the slot tip. Neither of these so-called "Kahn effects" are predicted

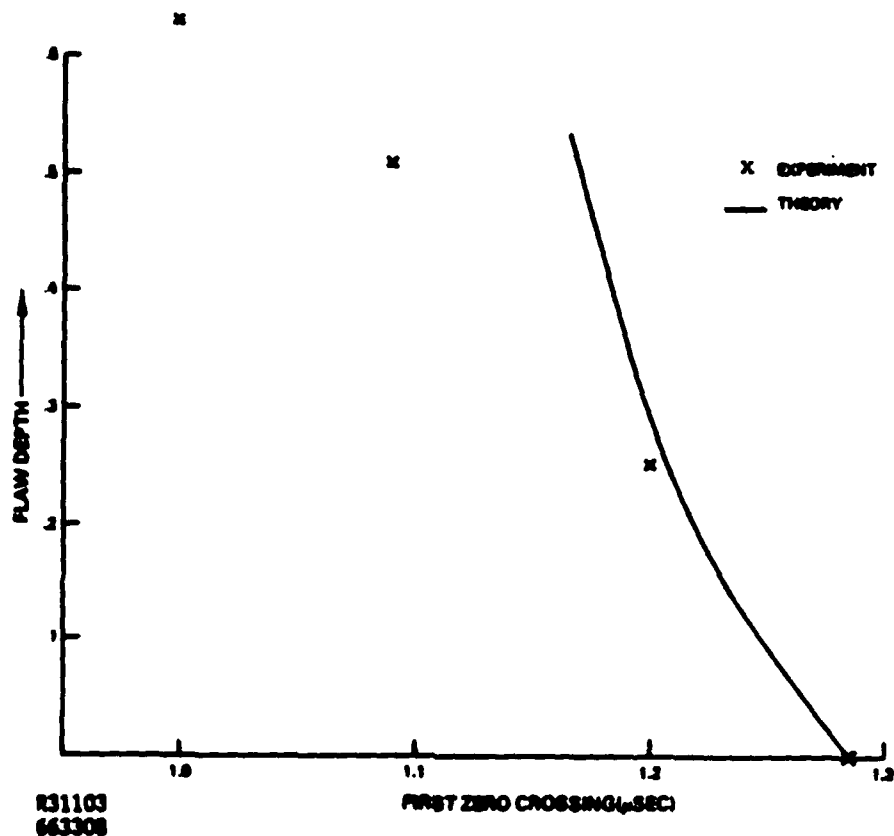


Figure 18. Calculated and Measured Zero-Crossing Times as a Function of Flaw Depth. Failure of the theory to predict the correct behavior for larger flaws is attributed to the small flaw approximation inherent in the model.

by the small flaw theory. As a result, it is believed that the theory used here tends to overestimate the effects of near-surface current perturbations while underestimating the effect of perturbation at the slot tip. If this is the case, then a more realistic treatment of the interaction of eddy currents with extended flaws could lead to flaw response curves that change shape as well as magnitude as flaw size is increased. Our experience with calculations like those discussed here leads us to believe that this is the most likely explanation for the difference between theory and experiment shown in Figure 18. Unfortunately, the basic theory of eddy current/flaw interactions has not progressed to the point where more realistic calculations are feasible.

### 3.5 Slot Tip Effects - Theory

Although theory cannot provide a definitive answer concerning the relative intensity of near-surface and crack tip signals, it is possible to make some "worst case" and "best case" estimates of such effects based on simple extensions of the point flaw model.

One such result is shown in Figure 19. For this calculation, the integrated point flow model described in the preceding section was used. This is a "worst case" model because it ignores the fact that current is forced to flow down the crack face away from the surface, which would emphasize crack tip effects at the expense of near-surface effects. The integrated point flow model is therefore expected to overemphasize near-surface perturbations caused by a crack.

The calculated results shown in Figure 19 confirm that this is indeed the case. The curves shown here are the input waveform (dotted curve) which is 1.0  $\mu$ sec in width with 50 nsec rise and fall times, and the flaw response function (solid curve), both normalized to unity at their peak values. The significant point here is that the integrated point flow model predicts response functions of exactly the same shape for slot depths ranging from 0.005 to 0.020 in. In other words, this model predicts that near-surface effects dominate to such an extent that crack depth effects cannot be measured.

At the other extreme, one might assume that the current perturbation at the crack tip dominates and that near-surface effects are negligible. This so-called crack tip model gives the results shown in Figure 20 for the same input pulse used in Figure 19. In this case, a very distinct shift in decay times is obtained as slot depth is varied, indicating that depth information can be obtained from an analysis of pulse decay characteristics.

There are two additional points to be made concerning Figure 20. One is that signal rise times are also depth dependent and that pulse buildup data can be used just as well as decay data to infer crack depth. The second point is that decay or rise time characteristics are used to infer depth rather than peak arrival times, as was the case in Figure 13. This is a distinct advantage because rise and fall characteristics are observed over times of the order of hundreds of nanoseconds, whereas peak arrival times occur in tens of nanoseconds. Thus, for the particular pulse shape shown in Figure 20, differences in decay characteristics are easily recognized, while peak arrival time differences cannot be seen.

The main question, however, remains unanswered at this point. The integrated point flow model used in Figure 19 indicates that depth information cannot be measured, while the "best case" model, the crack tip calculation, says that crack depth is easily inferred from the rise and fall time characteristics of the reflected signal. Furthermore, both calculations are suspect because both are based on simplified extensions of the point flow theory. Clearly, then, this situation calls for an experimental study of signals produced by flaws of different depths to determine which of the two models is more nearly correct, i.e., to determine if flaw signals are dominated by near-surface scattering or if crack tip effects are measurable.

Before presenting the experimental results, it is important to note that experiments with open slots are likely to involve smaller time shifts than experiments with closed cracks. The reason is illustrated in Figure 21

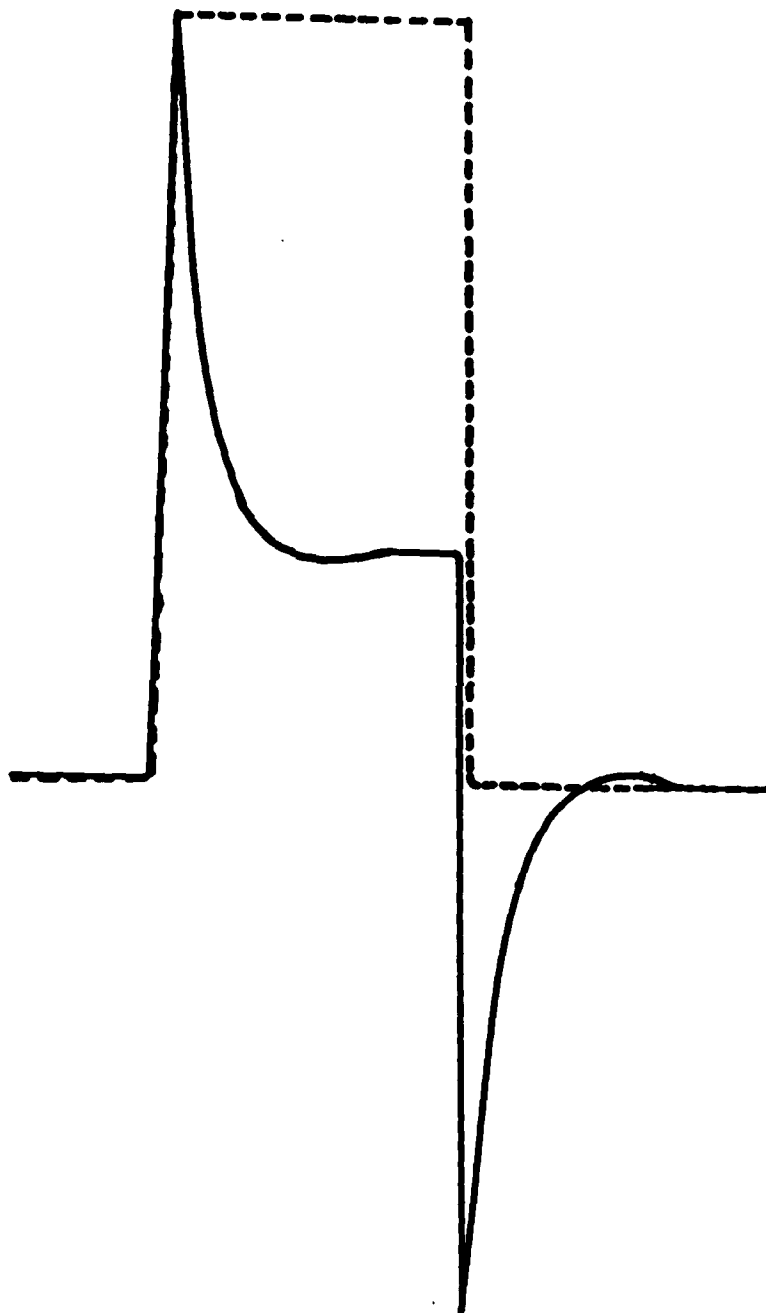


Figure 19. Flaw Response Based on an Integrated Point Flaw Model. The input current (dashed curve) is of 1  $\mu$ sec duration, with 50 nsec rise and fall times. The flaw response function (solid curve) is dominated by near-surface scattering and is the same for slot depths ranging from 5 to 20 mils.

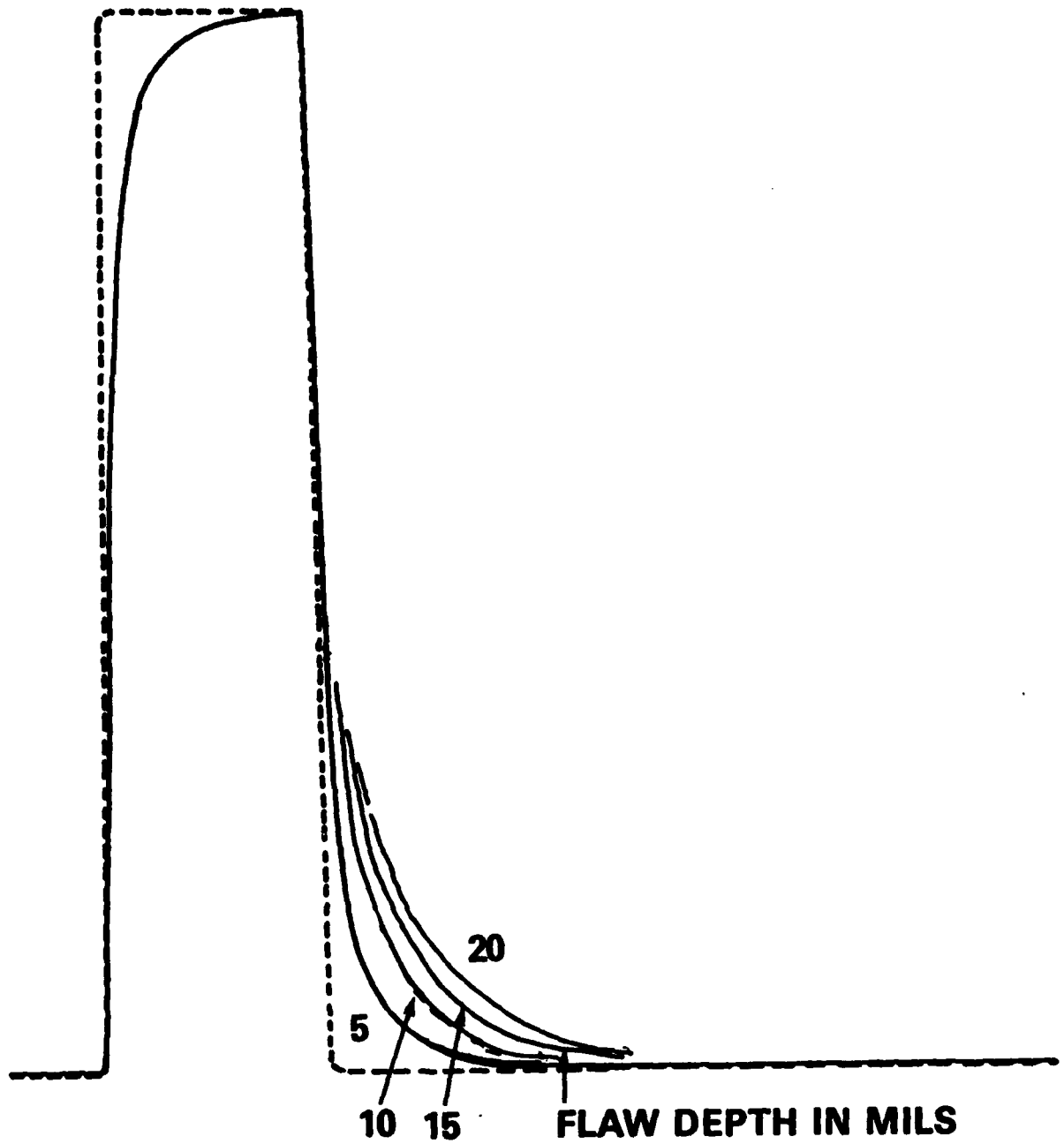
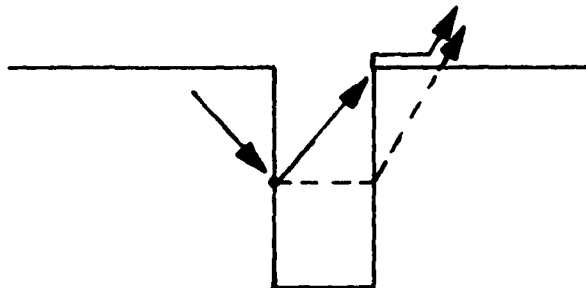


Figure 20. Flaw Response Based on a Crack Tip Model, for the Same Input Pulse as Used in Figure 18. Significant differences in decay characteristics of response functions are noted for crack tips at different depths.

OPEN CRACK



CLOSED CRACK

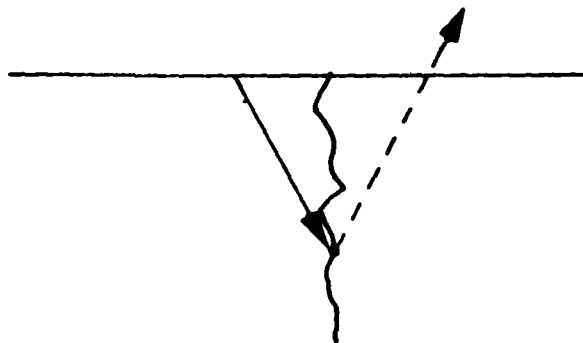


Figure 21. Signal Propagation Paths for Open and Closed Cracks. For a closed crack, with the propagation path through the metal, the arrival time of a signal from a crack tip will be later than the arrival time from an open crack tip.

which shows possible signal propagation paths for open and closed flaws. Part of the signal from an open crack (slot) will arrive at an earlier time than the signal from a closed crack of the same depth because, in the case of an open slot, the signal can return along a path that is mostly in air. In the analysis of experimentally observed time shifts for open slots, one should therefore interpret the data as indicative of a single propagation path through the metal from transmitter to flaw with a return path in air involving no time delay. Thus, if slot tip scattering is significant, time shifts should approximate the time required for a signal to propagate through the metal to the slot tip. If, on the other hand, near-surface scattering dominates, then measured time shifts should be much smaller than the transmitter-to-slot tip propagation time.

To provide a basis for analyzing experimental data in this way, an analytic solution was developed for eddy currents induced by dipole source in an infinite conductor. This solution leads to the expression

$$t_p = \frac{\mu_0 \sigma R^2}{6.52} \quad (1)$$

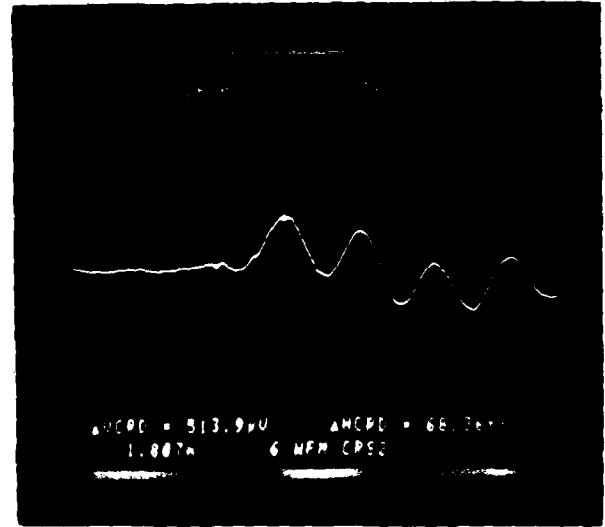
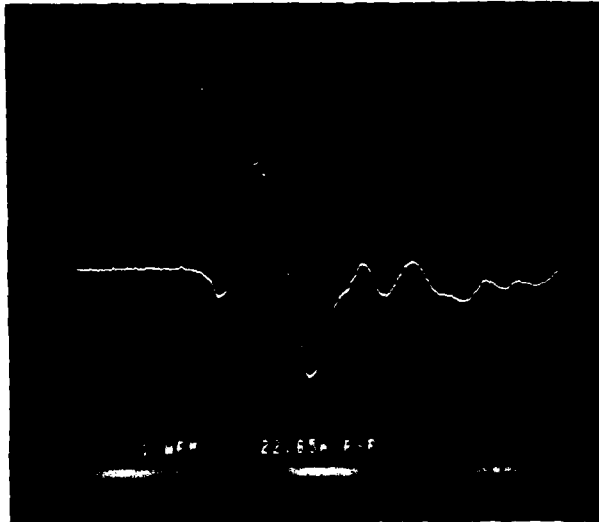
for the time required for the current peak to propagate a distance R in a medium with conductivity  $\sigma$  (MKS units).

### 3.6 Slot Tip Effects - Experiment

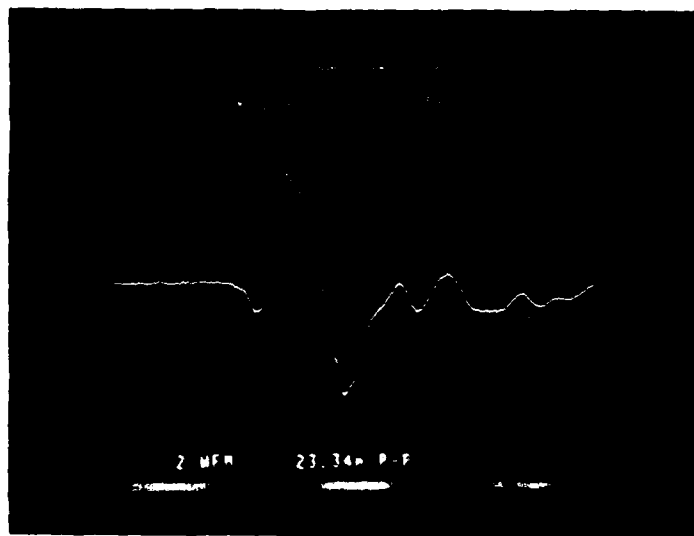
A series of experiments was carried out to determine if any time resolved flaw information is available with the PEC breadboard arrangement, in particular to find out if any information from eddy current concentration at the crack tip is available on the time scales implied by the above equation. Transmitter probe T4, a ferrite-shielded probe with only 20 turns of #38 gage wire, in order to minimize phase distortion, was used, with a receiver of 30 turns of #38 gauge wire. The titanium test specimen used has a series of EDM notches of constant length (1.25 mm) and width (0.13 mm) but varying depth from 1.25 mm to 0.08 mm. Since the surface area of each flaw is the same, the integrated point flaw model predicts no variation in flaw response. A pulse length of approximately 150 nsec was used.

Figure 22 shows a sample experiment with the received signal in the absence of a flaw and over the 1.25 mm deep flaw. The shapes are similar and, in fact, the peak arrival time does not vary substantially. However, the decay of the signal between this peak and the first zero-crossing does exhibit a variation as the probe is moved from unflawed to flawed region, and the decay varies with flaw depth. This result is seen more clearly in Figure 22(c) in which the no-flaw signal is subtracted from the flaw signal, and the result smoothed.

The difference signals were smoothed with a low pass filter with a cutoff frequency of approximately 8 MHz. The filtered difference signals exhibit peaks that decrease in phase as well as amplitude as the flaw depth decreases. Figure 23 shows the peak arrival time as a function of



(a) Signal in the Absence of a Flaw (b) Signal in the Presence of a Flaw



(c) Filtered Difference Signal

Figure 22. Received Pulse in the Absence of a Flaw (a) Received Pulse With Probe Positioned to Maximize the Flaw Signal (b)

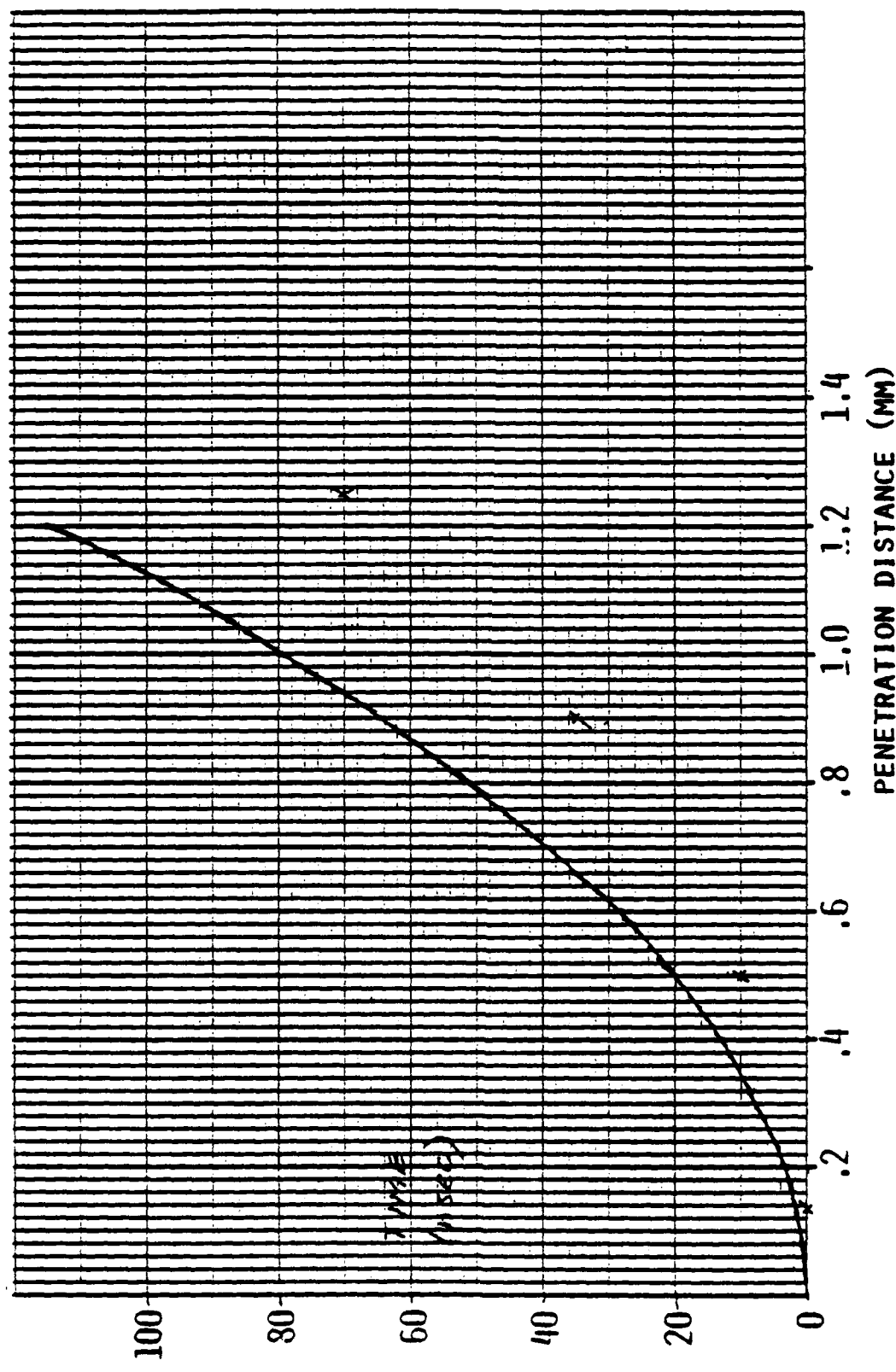


Figure 23. Flaw Signal Peak Arrival Time Vs Flaw Depth as Measured (x's) Agrees With the Time Required for an Eddy Current Pulse to Diffuse to the Crack Tip (solid curve)

flaw depth. Also shown is a curve of the time for an eddy current pulse to penetrate from the surface to a depth equal to the flaw depth, from Eq. 1. The measured times agree with the curve within a factor of two.

Furthermore, the general shapes (convexity) of the curves are similar: they both exhibit time dependence that is proportional to the square of penetration depth. This correct dependence confirms that the times measured are indeed indicative of eddy current penetration dynamics.

This experiment indicates that flaw depth information, in addition to surface information, is present with appropriate signal processing. Furthermore, it shows behavior that agrees, at least qualitatively, with that expected from the Kahn effect, indicating that correct modeling of the flaw signal requires abandoning the point flaw model assumptions. Finally, the experiment and theory suggest that the flaw depth information may be enhanced by reducing the direct coupling between the transmitter and receiver during the time in which the defect tip signal reaches the receiver.

### 3.7 Conclusion

Experimental evidence and theoretical calculations have confirmed that defect depth information for surface-breaking flaws is available from PEC receiver signals. This information is related to the arrival time of the signal from eddy current concentration at the flaw tip. Because the information is interpreted from time, rather than amplitude data, the measurement should be relatively insensitive to liftoff variation.

It should be pointed out that this viewpoint is not in conflict with some previous observations. Waidelich (11) has observed empirically that deeper flaws in aluminum influence the received signal at later times than more shallow flaws. Morris (12) observed, also empirically, that defect depth correlated well with the observed time at which the flaw and no-flaw signals are equal. This approach may be similar to measuring the change in decay time of the transmitted pulse. These past observations have not been previously explained quantitatively in terms of eddy current paths, however.

Consideration of this time-domain information leads to the question of how best to exploit it to maximize the desired signal strength. The approach taken in this project has been to take advantage of the time-domain nature of the signal by separating in time the depth information from the surface flaw information and no-flaw signal. That is, if signal transmission could be halted or severely diminished before the flaw depth signal arrives, then the signal-to-noise ratio could be improved.

One possible current pulse shape is a ramp, as shown in Figure 24(a). In fact, Hendrickson and Hansen (13) have suggested this as a way to generate deeply penetrating eddy currents, then to receive signals from their decay. The difficulty of this approach, compared to the bipolar pulses used for the experiment previously described, is that it is impractical to stop the current flow in the excitor coil in a time short compared to the arrival time expected for small flaws in low conductivity material - tens of nanoseconds in titanium.

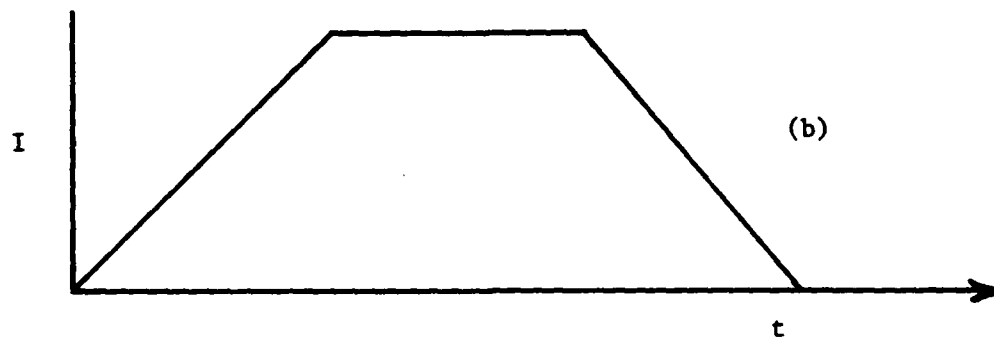
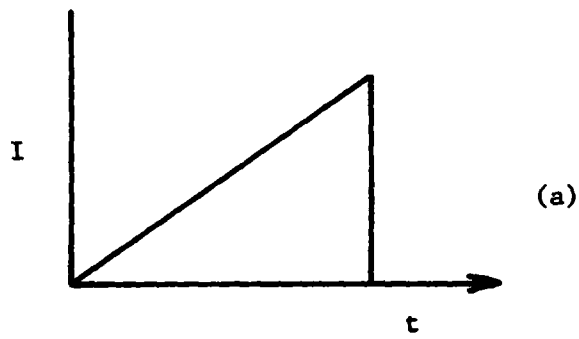


Figure 24. Ideal Current Waveforms for Achieving Time-Domain Separation of Surface Signals and Flaw Depth Information. In case (b), a sharp change in current is not required even though signal transmission stops as quickly as in (a).

The reason is that the coil, if made capable of supplying a large signal, must have substantial inductance (of the order of 1 microhenry). The e-folding time to remove the current in an inductor through a resistance is  $L/R$ . Therefore, a resistance of .01 ohm is required to passively remove approximately 2/3 of the current in 10 nanoseconds. This is a factor of ten less than typical coil resistances, and ignores cable and winding capacitance. Alternatively, a back voltage could be applied to the probe, but the magnitude of this voltage is inversely proportional to the decay time desired. In other words, if the desired decay time is one tenth of the rise time, then the decay portion applied voltage must be 10 times the rise portion voltage. This operation mode would require the use of fewer turns of heavily insulated wire, and thereby reduce the transmitted power.

Therefore, the selected approach for this project is to use the waveform shown in Figure 24(b). When the current reaches the top of the ramp, it is held constant for a time long enough to take the desired measurements. In this manner, the de-energizing of the probe can take place after the measurement is taken, at a moderate rate consistent with its own impedance. The voltage induced in the test material, however, according to Faraday's Law, is proportional to the rate of change of current, and therefore decays in the time that it takes to change the probe current from a ramp to a constant value. This selected approach is described in the following section.

## 4. ADVANCED SYSTEM DESIGN

### 4.1 Breadboard Development

The original breadboard system was modified to test the time domain signal processing concepts evaluated in the latter part of this project. As modified, the breadboard system consists of a Texas Instruments Model 6613 pulse generator, a voltage-to-current pulse amplifier, a Hewlett Packard Model 9826 computer, a Tektronix Model 7854 digital oscilloscope, and a Princeton Applied Research Model 115 wideband preamplifier. In addition, the mechanical scanning system was modified to provide digital read-out of position in one axis at approximately 0.0005 inch resolution. The modified breadboard system is shown in Figure 25. In this system, the only components not commercially available are the probes and the voltage-to-current amplifier, although the amplifier was constructed out of commercially available discrete components.

The pulse generator was selected because it can provide continuously variable pulse risetime, falltime, and duration, with each parameter continuously variable and independently controllable from 10 nanoseconds to at least 1 millisecond. The output is a voltage pulse of up to 5 volts peak amplitude into 50 ohms resistance.

The pulse generator signal is amplified by the voltage-to-current amplifier that was designed for this project at SwRI. The amplifier is a wideband (approximately 50-MHz) device capable of delivering at least 2.5 Amperes into a load impedance varying from 0 to more than 100 Ohms. This is achieved at the cost of a low pulse repetition rate: approximately 300 pulses per second at the maximum current. The current pulse shape is maintained close to that of the input voltage by the use of a feedback circuit that directly senses the current delivered to the probe. This amplifier is described in greater detail and its circuit schematic is presented in Appendix D.

The received signal is amplified by a PARC Model 115 wideband pre-amplifier. The 50 Ohm input impedance of the preamplifier effectively dampens the receiver probe response. The amplified signal is input to the digital oscilloscope, which also serves as the transient recorder/digitizer for the system. The oscilloscope is directly connected to the HP 9826 minicomputer via a standard General Purpose Interface Bus (GPB). The oscilloscope waveform acquisition and signal pre-processing can be controlled by the oscilloscope keyboard or the signal acquisition program written for the HP 9826. Signal processing performed in the oscilloscope includes multiple signal acquisition and averaging. This function takes the place of the boxcar averager in the original breadboard configuration. Since the oscilloscope reconstructs a high frequency waveform by repetitive random sampling of multiple waveforms, it does not allow a continuous scan to be made of the signal at one point in time. Hardcopy output is provided by a thermal printer attached to the HP 9826.

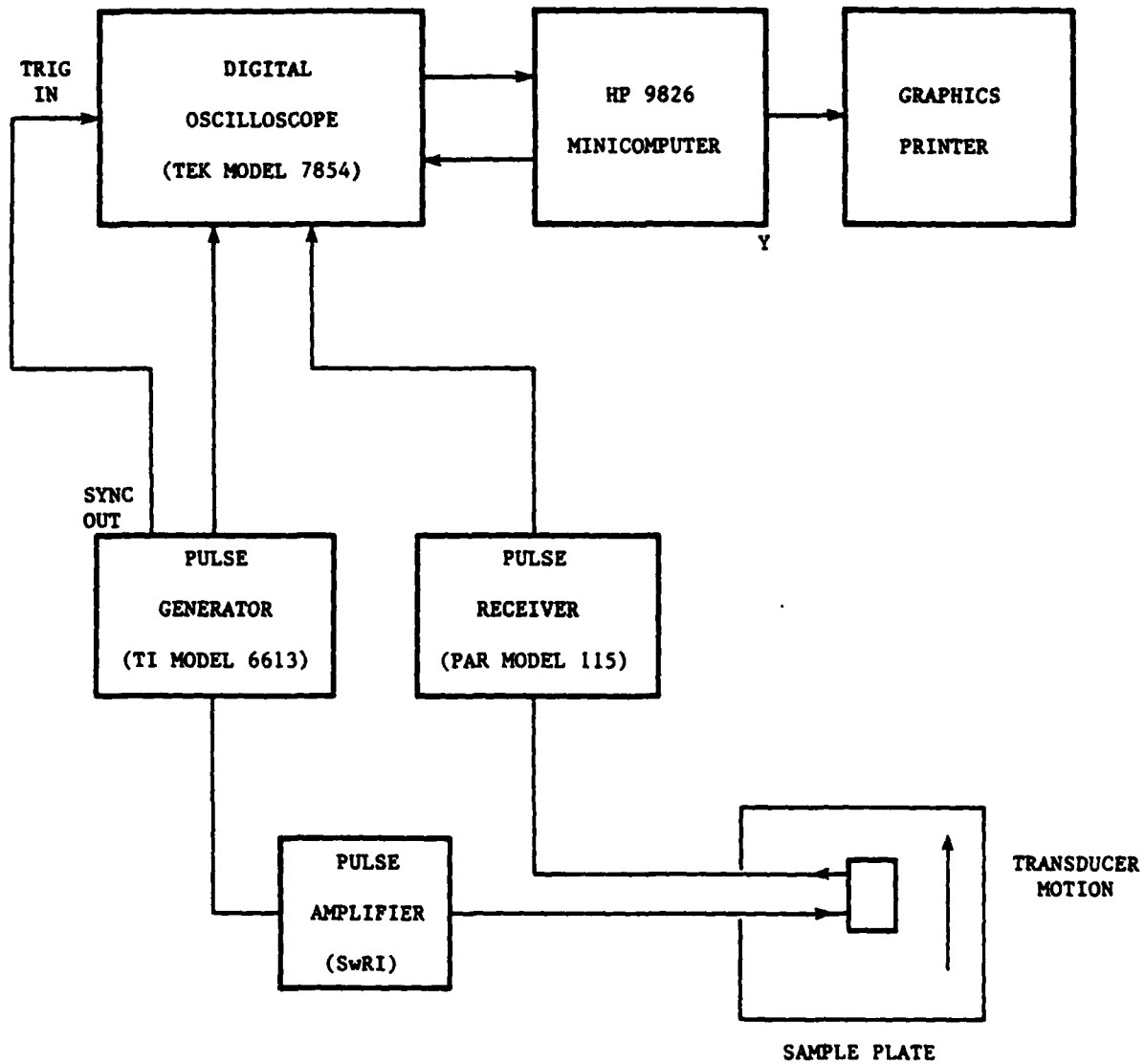


Figure 25. The Modified Pulsed Eddy Current Test System. This breadboard system has been constructed to allow use of monopolar pulses with variable rise/fall times and duration, and more flexible (software controlled) feature extraction. Only the SwRI-constructed voltage-to-current pulse amplifier is not commercially available.

This breadboard system provides greater flexibility in pulse shaping and signal processing at the cost of reduced probe current, reduced pulse repetition rates, and inability to provide real time scans of flaws specimens. The limited peak current of 2.5 amperes compares to more than 7 amperes typically available with probes connected to the Velonex pulser, where the current was effectively limited only by the need to maintain the peak voltage below the arcing point of the probe windings. Thus, the flaw detection capability was sacrificed and cannot be directly compared with that of the original pulsed eddy current breadboard system or the conventional eddy current system.

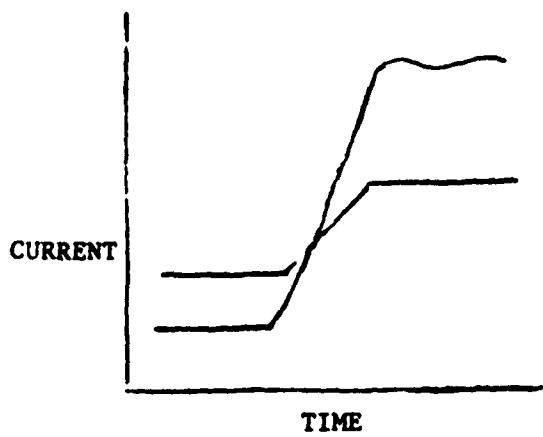
Figure 26 shows the pulse quality available through a one-half turn coil of wire, essentially a short circuit. The bottom trace is the input voltage waveform, and the top trace is the output current, at one ampere per division. The horizontal scale is 500 nanoseconds per division.

#### 4.2 Probe Development

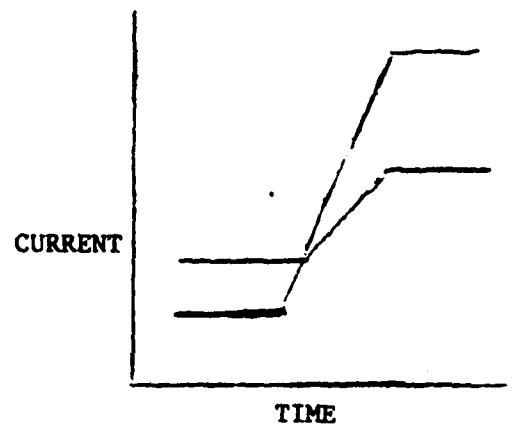
Transmitter probe response to the pulsing system was studied. There were two areas of concern. One is that the voltage swings necessary to drive the probe at the desired waveform be kept below the limited capability of the pulser (less than 200 volts). Second is the desire to make the probe coil current follow the pulser output current. These two currents may not be equal because capacitance in the probe cable and coil itself will shunt part of the current. It has been experimentally observed that a lower resonant frequency causes greater output voltage swings and thus reduces the ability of the feedback circuit to track the input current. Figures 27(a) and 27(b) show this effect for a 6-MHz resonant frequency probe [Figure 27(a)] and a 14-MHz probe [Figure 27(b)].



Figure 26. Input Voltage Waveform (Bottom Trace) and Output Current Waveform (1 Ampere per Division) of the Voltage-to-Current Amplifier. Output is through a one-half turn, one-half inch long coil of wire.



(a)



(b)

Figure 27. Probe Current (Upper Trace) Follows Input Voltage (Lower Trace) Better When a Probe With a Higher Resonant Frequency [(b), 14.3 MHz] Probe is Used than When a Lower Resonant Frequency Probe [(a), 6 MHz] is used. Probes have similar construction, but use different cables. The pulse rise time is 400 nanoseconds.

In order to study the coil response to an ideal probe input waveform, the probe was modeled as a capacitance in series with an inductance. The result for the difference between current into the probe and through the coil is

$$I = I_0 - \frac{\sin \omega_0 t}{\omega_0 T} \frac{\sin \omega_0 T}{\omega_0 T} \cos \omega_0 (t-T) \\ + 1 - \frac{\cos \omega_0 T}{\omega_0 T} \sin \omega_0 (t-T)$$

where  $\omega_0$  is the resonant frequency of the probe in radians per second [ $\omega_0^2 = 1/(LC)$ ],  $T$  is the duration of the ramp,  $t$  is time since beginning of the pulse, and  $I_0$  is the current in amperes at the end of the ramp portion of the pulse and during the constant portion.

This analysis indicates that in order for the coil current to accurately track the pulser output, the following condition must be met:

$$fT \gg \frac{1}{2}$$

where  $f = \omega_0/2\pi$  is the resonant frequency in Hertz.

An effective way to increase the probe resonant frequency (and bandwidth) without decreasing its transmitting power is to reduce the capacitance of the pulser-to-coil cable. Figure 28 shows the effect of cable capacitance for probe T4 (20 turns of #38 gage wire on a ferrite core, ferrite shielded). Without a cable, the apparent inductance of the probe is almost constant to 15 MHz. With standard 50-ohm impedance RG/U 174 cable, the resonant frequency is lowered to 10 MHz. This cable has a nominal capacitance of 30.8 pf per foot. With RG/U 62B cable at 13 pf per foot, the resonant frequency is increased to 14 MHz. Finally, with the use of a low capacitance cable (RG/U-114A) rated at 10 pf per foot, the probe has a resonance at 17 MHz. It was decided to use RG/U 62B cable for probe development efforts because the marginal improvement of the R6/U-114 cable is offset by greater bulk, stiffness, and electrical noise.

Figure 29 shows the current waveform that is achievable with the 10-MHz probe, using a 250-nanosecond ramp, and the resulting power spectrum. It is seen that the input power intensity is negligible for radial frequencies above  $\pi/T$ . Figure 30 shows in comparison the ideal frequency magnitude spectrum. The magnitude peaks above the first zero actually represent only 1 percent of peak power. Therefore, it is concluded that probes can be constructed to allow the pulsing unit to deliver a reasonably accurate waveform to the transmitter probe coil.

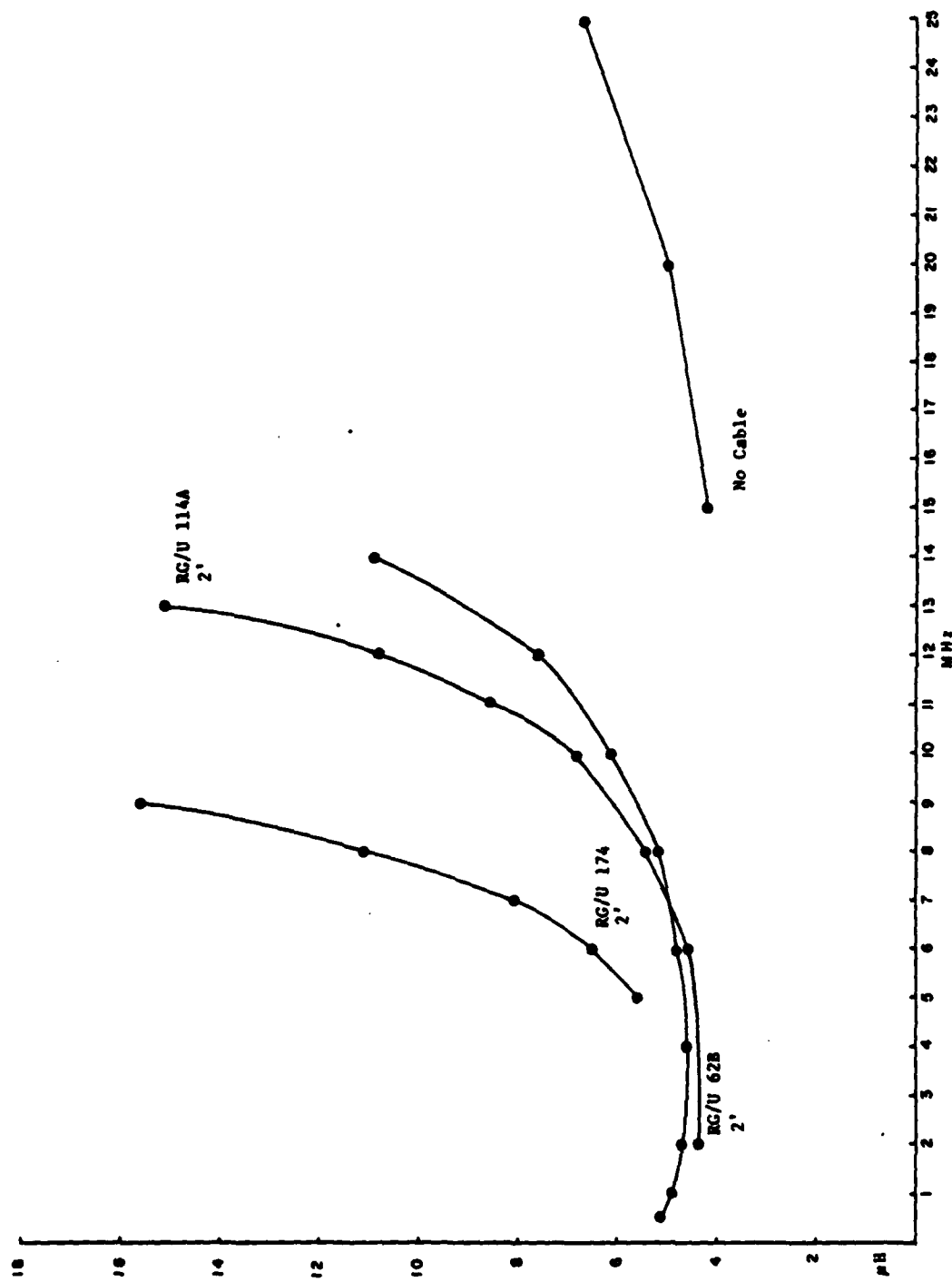


Figure 28. The Variation of Observed Inductance of a Single Transmitter Coil as a Function of Frequency, When Measured With Short Leads and With 2 Feet of Different Coaxial Cables. The cable substantially decreases probe bandwidth, but this effect may be minimized by use of low-capacitance cable (RG-62B or RG-114A).

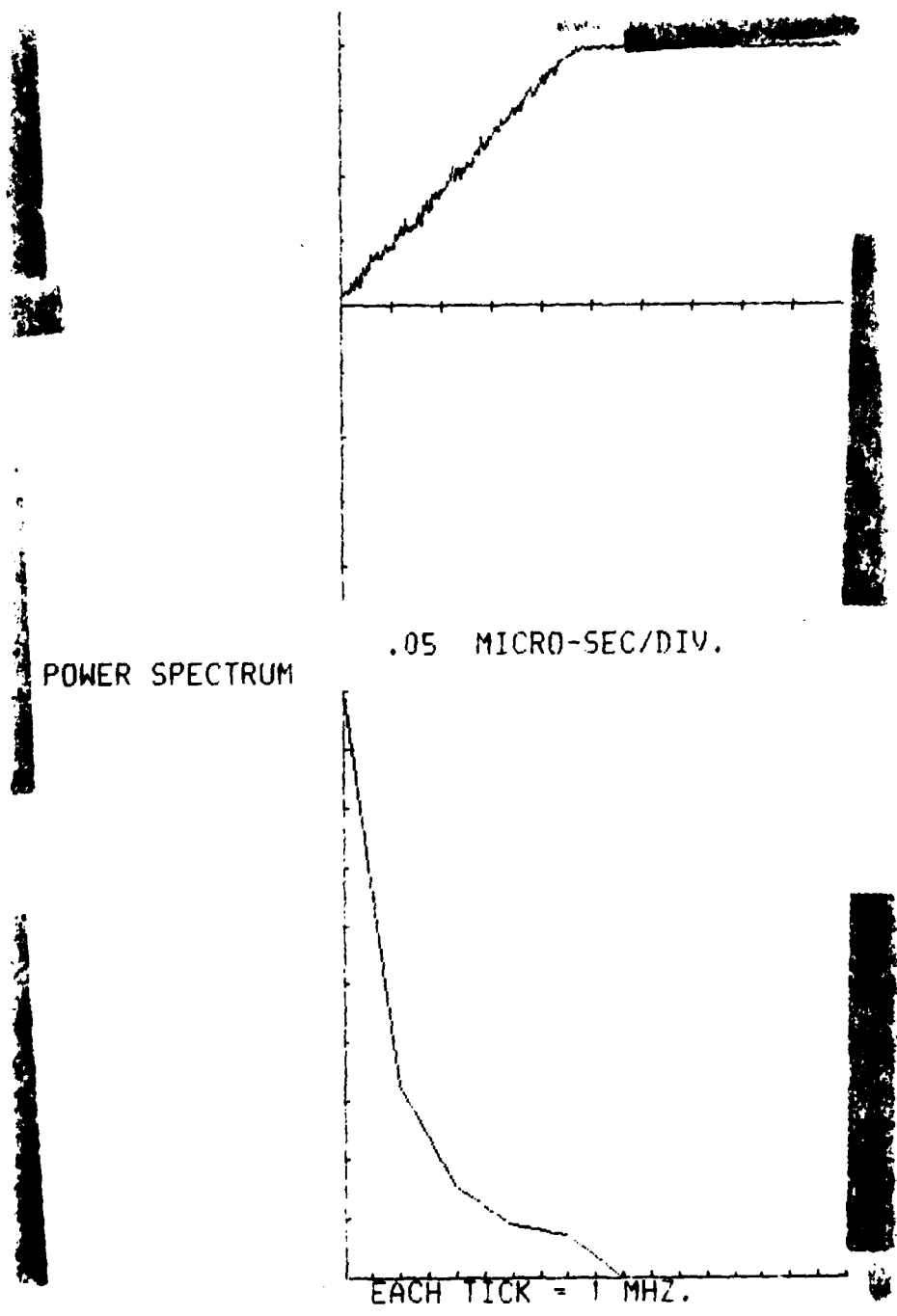


Figure 29. Actual Current Waveform and Power Spectrum Obtainable With a 10-MHz Probe

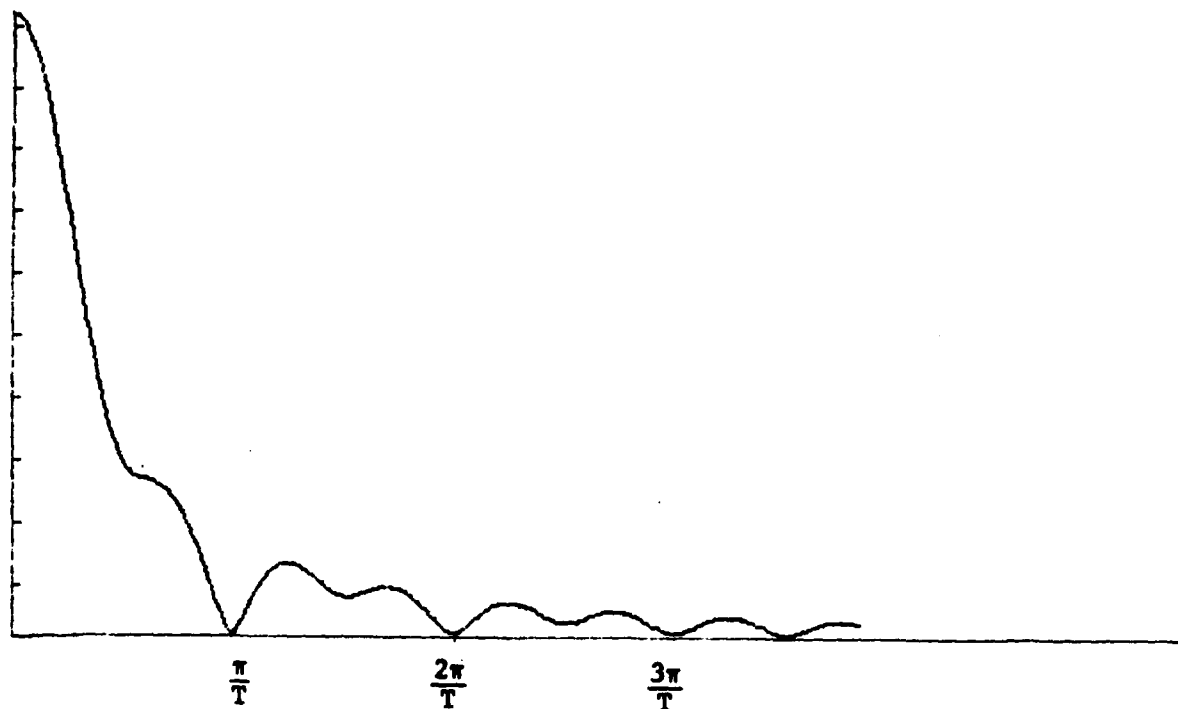


Figure 30. Magnitude of the Fourier Transform of the Ideal Transmitter Current Waveform  $T$  is the Duration of the Ramp Portion. Note that at frequencies above the first zero, the peak magnitude is 10% of the first peak, so the energy is only 1 percent.

### 4.3 Evaluation Results

Tests were conducted with the new pulsing system and transmitter probe T4 modified with the low capacitance coaxial cable and the addition of an absolute receiver coil placed parallel to the transmitter. As in previous experiments, the receiver coil was aligned first visually and then by minimizing the transmitter-to-receiver coupling when placed over an unflawed surface.

A sample of test results is shown in Figures 31 and 32. Figure 31 shows the receiver signal in the absence of a flaw, during the ramp and constant value portions of the transmitted signal. Figure 32 waveforms are the difference between a flaw signal and the no-flaw signal of Figure 31. This approach is similar to that of Section 3; however in this case the resulting curve is not smoothed. It is seen that with the use of this new pulse shape, the difference in decay characteristics predicted by the crack tip model as shown in Figure 20 can now be directly observed. Figure 33 shows the inverse of the slope of the decay portion of the curve as a function of flaw depth. The inverse slope is used because this quantity is a measure of the time delay of the signal in reaching any given value, and should therefore increase with flaw depth. It is seen that flaw depth corresponds to this measured parameter, in agreement with the crack-tip model calculations shown in Figure 20. A more quantitative comparison is difficult to make because of the variation between ideal and achieved pulse shapes.

Two encouraging observations can be made from these results. First, the basic predictions made from the crack tip model have been confirmed. Second, this result has suggested a way to measure flaw depth that appears to be more sensitive than that used in Section 3. In this approach, the smallest target flaw appears on the scale, with a finite time, in contrast to the result obtained with the initial breadboard system, in which the measured time delay of the 0.005-inch deep flaw was 0.

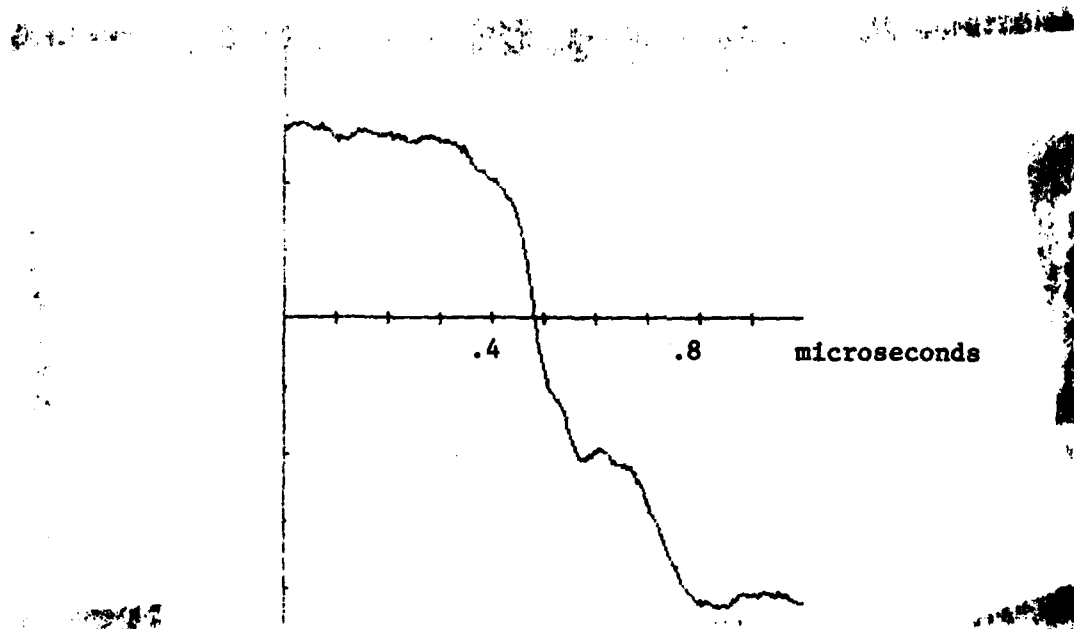


Figure 31. The No-Flow Receiver Signal Used in a Series of Flaw Depth Measurement Tests. The amplitude drops sharply when the transmitted current becomes constant.

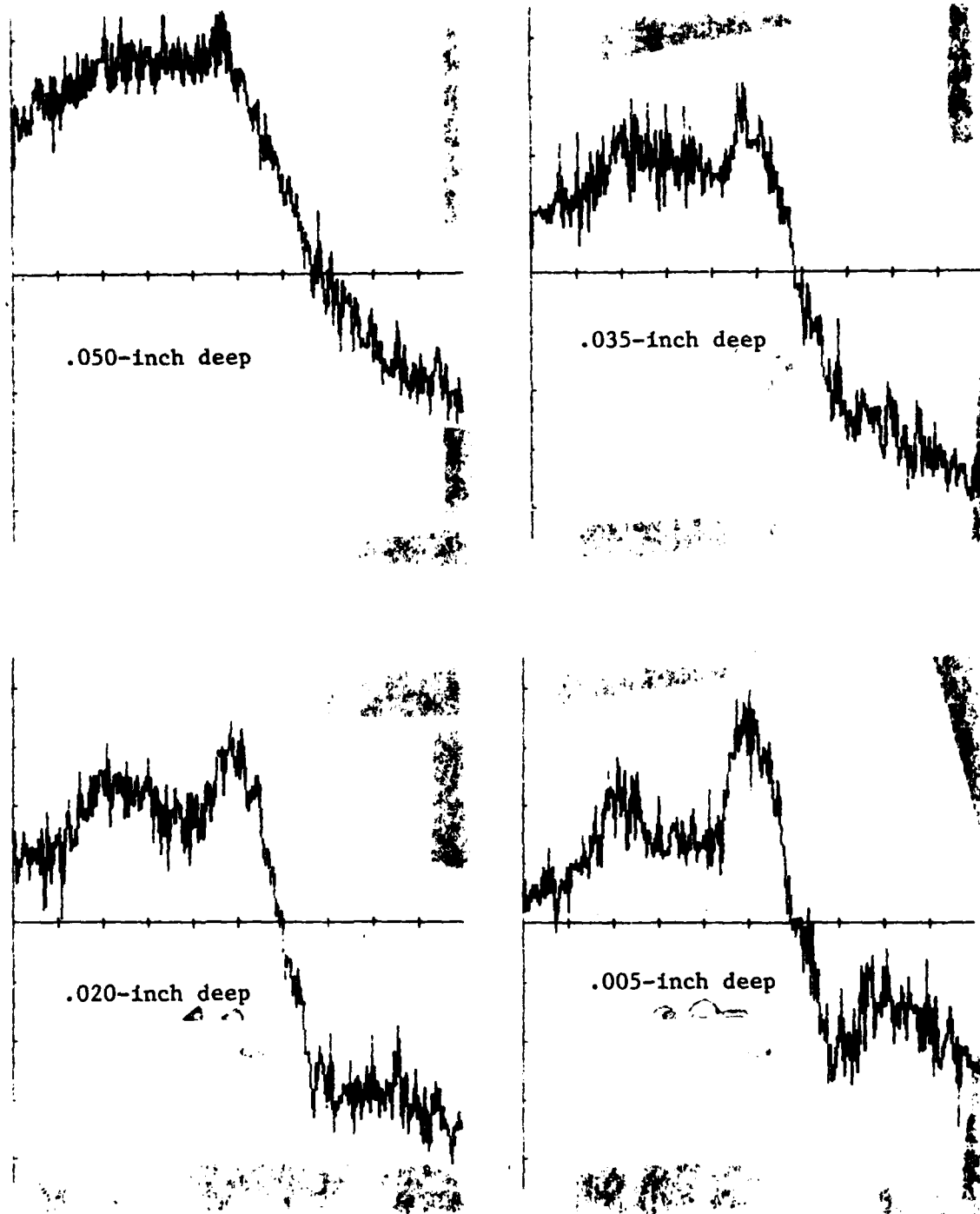


Figure 32. Receiver Flaw Minus No-Flaw Signal, for Different Depth Notches. The slope of the decaying portion of the signal decreases with increasing flaw depth, as predicted by the crack-tip model results of Figure 20.

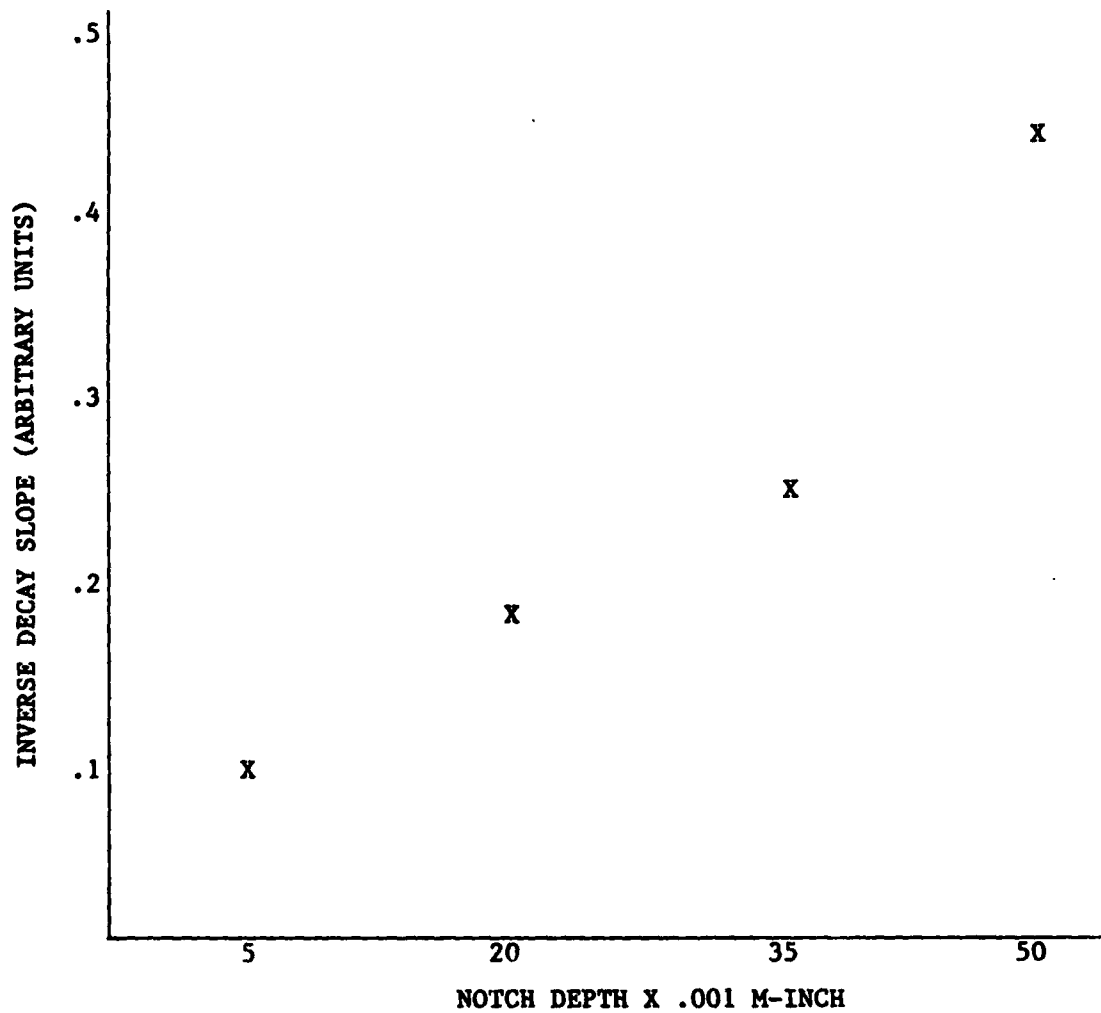


Figure 33. Inverse of the Slope of the Decay Portion of Flaw waveforms shown in Figure 32. The curve is similar to that obtained from the bipolar pulse shown in Figure 23 confirming the presence of depth information on an eddy current diffusion time scale.

## 5. COMPARISON WITH C-W RESULTS

A conventional eddy current analysis was carried out on the flaw samples in order to provide a comparison between current state-of-the-art practice and PEC testing capability as developed in this project. The eddy current instrument used was a Nortec NDT-19. This instrument is a single frequency device, with a maximum frequency of 4.6 MHz. The probe used was a Nortec SP-5000. This probe is a conventional absolute probe with windings parallel to the surface. Throughout the experiments, the auto balance mode of the NDT-19 was used to null the probe.

The test fixture of the modified PEC breadboard system was used to hold the probe. During initial experiments, it was found that surface variation in the test specimens created substantial liftoff signal variation, so the probe fixture was modified to maintain constant probe contact with the surface by spring-loading the probe.

Tests were conducted by performing a series of scans in the Y-direction, that is, parallel to the length of the specimen blocks. At the end of each Y-scan, the probe position was incremented 0.025-inch in the X-direction before another Y-scan was conducted. Limit switches on the test fixture provided signals to the data acquisition equipment to ensure that each Y-scan started and ended at the same value of X.

The eddy current instrument was adjusted such that the initial liftoff signal was in the horizontal left, or -H, direction. This allowed the vertical component of the signal to be used as the indicator of flaw characteristics. This approach makes the vertical signal more sensitive to flaws. Both horizontal and vertical components of the instrument impedance plane display were sent to the data acquisition system. Data acquisition and processing were conducted by the use of a Biomation digitizer connected to a Data General Nova series computer.

Several different presentation formats were developed. Figure 34 shows two representations of flaws A through D on the T1-6-4 surface flaw detection standard. This figure was produced by a single scan in the Y-direction through the center of each flaw. The flaws are all 0.010-inch long by 0.005-inch wide. The depths of flaw A through D are, respectively, 0.050, 0.035, 0.020, and 0.005-inch. Flaw E, which is 0.003-inch deep, was not detectable. Figure 34(a) is a re-creation of the impedance plane display of the eddy current instrument. Figure 34(b) shows the separate horizontal and vertical components of the impedance plane display as a function of scan position. In both presentation forms, it is seen that the response of flaws A, B, and C is very similar.

Figure 35 shows a plan view created by presenting the vertical component of the impedance plane for a series of scans over the same flaws as shown in Figure 34. It should be noted that each plan view in the figure was automatically scaled by a different factor in order to maximize resolution in the digital-to-analog converter. The actual signal level represented

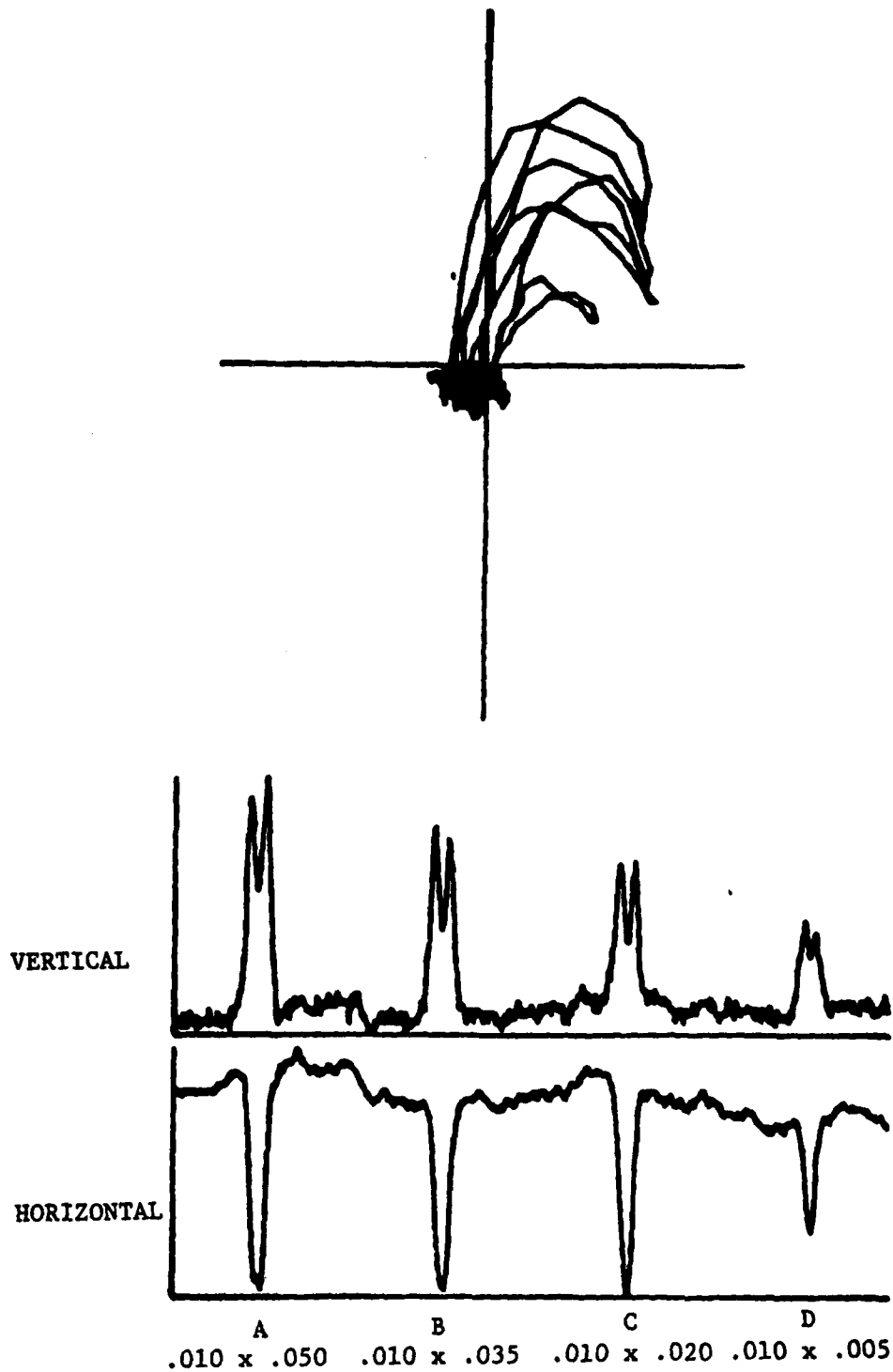


Figure 34. Conventional Eddy Current Scans of Flaws A Through D on the Surface Flaw Detection Standard (E is not Detectable). Top figure is computer reconstruction of eddy current instrument impedance plane display. Bottom figure is separate plots of vertical and horizontal impedance plane components. The axes are adjusted such that liftoff is in the negative horizontal direction. The flaw signature is similar for flaws A, B, and C, which have equal surface areas, but depths varying from 0.050 to 0.020 inch.



in each view is proportional to the maximum signal level in that view, shown at the bottom of each scan view. From these scans, it is seen that the maximum flaw signal occurs when the probe is centered over the end of the flaw. When the probe is centered over the middle of the flaw, the eddy currents are not as disturbed, because the probe is larger than the flaws, and the eddy current density induced below the center of the probe is small.

Figure 36 shows the same plan view display as described above, for a series of flaws (G, H, I, and J) with a constant aspect ratio of 2 to 1 (length to depth). Flaw F in this series is the same size as Flaw E in the previous series and is also not consistently detectable. It is seen that the variation in response is much more dramatic than for the previous series ABCD, which consists of flaws with equal surface area. This point is illustrated in Figure 37, which shows the maximum response as a function of flaw depth for each series.

Figure 38 shows data from the probe system being developed for the RFC program, for the same set of flaws as in Figure 36. A conventional 2 MHz eddy current coil is used, but it is mounted in an air-bearing probe to provide a relatively constant liftoff. The results are seen to be consistent with those described above. In particular, Flaws G, H, I, and J are easily detectable with increasing signal amplitudes, but Flaw F is not clearly distinguishable from noise.

Two significant observations can be made from this conventional data. First, the conventional system set up in this project is capable of meeting the target-size flaw detection goals set up for the PEC system, and shows flaw detection capability similar to that of the RFC program eddy current system.

Second, the response of the conventional system is approximately the same for flaws of equal surface area, for depths ranging from 0.020-inch (0.5 mm) to 0.050-inch (1.25 mm), and varies substantially with flaw length. Therefore, it is expected that conventional continuous-wave eddy current inspection could be developed to provide an indication of surface-breaking flaw surface area, but it does not appear as promising for flaw depth characterization.



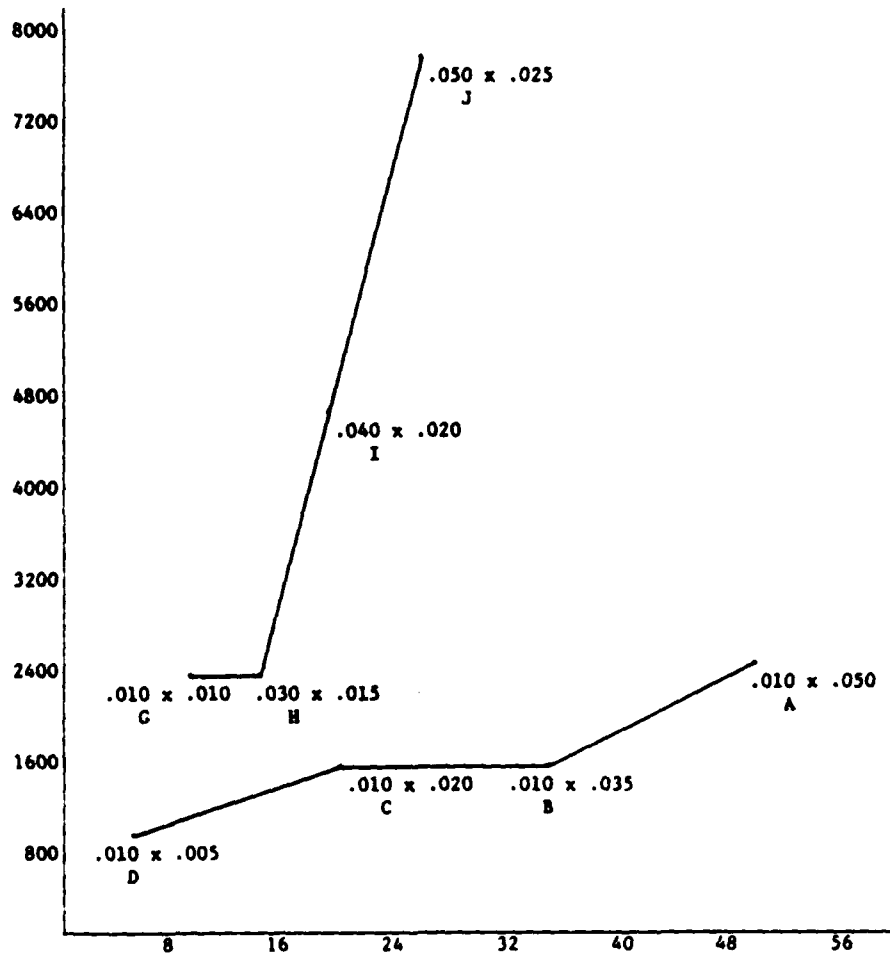


Figure 37. Peak Vertical Signal Response From Conventional Eddy Current Examination. Much less variation is seen for flaw series ABCD (equal surface area) than series GHIJ (equal aspect ratio).

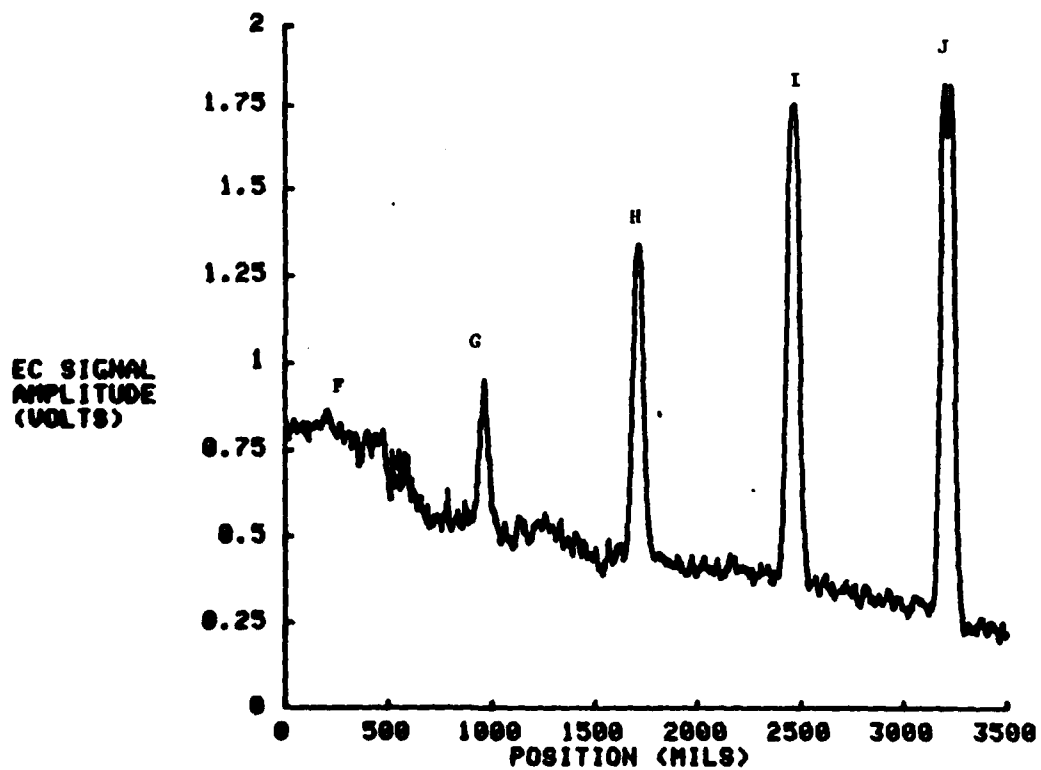


Figure 18. Conventional Eddy Current Scan of the Same Flaws as in Figure 16 using an Air-Bearing Probe Developed by SwRI for RFC. The response is similar to that achieved by the conventional equipment employed in this project.

## 6. CONCLUSIONS AND RECOMMENDATIONS

It has been shown that pulsed eddy current examination is capable of detecting the target flaws in low conductivity alloys, and that it offers a promising way to estimate the depth of surface-breaking flaws.

It has been successfully demonstrated that the pulsed eddy current breadboard system is capable of detecting flaws as small as 0.010 inch by 0.005 inch in a titanium-6-4 surface. The equipment required to set up such a PEC system is commercially available.

By using the unique time-domain characteristics of PEC signals, the correlation receiver flaw signal decay with flaw depth was shown. This is possible because the eddy current density is concentrated at the tip and depleted at the surface of a surface-breaking flaw. Theoretical calculations, when revised to include this Kahn effect, showed reasonable agreement with the measured data for flaw depth.

Because the concept of the depth measurement technique is relatively unexplored, it is recommended that additional research be conducted in this area. Several areas of improvement need to be investigated. First, the breadboard pulsing unit containing the voltage-to-current amplifier needs to deliver larger currents than is now possible at equal or better bandwidth. This would make possible a comparison between the flaw detection capability of the ramp pulse system and the more conventional bipolar pulse system that was set up at the beginning of the project.

Second, theory development should be pursued, in the area of flaw response. The models that were developed did successfully predict the spatial and temporal variation of transmitted magnetic fields due to shielded eddy current probes, but the integrated point flaw model is clearly inadequate to describe flaw signal behavior when flaw characterization is the goal. Even though the eddy current paths of interest are three-dimensional in nature, the authors believe that an appropriate step is to develop an analytical two-dimensional model that could simulate a long crack with a finite depth. This is the simplest model that would self-consistently include the Kahn effect. Theory development in this area may help provide guidance to further probe development for depth measurement, including the use of differential receiver coils.

Third, the depth measurement approach needs to be tried out on naturally-occurring flaws. This test is important, because it is theorized that this measurement depends on the flaw geometry, and not only the flaw surface area, as for example appears to be the case with electric current perturbation and, to a lesser extent, conventional eddy current examination.

## 7. REFERENCES

1. Sather, A., "Investigation into the Depth of Pulsed Eddy-Current Penetration," Eddy-Current Characterization of Materials and Structures, 374-386, G. Birnbaum and G. Free, Eds., ASTM STP 722.
2. Waidelich, D. L., "Reduction of Probe Spacing Effect in Pulsed Eddy Current Testing," Symposium on Nondestructive Tests in the Field of Nuclear Energy, ASTM, 1958.
3. Libby, H. L., Introduction to Electromagnetic Nondestructive Test Methods, Krieger, New York, 1979.
4. Wittig, G., and Thomas, H. M., "Design of a Pulsed Eddy Current Test Equipment with Digital Signal Analysis," Eddy-Current Characterization of Materials and Structures, G. Birnbaum and G. Free, Eds., ASTM STP 722, 387-397, 1981.
5. Busse, T. H., and Beyer, N. S., "Pulsed Eddy Current Inspection of Thin-Walled Reactor Tubing," Materials Evaluation, 28, 228, October 1970.
6. Auld, B. A., "Theoretical Characterization and Comparison of Resonant-Probe Microwave Eddy-Current Testing with Conventional Low-Frequency Eddy-Current Methods," in: Eddy-Current Characterization of Materials and Structures, G. Birnbaum and G. Free, Eds., ASTM STP 722, 1981.
7. Kahn, A. H., Spal, R., and Feldman, A., "Eddy Current Losses Due to a Surface Crack in Conducting Material," Journal of Applied Physics, 48, 4454, 1977.
8. Beissner, R. E., Sablik, M. J., Krzywosz, K. J., and Doherty, J. E., "Optimization of Pulsed Eddy Current Probes," Review of Progress in Quantitative NDE, Vol. 2, D. O. Thompson and D. E. Chimenti, Eds., Plenum, New York, 1983.
9. Burrows, M., "A Theory of Eddy Current Flaw Detection," Ph.D. Thesis, University of Michigan, 1964, University Microfilms International, Ann Arbor, Michigan.
10. Dodd, C. V., and Deeds, W. E., "Analytical Solutions to Eddy-Current Probe-Coil Problems," Journal of Applied Physics, 39:2829, 1968.
11. Waidelich, D. L., "Pulsed Eddy Currents," in Research Techniques in Nondestructive Testing, 383-416, R. S. Sharpe, Ed., Academic Press, 1970.

12. Morris, R. A., "Quantitative Pulsed Eddy Current Analysis," Proc. 10th Symposium on NDE, San Antonio, April 23-25, 1975.
13. Hendrickson, I. G., and Hansen, K. A., "High Peak Energy Shaped Pulse Electromagnetic Crack Detection," Eddy Current Characterization of Materials and Structures, 129-139, G. Birnbaum and G. Free, Eds., ASTM, 1981.

APPENDIX A  
ANALYTICAL MODELS

Development of the Simplified Model

The purpose of developing the simplified analytical model was to obtain approximate mathematical solutions that describe the effect of the shield on the transient field produced by an arbitrary excitation pulse. Of primary interest is the focusing effect, i.e., the narrowing of the spatial distribution of field and the shielding of the detector from the excitation pulse. To achieve the stated purpose, the field reflected by the specimen was ignored, and the model employed was a cylindrical excitation coil of finite length surrounded by a cylindrical shield of the same length. The probe configuration of the excitation coil used is as shown in Figure 39.

An approximate analytical solution was obtained by first solving for the transient current induced in a shield of infinite length, and then substituting this current in the integral expression for the vector potential for a shield and coil of finite length. The solution thus obtained was

$$\frac{dB_z}{dt} \sim \mu_0 \frac{dJ_0(t)}{dt} \frac{\rho_1}{\rho_2} \left[ \rho_2 G(\vec{x}, \rho_1) - \rho_1 G(\vec{x}, \rho_2) \right]$$

where  $B_z$  is the vertical component of the flux density (in the sense of Figure 39),  $J_0$  is the excitation current,  $\rho_1$  is the coil radius,  $\rho_2$  is the inner radius of the shield, and  $G$  is a rather complicated geometrical factor involving elliptic integrals. (8) This expression applies to thin shields such that  $T \ll |x|$ , where  $T$  is the shield thickness. It also applies only to shielding of the excitation pulse; the effect of the field that diffuses through the shield has been ignored. Use of this result is, therefore, limited to studies of the spatial distribution of the primary field.

To estimate the time-dependent field that diffuses through the shield to the detector position, the solution for an infinitely long shield was employed with the additional assumption that the effect of shield curvature could be ignored. This led to an exponentially convergent series solution for the field at the outside surface of the shield.

These approximate analytical solutions were used to study the effects of probe geometry on the focusing of the primary field and the time-dependence of the field at the outside surface of the shield. A typical result illustrating the focusing effect is shown in Figure 40. This is a plot of the geometrical factor  $\rho_2 G(x, \rho_1) - \rho_1 G(x, \rho_2)$  as a function of distance from the center of the coil along a line 0.025 mm from the end of the probe. The sharp negative peak at about 1.8 mm occurs in the region between the coil and shield.

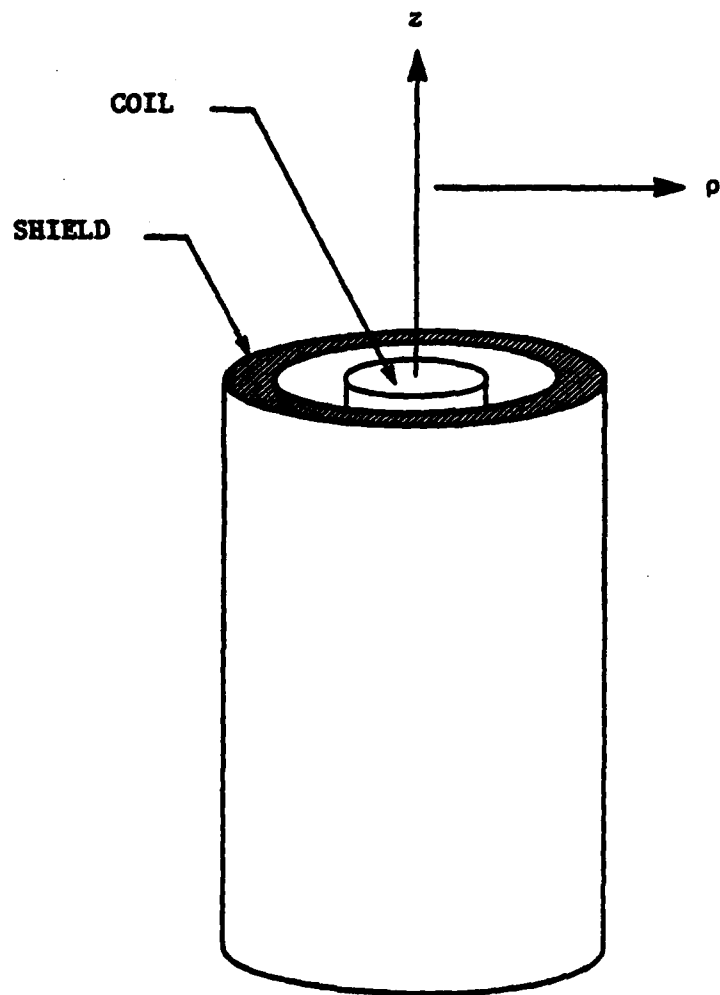


Figure 39. Simplified Model of Pulsed Eddy Current Probe. This model was used to evaluate the field in front of and alongside the probe. The finite current coil is modeled as a thin current sheet at  $\rho_1$ .

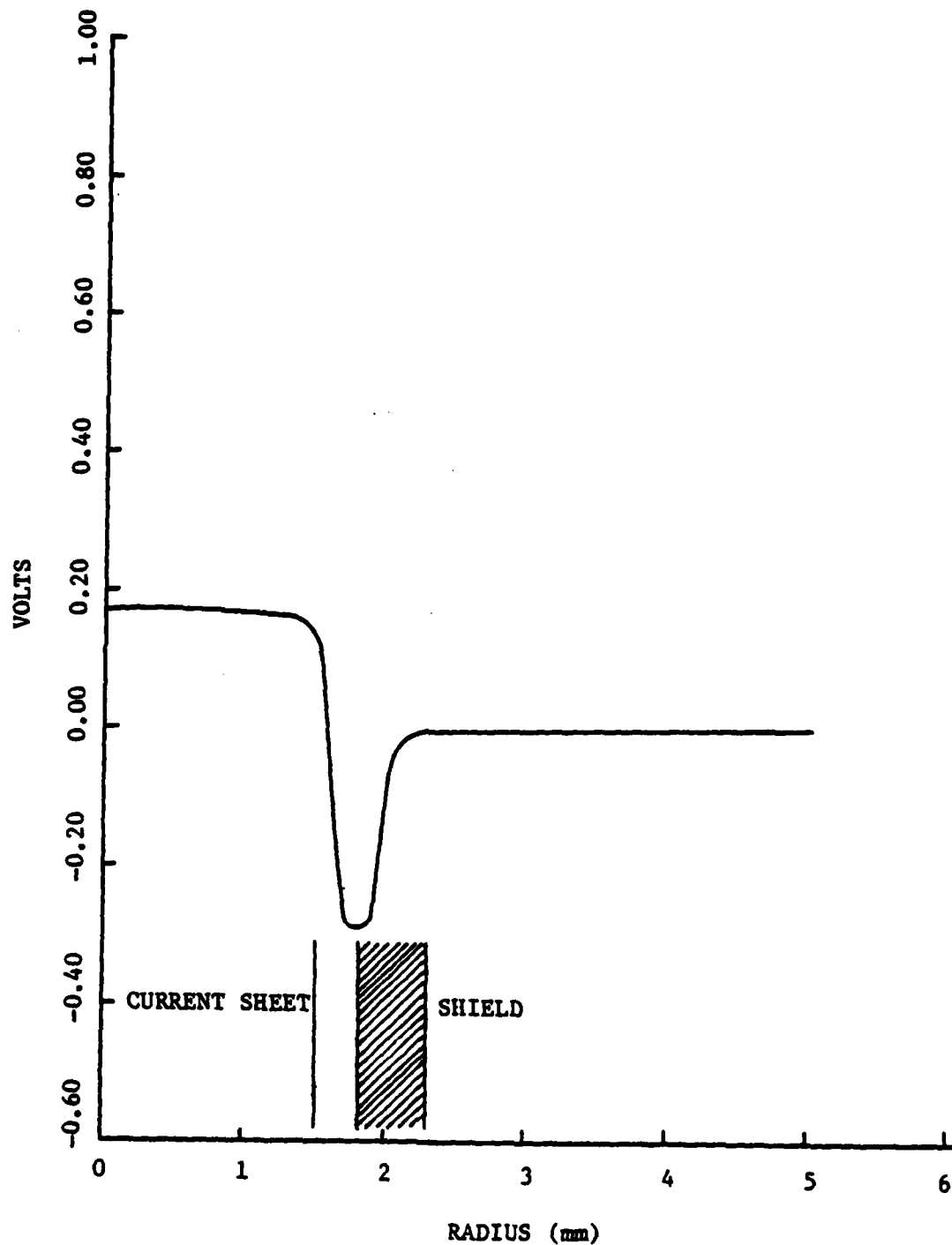


Figure 40. Field Calculated 0.025 mm in Front of the Model Probe Shown in Figure 39. The field change is greatest between the current sheet and the shield. The length of the model probe is 9.5 mm.

The time-dependent field just inside and outside a shield of 0.25-mm thickness is shown in Figure 41. For a shield this thin, the calculation shows that the diffusion component of the field just outside a shield peaks about 1  $\mu$ sec after the initial pulse. Other calculations indicate that increasing the shield thickness to 1.5 mm causes the diffusion time to increase to about 9  $\mu$ sec and reduces the amplitude of the diffusion pulse by about a factor of 200.

These results indicate that copper shielding provides both focusing of the excitation field and shielding of receiver coils from coupling directly with the excitation field.

#### Development of Detailed Model

The detailed model is a small flaw theory in the sense that the current perturbation caused by the flaw is approximated by a current dipole in exactly the same way as in the theory of Burrows (9) and Dodd et al. (10).

The major difference between this new small flaw model and the Burrows' theory is that we start with the Fourier or Laplace transform of the general time-dependent form of Maxwell's equations rather than the special case of a sinusoidal driving current.

Application of the reciprocity theorem and the introduction of the small flaw scattering matrix  $\vec{\alpha}$  then follow as in Burrows' dissertation, leading to the flaw impulse response function given by

$$\Delta v(t) = -\frac{3}{2} \sigma v_f \int_0^t \left( \frac{\vec{E}_t}{I_t} \right)_t \cdot \vec{\alpha} \cdot \left( \frac{\vec{E}_r}{I_r} \right)_{t-t'} dt' \quad (A-1)$$

where  $\sigma$  is the conductivity,  $v_f$  is the flaw volume,  $\vec{\alpha}$  is the flaw scattering matrix, and the  $\vec{E}/I$  functions are electric fields at the flaw position caused by current pulses of infinitesimal duration in the transmitter (t) and receiver (r). For an excitation current  $I(t)$  in the transmitter, the voltage pulse in the receiver is given by the convolution of  $I(t)$  with  $\Delta v(t)$ , i.e.,

$$\Delta v(t) = \int_0^t I(t') \Delta v(t-t') dt' \quad (A-2)$$

The first step in a prediction of flaw response is the calculation of the vector potentials  $A_0$  and radial flux densities  $\partial A_0 / \partial z$  in air for an axisymmetric transmitter and an axisymmetric differential receiver. Input variables for these calculations are coil length, radius of the permeable core,

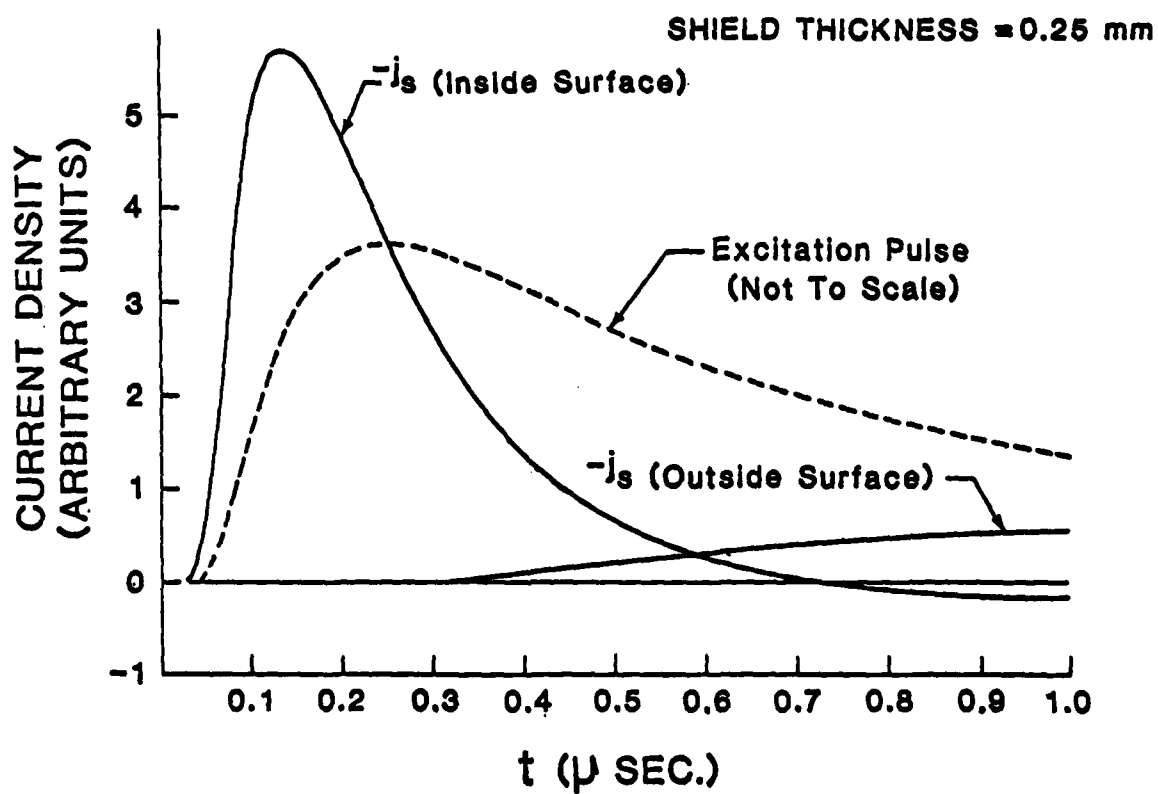


Figure 41. Time-Dependent Field Alongside a Probe With a 0.25-mm Thick Shield. It takes approximately one microsecond after the initial pulse for the field peak to diffuse through the shield. The current sheet is 1.6 mm, and the shield is 1.7 mm from the probe centerline.

winding thickness and shield radius. For a differential coil, the winding consists of any number of alternating layers of positive and negative current. The theory used for these calculations was the same as that used in the simplified model.

Once the fields in air are known, the next step is the calculation of E/I functions for the transmitter and receiver. This may be done by direct numerical integration of the following exact expression:

$$\begin{aligned} \frac{E}{I} = & - \frac{e^{-z^2/4\tau}}{2(\mu\sigma)2\sqrt{\pi\tau^3}} \int_0^\infty \left[ \frac{\partial A_0}{\partial z} \left( \frac{z^2}{2\tau} - 1 \right) \tilde{I}_1 \right. \\ & + \left. \left( A_0 \left( \frac{z^2}{2\tau} - 1 \right) - \frac{\partial A_0}{\partial z} |z| \right) \tilde{I}_2 \right. \\ & \left. - |z| A_0 \tilde{I}_3 \right] \rho' d\rho' \end{aligned} \quad (A-3)$$

where  $A_0$  and its derivative are evaluated at  $\rho'$  and the  $F_n$  are integrals of ordinary Bessel functions. Two of these integrals,  $F_1$  and  $F_3$ , can be evaluated analytically, but the third requires numerical integration. The exact calculation of E/I therefore requires rather extensive numerical computation.

In numerical studies of the various quantities involved in this integral, it was discovered that the  $F_n$  functions are strongly peaked at  $\rho' = \rho$ . This finding then led to the following approximate result in which  $A_0$  and  $\partial A_0/\partial z$  are evaluated at  $\rho$ :

$$\begin{aligned} \frac{E}{I} \sim & - \frac{e^{-z^2/4\tau}}{2\sqrt{\pi}(\mu\sigma)2\tau^{3/2}} \left[ \frac{\partial A_0}{\partial z} \cdot \left( \frac{z^2}{2\tau} - 1 \right) \cdot (1 - e^{-\rho^2/4\tau}) \right. \\ & + \rho^2 \left\{ A_0 \cdot \left( \frac{z^2}{2\tau} - 1 \right) - \frac{\partial A_0}{\partial z} \cdot |z| \right\} \frac{\sqrt{\pi e^{-\rho^2/4\tau}}}{8\tau^{3/2}} \cdot \frac{1}{8\tau} \left\{ I_0 \left( \frac{\rho^2}{8\tau} \right) - I_1 \left( \frac{\rho^2}{8\tau} \right) \right\} \\ & \left. - |z| \rho^2 A_0 \frac{e^{-\rho^2/4\tau}}{4\tau} \right] \end{aligned} \quad (A-4)$$

where  $I_0$  and  $I_1$  are modified Bessel functions. Numerical tests, one of which is shown in Figure 42, show that the approximate formula gives results that are within about 20 percent of the results obtained by numerical integration except for small  $\rho$  where  $E/I$  itself is small. Because use of the approximate formula reduces computer time by about a factor of 1000, all parametric flaw response studies were based on the approximate calculation of  $E/I$ .

The next step is the calculation of  $\Delta v(t)$  according to equation (A-1). The time integral is evaluated numerically and the results are retained as a disc file. The final step is then given by equation (A-2), which, again, is evaluated numerically.

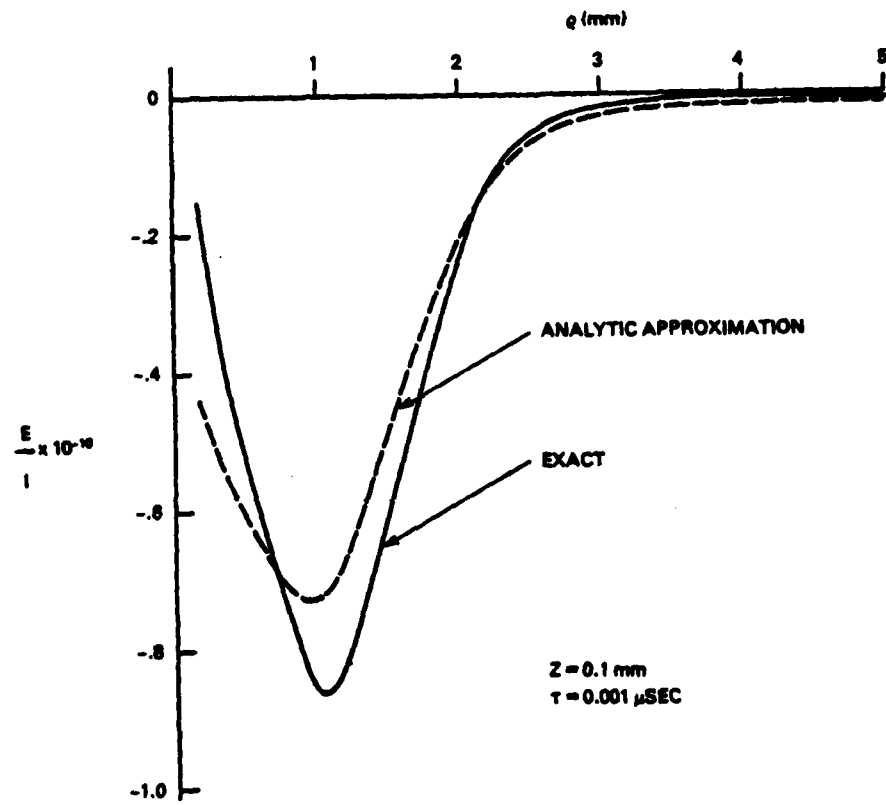


Figure 42. Comparison of the Analytic Approximation to the Exact Expression of Current Density

## APPENDIX B

AN ALTERNATIVE APPROACH FOR COMPUTING EDDY CURRENTS:  
CASE OF THE DOUBLE-LAYERED PLATEAn Alternative Numerical Approach for Computing  
Eddy Currents: Case of the Double-Layered Plate

MARTIN J. SABLİK, MEMBER, IEEE, ROBERT E. BEISSNER, AND ATHENE CHOY

*Abstract*—A numerical approach is presented for cases where induced eddy current densities are to be computed in axisymmetric situations. Conductors are represented as stacks of inductively coupled, concentric, metal rings in which current is excited by an external coil. Matrix techniques are used to solve the resulting set of circuit equations. Sinusoidally induced currents in a sandwich plate consisting of two layers of different metals are discussed as an application. Comparison is made with a finite element calculation and with results obtained via an analytical approach. Non sinusoidal excitation is also briefly discussed.

Manuscript received September 27, 1983; revised December 27, 1983. This paper was supported in part by the Air Force Wright Aeronautical Laboratories under Contract F33615-81-C-5036 and the Naval Sea Systems Command in cooperation with the Quantitative NDE Program of Ames Laboratory.

M. J. Sablik and R. E. Beissner are with Southwest Research Institute, P.O. Drawer 28510, San Antonio, TX 78284.

A. Choy was with Southwest Research Institute. She is now with NL Industries, Inc., P.O. Box 60075, Houston, TX 77305.

## I. INTRODUCTION

**I**N THIS PAPER we discuss a numerical approach to axisymmetric problems involving the computation of eddy current distributions induced in conductors by a driving current in a cylindrical coil. Each conductor is represented by stacks of inductively coupled metal rings concentric with the driving coil. Matrix techniques are employed in solving the set of circuit equations used to represent the interaction between rings in the conductors and the external driving current. This "coupled circuit approach" is a generalization of earlier work by Chang and Smith [1], [2].

The paper is organized as follows. Section II discusses the coupled circuit approach. Section III presents numerical results for the case of eddy currents induced in a sandwich plate consisting of two layers of different metals and compares these

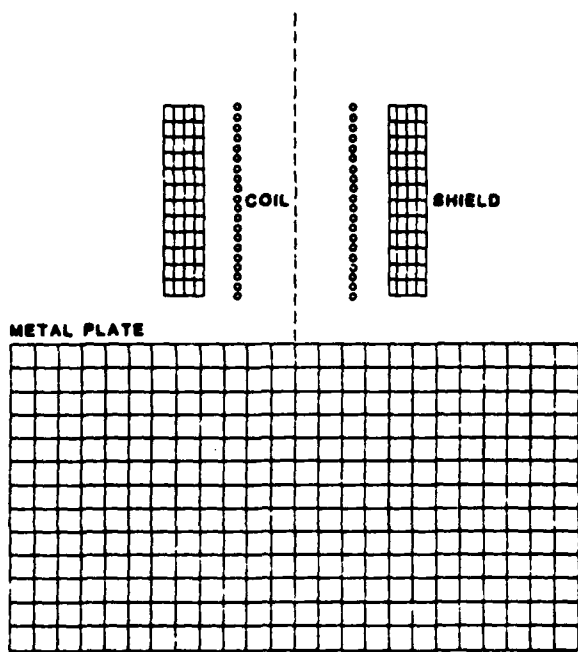


Fig. 1. Example of axisymmetric configuration which can be treated by coupled circuit approach. Metal plate and shield are subdivided into concentric stacks of rings, as shown in this two-dimensional cross section.

results to those obtained by Palanisamy *et al.* [3], [4] via the finite element method [5], [6]. Section IV compares the analytic solution of Dodd *et al.* [7]-[9] to the coupled circuit results for the sandwich plate. Section V briefly discusses extension of the coupled circuit approach to nonsinusoidal driving currents.

## II. THE COUPLED CIRCUIT APPROACH

When current flows in a circular coil, the vector potential produced by it has only one component  $A_\theta$  in cylindrical coordinates. Thus currents induced in a conductor tend to flow in circular paths concentric with the axis of the excitation coil. The same situation prevails when the excitation coil is a multi-turn tightly wound cylindrical coil. Thus, when conductors are positioned axisymmetrically with respect to the excitation coil, the conductors can be modeled as stacks of inductively coupled, concentric, conducting rings.

Fig. 1 shows a typical problem. A coil is surrounded by a conducting shield and positioned over a conducting plate. The plate is modeled as a disk broken horizontally and vertically into stacks of concentric conducting rings. In Chang and Smith's model [1] of a conducting plate, a tiny cylindrical hole was inserted in the center of the plate. This hole is not necessary because the vector potential goes to zero along the central axis [10] and hence so does  $E = -\partial A/\partial t$  and  $J = \sigma E$ . Our computer calculations produce essentially equivalent results with and without the hole.

The problem depicted in Fig. 1 is of greater complexity than that treated by Chang and Smith [1], [2] in that 1) a multi-turn excitation coil is considered, 2) a vertical distribution of eddy currents in the plate is obtainable, and 3) the effect of a conducting shield about the driving coil can be considered.

Eddy current distributions in both the plate and the shield are obtainable. In another type of general axisymmetric problem, the shield can be replaced by a secondary coil and currents in the secondary can be obtained. The plate can also be divided into layers of different conducting media.

Each of the rings is replaced by its corresponding circuit representation. The  $i$ th ring is assigned a self-inductance  $L_i$  and a resistance  $R_i$ . Mutual inductance  $M_{i0}$  exists between the  $i$ th ring and the excitation coil. In addition the  $i$ th ring is coupled to all other rings via mutual inductances  $M_{ij} = M_{ji}$ , where  $i = 1, 2, \dots, N$  and  $i \neq j$  and where there are  $N$  rings in total.

The currents in the rings are then completely determined [1] by the following sets of equations in phasor form for sinusoidal angular frequency  $\omega$ :

$$\begin{aligned} (R_1 I_1 + j\omega L_1 I_1) + j\omega M_{12} I_2 + \dots + j\omega M_{1N} I_N \\ = -j\omega M_{10} I_0 \\ j\omega M_{21} I_1 + (R_2 I_2 + j\omega L_2 I_2) + \dots + j\omega M_{2N} I_N \\ = -j\omega M_{20} I_0 \\ \dots \\ j\omega M_{N1} I_1 + j\omega M_{N2} I_2 + \dots + (R_N I_N + j\omega L_N I_N) \\ = -j\omega M_{N0} I_0, \end{aligned} \quad (1)$$

where  $I_0$  is the current in the excitation coil. After dividing both sides of these equations by  $j\omega$ , the equations may be written in matrix form as

$$[X][I] = -[V], \quad (2)$$

where

$$[X] = \begin{bmatrix} L_1 - jR_1/\omega & M_{12} & \dots & M_{1N} \\ M_{21} & L_2 - jR_2/\omega & \dots & M_{2N} \\ \vdots & \vdots & \ddots & \vdots \\ M_{N1} & M_{N2} & \dots & L_N - jR_N/\omega \end{bmatrix} \quad (3)$$

and  $[I]$  is the column matrix  $[I_1, I_2, \dots, I_N]$  and  $[V]$  the column matrix  $[M_{10} I_0, M_{20} I_0, \dots, M_{N0} I_0]$ . Equation (2) can then be solved as

$$[I] = -[X]^{-1} [V]. \quad (4)$$

To calculate the mutual inductance between two circular filament conductors with the same axis, the following result is used [11], [12]:

$$M_{12} = \mu_0 \sqrt{r_1 r_2} \left[ \left( \frac{2}{k} - k \right) K(k) - \frac{2}{k} E(k) \right], \quad (5)$$

where  $r_1$  and  $r_2$  are the radii of the circular filaments,  $K(k)$  and  $E(k)$  are complete elliptic integrals of the first and second kind, and

$$k^2 = 1 - \frac{p^2}{q^2}, \quad (6)$$

where

$$p^2 = (r_2 - r_1)^2 + s^2, \quad (7a)$$

$$q^2 = (r_2 + r_1)^2 + s^2, \quad (7b)$$

and  $s$  is the distance between the planes of the filaments.

Following Rosa and Grover [12], Chang [1] used series expressions in place of (5). These are unsuitable because they cannot be applied to all geometries. Modern "math packs" available on large main-frame computers can evaluate elliptic integrals readily in all situations. Thus (5) was employed to compute the mutual inductances.

To calculate the mutual inductance between two rings  $i$  and  $j$  in our model, both of the rings are subdivided into  $n$  smaller rings. Each smaller ring is then replaced by a filament in its center. Following Chang [1], the mutual inductance is then given by

$$M_{ij} = \frac{1}{n^2} \sum_{l_i=1}^n \sum_{m_j=1}^n M_{l_i m_j}, \quad (8)$$

where  $M_{l_i m_j}$  is the mutual inductance as given by (5) of two filaments  $l_i$  and  $m_j$  inside rings  $i$  and  $j$ , respectively.

To compute the self-inductance of a conducting ring  $i$  in our model, the ring is subdivided into  $n$  smaller rings, and these smaller subrings are again replaced by filaments. The self-inductance of the conducting ring is then given by

$$L_i = \frac{1}{n^2} \sum_{l_i=1}^n \sum_{\substack{m_i=1 \\ l_i \neq m_i}}^n M_{l_i m_i} + \frac{1}{n} \sum_{l_i=1}^n L_{l_i}^{(0)}, \quad (9)$$

where  $L_{l_i}^{(0)}$  is the self-inductance of filament  $l_i$ , given by Smythe [13] as

$$L_{l_i}^{(0)} \approx \mu_0 a_i [\ln(16a_i/c_i) - 1.75] \quad (10)$$

for  $a_i \gg c_i$ , where  $a_i$  is the radius of the filament and  $c_i$  is the width of the subring replaced by the filament.<sup>1</sup>

The mutual inductance  $M_{i0}$  between a conducting ring and the excitation coil is calculated in the same way as other mutual inductances. The ring is divided into  $n$  subrings, the subrings are replaced by filaments, and the excitation coil of  $n_0$  turns is replaced by a vertical stack of  $n_0$  concentric circular filaments, equally spaced. A multilayered excitation coil is modeled as several concentric vertical stacks of filaments, appropriately spaced.  $M_{i0}$  is given by

$$M_{i0} = \frac{1}{n} \sum_{l_i=1}^n \sum_{m_i=1}^{n_0} M_{l_i m_i}. \quad (11)$$

The resistance of the rings is calculated by

$$R_i = \rho_i L_i / A_i \quad (12)$$

where  $R_i$  is the resistance of the  $i$ th ring,  $\rho$  is its resistivity,  $L_i = 2\pi r_i$  is the mean path length of current in the ring,  $r_i$  is the mean radius of the ring, and  $A_i$  is the cross-sectional area of the ring.

Current densities in each ring are easily derivable from matrix  $[J]$  in (4) and from ring dimensions.

<sup>1</sup>Although this condition is not satisfied for the innermost filament of the innermost ring, it does not lead to significant error in the numerical calculation because, as cited in the text, the current will be negligible in the region where the approximation breaks down.

### III. COMPARISON TO FINITE ELEMENT RESULTS FOR THE CASE OF THE DOUBLE-LAYERED PLATE

Although we have constructed a computer program to handle a problem as general as that depicted in Fig. 1, we here restrict the geometry to a single-layer 20-turn excitation coil above a conducting plate of two layers. In the first layer of the plate, the resistivity  $\rho$  is  $6.6934 \times 10^{-7}$  ohm-meters (appropriate to stainless steel); in the second layer,  $\rho = 1.5221 \times 10^{-6}$  (appropriate to certain titanium alloys). The first layer is 0.127 cm (50 mils) thick; the second of unlimited thickness. The coil has a length of 0.3175 cm (125 mils) and diameter of 0.3175 cm. The coil carries 0.5 A of sinusoidally varying current.

Presented here are the results of two numerical solutions to the problem—one by the coupled circuit approach and one by the finite element approach.

In the coupled circuit approach, the first layer of the plate is subdivided into four sublayers, each 0.03175 cm thick, and the second layer is subdivided into nine sublayers of similar thickness. The fact that the second layer is given a finite thickness has a negligible effect on the results because of the skin effect and because the plate is modeled as a disk of sufficiently large diameter, namely, 2.655 cm. Each layer of the plate is subdivided into 12 concentric subrings of equal radial thickness. In this way, both a horizontal and vertical distribution of the eddy currents in the plate can be obtained.

Fig. 2 shows details concerning the way in which Palanisamy [3] did the corresponding finite element calculation. The coil is modeled as a region of uniform current density  $4.133 \times 10^3$  A/cm<sup>2</sup>, of inner radius 0.1588 cm and outer radius 0.1664 cm. Finite elements inside the conducting plate are not uniform in size but are smaller in the regions of high eddy current density and larger in regions of low eddy current density, gradually increasing in size from high to low density regions, as seen in the discretization depicted in Fig. 2. By contrast, for a single sinusoidal excitation frequency, the coupled circuit approach does not require a similar refinement utilizing graduated ring size at least for frequencies in the range from 5 to 2000 kHz.

Fig. 3 depicts the variation of the eddy current density magnitude with depth at a particular radius from the central axis, namely, 0.1664 cm. A characteristic discontinuity in current density versus depth is seen at the boundary between the two plate layers. Both finite element results (solid curves) and coupled circuit results (dashed curves) are presented. Agreement in the frequency range 12.5–200 kHz is extremely good despite the small differences in the way in which the excitation coil is modeled.

The coupled circuit computation was performed on a CDC CYBER 172 computer which is a 64-bit machine, whereas the finite element computation was performed on a VAX 11/780, which is a 32-bit machine. The coupled circuit computation involved initial construction of a  $156 \times 156$  mutual inductance matrix (requiring about 7.5 min of CPU time). Once formulated, this inductance matrix however did not have to be recomputed for each new frequency. The finite element tech-

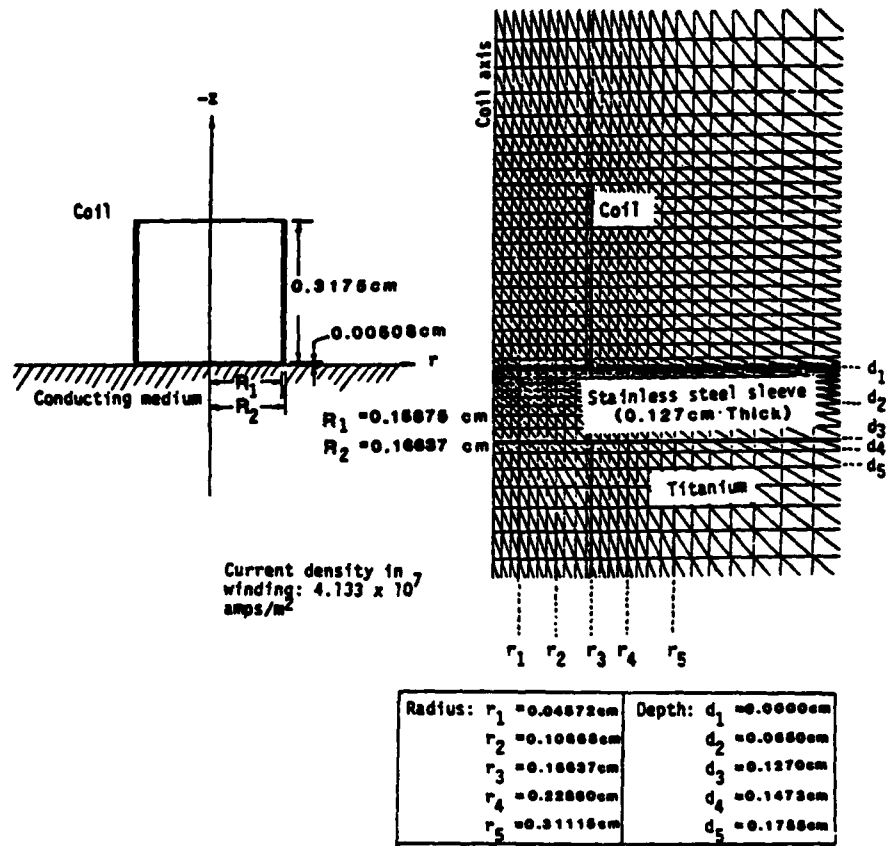


Fig. 2. Air-core coil over a conducting slab and the finite element discretization (courtesy of R. Palanisamy).

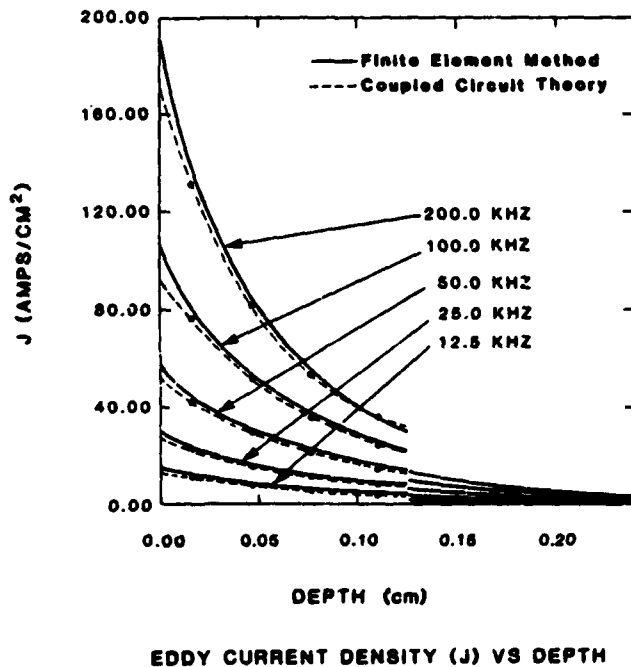


Fig. 3. Current density in plate as function of depth for frequencies from 12.5 kHz to 200 kHz. The discontinuity seen at depth of 0.127 cm (50 mils) is due to change in medium. Top plate layer is stainless steel and bottom layer is titanium alloy.

nique required the storage of 60 000 element matrix. Both techniques required roughly one minute per frequency to compute respective spatial distributions of eddy currents. In terms of computation times, the two techniques are roughly comparable, with finite element possibly being slightly faster in initial construction of matrices, but with finite element also requiring slightly more storage. This latter however may not necessarily be true as perhaps a coarser mesh could have given somewhat similar results.

IV. COMPARISON TO ANALYTICAL RESULTS FOR THE CASE OF THE DOUBLE-LAYERED PLATE

Dodd *et al.* [7]-[9] have found an analytical solution for the problem of a sinusoidally varying current in an excitation coil above a double-layered plate, where the second layer is of infinite vertical extent and both layers are of infinite horizontal extent.

Two models can be used for the excitation coil. First the coil can be represented as a stack of equally spaced circular filaments ("delta-function coils"). Second, it can be represented as a cylindrical sheet with length and radius corresponding to that of the excitation coil and with current per unit length equal to  $n_0 I_0 / (l_{n_0} - l_1)$ , where  $l_1$  and  $l_{n_0}$  are distances from the plate to the bottom and top of the excitation coil, respectively, and where the coil has  $n_0$  turns.

In the case of the first model, the current densities  $J_1^{(I)}$  and  $J_2^{(I)}$  in plate layers 1 and 2, respectively, are given in phasor notation by [7]-[9]

$$J_1^{(I)}(r, z) = -j\omega\sigma_1\mu_0 I_0 r_0 \int_0^\infty J_1(\alpha r_0) J_1(\alpha r) \frac{1 - e^{-n_0\alpha_0\Delta l}}{1 - e^{-\alpha_0\Delta l}} e^{-\alpha_0 l_1} \times \alpha \left\{ \frac{(\beta_1 + \beta_2) e^{2\alpha_1 D} e^{\alpha_1 z} + (\beta_1 - \beta_2) e^{-\alpha_1 z}}{(\alpha_0 - \beta_1)(\beta_1 - \beta_2) + (\alpha_0 + \beta_1)(\beta_1 + \beta_2) e^{2\alpha_1 D}} \right\} d\alpha, \quad (13a)$$

$$J_2^{(I)}(r, z) = -j\omega\sigma_2\mu_0 I_0 r_0 \int_0^\infty J_1(\alpha r_0) J_1(\alpha r) \frac{1 - e^{-n_0\alpha_0\Delta l}}{1 - e^{-\alpha_0\Delta l}} e^{-\alpha_0 l_1} \times \alpha \left\{ \frac{2\beta_1 e^{(\alpha_1 + \alpha_2)D} e^{\alpha_2 z}}{(\alpha_0 - \beta_1)(\beta_1 - \beta_2) + (\alpha_0 + \beta_1)(\beta_1 + \beta_2) e^{2\alpha_1 D}} \right\} d\alpha, \quad (13b)$$

where  $\sigma_1$  and  $\sigma_2$  are the respective conductivities of the two plate layers,  $r_0$  is the radius of the excitation coil,  $J_1(\alpha r_0)$  is a Bessel function of order one,  $\Delta l = (l_{n_0} - l_1)/n_0$ ,  $D$  is the thickness of the first plate layer, and

$$\alpha_j = \sqrt{\alpha^2 - \omega^2\mu_j\epsilon_j + j\omega\mu_j\sigma_j}, \quad (14a)$$

$$\beta_j = (\mu_0/\mu_j)\alpha_j, \quad (14b)$$

with  $j = 0, 1, 2$  and  $\sigma_0 = 0$ . The numerical results presented earlier have been calculated under the assumption that  $\mu_0 = \mu_1 = \mu_2$  and  $\epsilon_0 = \epsilon_1 = \epsilon_2$ , so that  $\beta_j = \alpha_j$ . For the case of the second model, the expression

$$\frac{1 - e^{-n_0\alpha_0\Delta l}}{1 - e^{-\alpha_0\Delta l}} e^{-\alpha_0 l_1} = \sum_{i=1}^{n_0} e^{-\alpha_0 l_i} \quad (15)$$

is replaced by

$$\frac{1}{\Delta l} \int_{l_1}^{l_{n_0}} e^{-\alpha_0 l} dl = \frac{1}{\Delta l} \left\{ \frac{1}{\alpha_0} (e^{-\alpha_0 l_1} - e^{-\alpha_0 l_{n_0}}) \right\}. \quad (16)$$

The first analytical model shall be called the "g-model," since a geometric series is used in the evaluation. The second analytical model shall be called the "l-model," since an integral over the length of the coil is used. Two models are introduced because in the coupled circuit analysis, the coil was modeled as a stack of circular filaments discretely spaced (which corresponds to the g-model), whereas in the finite element case, the coil was treated as a narrow cylinder of constant current density (which corresponds roughly to the l-model).

Fig. 4 presents the results of both the g-model and the l-model for the geometry described in Section III. The coupled circuit results are superimposed on the analytic curves. It is seen that agreement is extremely good. The slight differences between g-model results and l-model results are about the same as the differences between the coupled circuit results and the finite element results noted earlier, suggesting that the way in which the coil is modeled chiefly accounts for differences between results from the two numerical approaches.

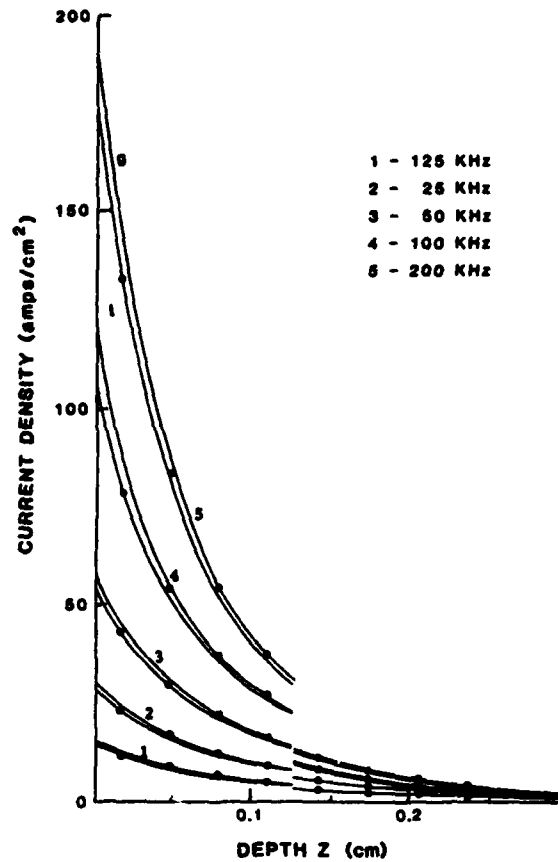


Fig. 4. Current density in two-layered plate as function of depth. Solid curves represent analytical results, with label  $g$  denoting "g-model" and label  $l$  denoting "l-model," as explained in text. Solid circles show the results from coupled circuit computation.

Figs. 5 and 6 focus on a particularly interesting effect, namely, that the current density at the boundary between the two plate layers exhibits a broad maximum in its frequency dependence for the range 300-500 kHz. The coupled circuit approach and the analytic approach both exhibit this same effect, whereas the finite element calculation was not tried for this frequency range.

Fig. 7 shows a comparison between analytic and coupled circuit approaches for a frequency range in order of magnitude greater than that seen in Fig. 3. As can be seen, the coupled circuit approach gives fairly good predictions without an adjustment in ring subdivisions.

## V. GENERALIZATION TO NONSINUSOIDAL EXCITATION

The coupled circuit approach can be extended to nonsinusoidal excitation, but at the expense of considerable computation time. The first step is to obtain a fast Fourier transform of the excitation signal  $I_0(t)$ . Thus, for example, values  $I_0(\omega_k)$  are obtained for the discrete set of frequencies  $\{\omega_k\}$ . The response  $I_i(\omega_k)$  of the  $i$ th conducting ring to sinusoidal excitation current  $I_0 e^{j\omega_k t}$  is then obtained using coupled circuit solution (4). A fast Fourier transform is then taken of the product set  $\{I_n(\omega_k) I_i(\omega_k)\}$  to obtain the time-developing current  $I_i(t)$  in ring  $i$ . A similar numerical transform procedure for pulsed excitations has been reported recently by Allen [14].

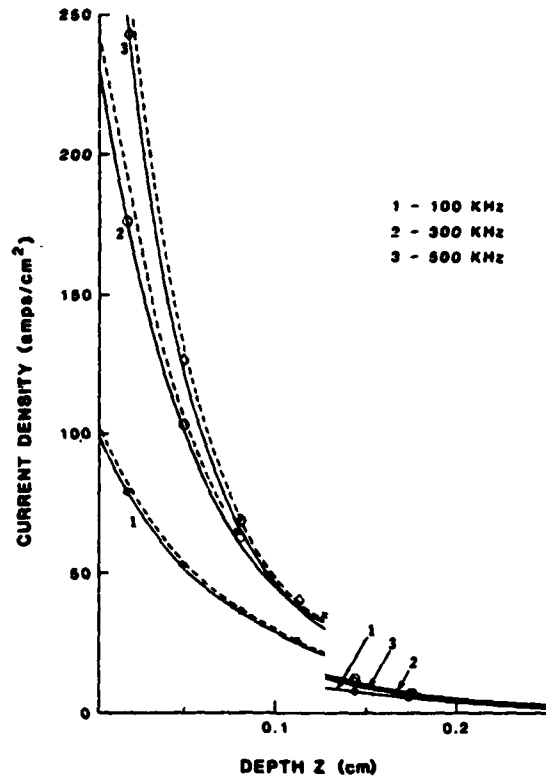


Fig. 5. Current density versus depth for higher frequencies in range from 100-500 kHz. Solid curves denote *l*-model analytical results; dashed curves, *g*-model analytical results. Coupled circuit results are denoted by  $\bullet$ , 100 kHz;  $\circ$ , 300 kHz; and  $\circ$ , 500 kHz. Crosses denote 300 kHz *g*-model results at depths where 300 kHz and 500 kHz curves intersect.

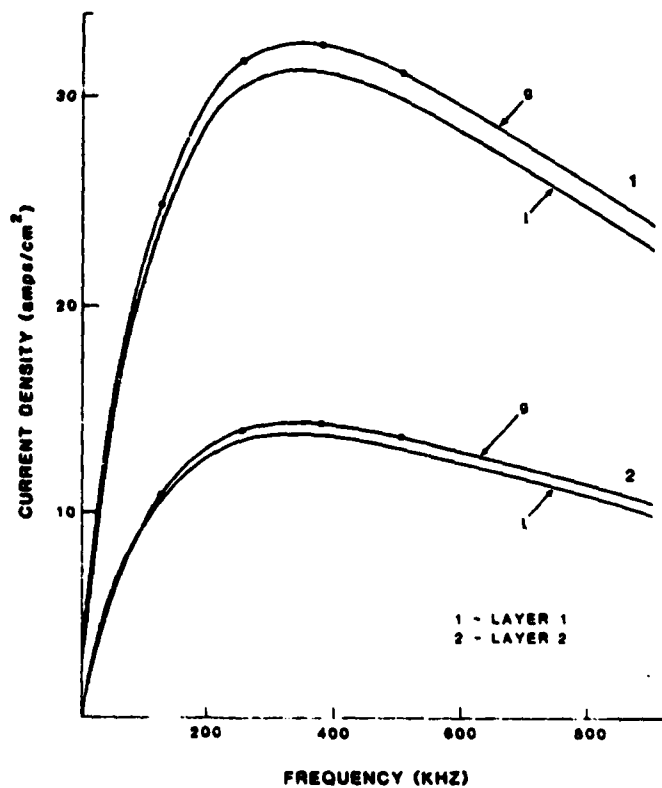


Fig. 6. Current density versus frequency at depth of 0.127 cm, corresponding to boundary between layer 1 (stainless steel) and layer 2 (titanium alloy). Analytical results are given by solid curves. Top two curves represent currents on stainless steel side of the boundary; bottom curves, the titanium side.

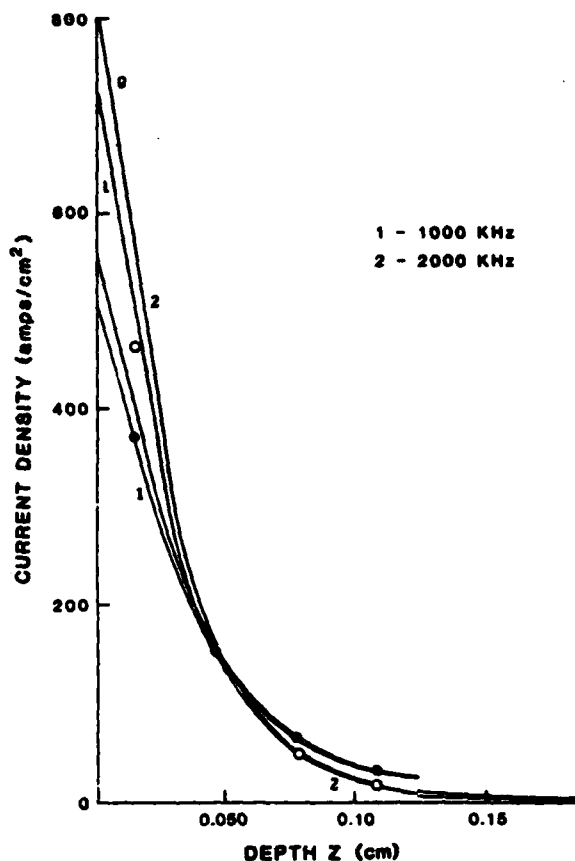


Fig. 7. Current density versus depth for frequencies 1000 kHz (●) and 2000 kHz (○). As before, solid curves represent analytical results (labeled *g* and *l*), and points represent coupled circuit results.

We have tried this approach on the problem of an excitation coil surrounded by a conduction shield. This problem has relevance to probe design in the pulsed eddy current nondestructive evaluation technique [15]. An analytical solution is now available for this situation [15].

For this case, uniform discretization into conducting rings does not produce results that completely represent the correct time development of the current response. Much better results are obtainable if rings are narrow and thin in regions of high current density and broad and thick in regions of low current density. Thus for nonsinusoidal excitation, nonuniform discretization is necessary.

## VI. CONCLUSION

An alternative numerical approach to the problem of computing induced eddy current densities in axisymmetric geometries has been discussed. This "coupled circuit approach" reproduces analytical solutions extremely well in the case of single-frequency excitation using a relatively simple discretization procedure. Computation times and storage requirements are comparable to the finite element approach. The coupled circuit approach can also be used for nonsinusoidal excitation using a fast Fourier transform procedure.

## ACKNOWLEDGMENT

We thank Dr. R. Palanisamy of Ames Laboratory at Iowa State University, who made his finite element results available to us.

## REFERENCES

- [1] K. Q. Chang, thesis, U. of Missouri-Rolla, 1971 (unpublished).
- [2] R. T. Smith, *IEEE Trans. on Aerospace and Electronic Systems*, vol. AES-11, pp. 495-498, July 1975.
- [3] R. Palanisamy, private communication.
- [4] R. Palanisamy, D. O. Thompson, G. L. Burkhardt, and R. E. Beissner, "Eddy current detection of subsurface cracks in engine disk bolt holes," presented at DARPA/AFWAL Conf. on Quantitative NDE, Santa Cruz, CA, Aug. 7-12, 1983.
- [5] M. V. K. Chari and P. P. Sylvester, *Finite Elements in Electrical and Magnetic Field Problems*. New York: Wiley, 1980.
- [6] R. Palanisamy, thesis, Colorado State Univ., 1980 (unpublished), available Univ. Microfilms, #8028760.
- [7] C. V. Dodd, thesis, U. Tennessee, 1967, and Rep. ORNL-TM-1842, Oak Ridge National Lab.
- [8] C. V. Dodd and W. E. Deeds, *J. Appl. Phys.*, vol. 39, pp. 2829-2838, May 1968.
- [9] C. V. Dodd, W. E. Deeds, and J. W. Luquire, *Int. J. Nondestructive Testing*, vol. 1, pp. 29-90, 1969.
- [10] A. Shadowitz, *The Electromagnetic Field*. New York: McGraw-Hill, 1975, ch. 5, p. 206.
- [11] W. R. Smythe, *Static and Dynamic Electricity*. New York: McGraw-Hill, 1968, 3rd ed., ch. 8, p. 340.
- [12] E. B. Rosa and F. W. Grover, *Bulletin of the Bureau of Standards*, vol. 8, pp. 1-237, Jan. 1912.
- [13] W. R. Smythe, *Bulletin of the Bureau of Standards*, ch. 8, p. 340, Jan. 1912.
- [14] B. L. Allen, "Finite element modeling of pulsed eddy current phenomena," presented at DARPA/AFWAL Conf. on Quantitative NDE, Santa Cruz, CA, Aug. 7-12, 1983.
- [15] R. E. Beissner, M. J. Sablik, K. J. Krzywocz, and J. E. Doherty, *Review of Progress in Quantitative NDE*. D. O. Thompson and D. E. Chimenti, Eds. New York: Plenum, 1983, vol. 2B, pp. 1159-1172.

## APPENDIX C

### PROBE DESIGN STUDIES

#### Transmitter Impulse Response Calculations

The transmitter impulse response function  $E/I$  is the transient electric field induced in the specimen by a current pulse of zero width in the transmitter coil. The purpose of the calculations reported here was to determine the effects of transmitter geometry on induced fields, and thus to provide guidance in designing the transmitter to maximize the induced field at typical flaw locations.

Figure 43 shows the geometry used for all of the calculations in this Appendix. In some of the calculations, such as those presented in the next four figures, the effect of the flaw on the receiver response is not involved. Thus, the only parameters of concern at present are those pertaining to the transmitter geometry and position ( $\rho$ ,  $Z$ ) within the specimen. Values chosen for the initial study were the following:

Coil length ( $L_T$ )	= 3.2 mm (0.125")
Core radius ( $C_T$ )	= 1.02 mm (0.040")
Winding thickness ( $W_T$ )	= 1.01 mm (0.040")
Shield radius ( $S_T$ )	= 2.29 mm (0.090")
Lift off ( $Z_T$ )	= 0.42 mm (0.016")

Figures 44 through 48 show the effects of variations in transmitter geometry on the induced field. Ferrite core diameter is an important parameter, as illustrated in Figure 44, which shows how the induced field is broadened and increases in intensity as core size increases. Variations in coil-to-shield distance, on the other hand, produce only minor changes in the field, as shown in Figure 45. The next illustration, Figure 46, illustrates the expected lift-off effect; and the final figure, Figure 47, shows how the shield tends to focus the induced field, again as expected.

#### Flaw Impulse Response Function

The flaw impulse response function is proportional to the change in voltage in the receiver coil caused by a flaw,\* with the source current being a pulse of zero width in the transmitter coil. In the next two figures, flaw response calculations are presented as a function of flaw position, receiver winding configuration, and signal arrival time.

The detailed model treats a differential receiver with alternating positive and negative windings, as illustrated in Figure 43, where only one pair of windings is shown. To study the effect of winding configuration, calculations were performed as a function of the number of  $\pm$  winding pairs with the overall thickness of the winding held constant. Figure 48 shows a typical comparison, in this case between a coil with one  $\pm$  layer

\*In these calculations, as in Burrows' (9) model, the flaw is assumed to be small enough to be treated as a point scatterer. Signal amplitudes are normalized by dividing by the flaw volume.

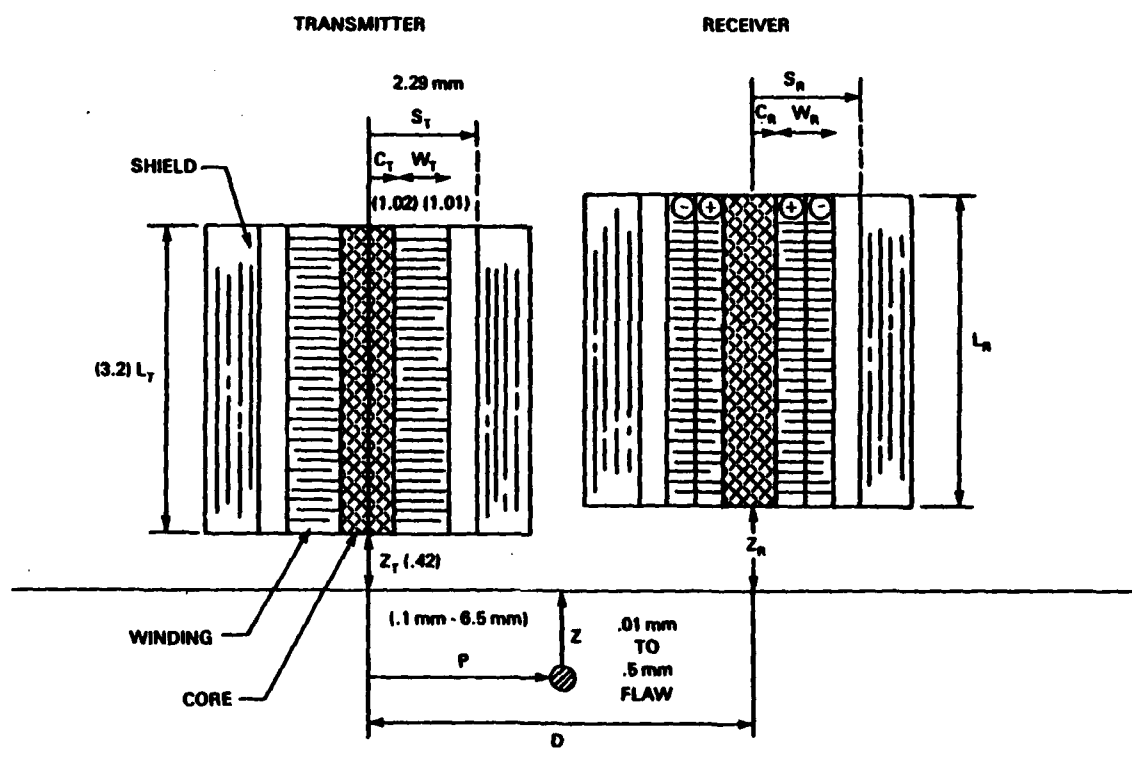


Figure 43. Geometry Used in Probe Design Studies

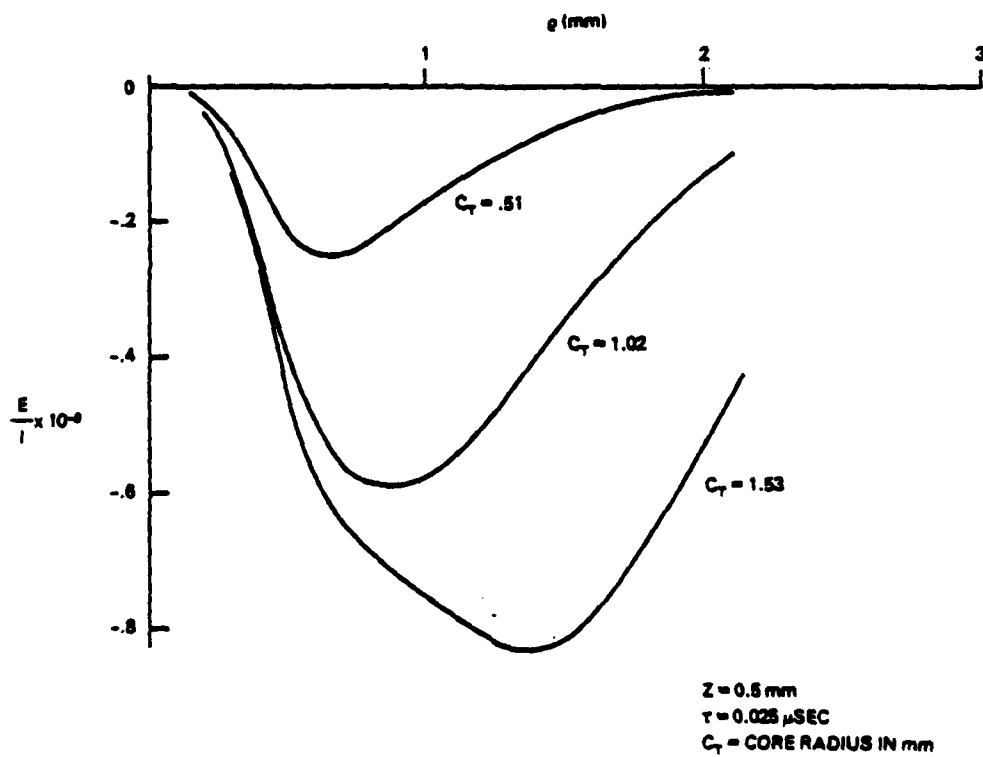


Figure 44. Effect of the Ferrite Core Size

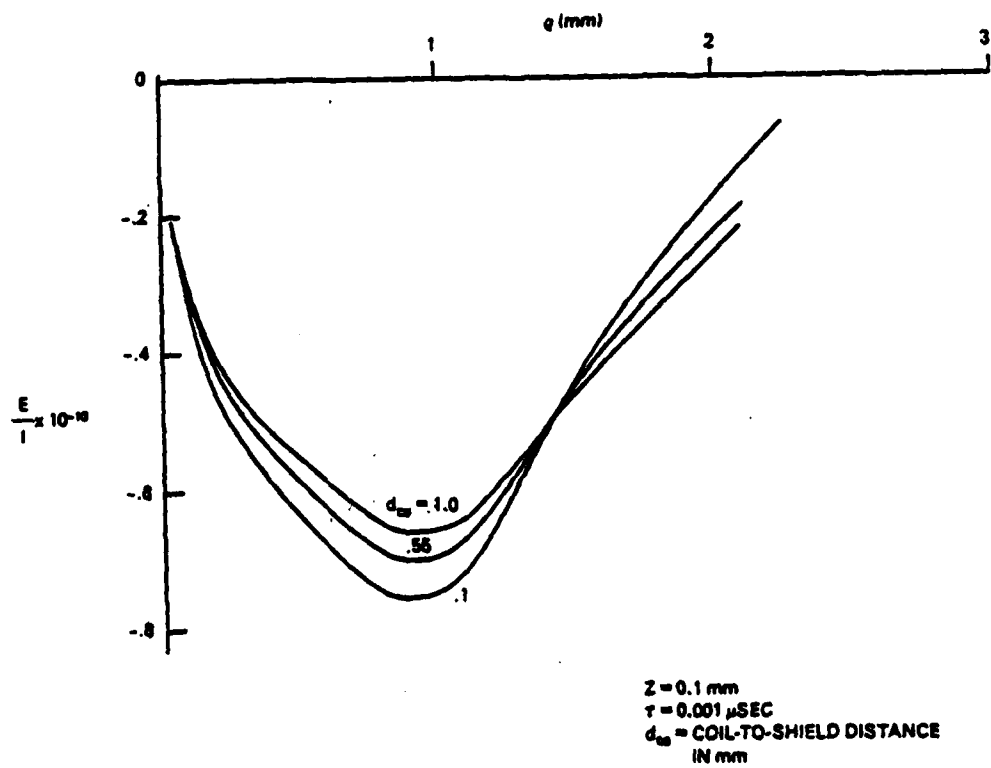


Figure 45. Effect of the Coil-to-Shield Distance

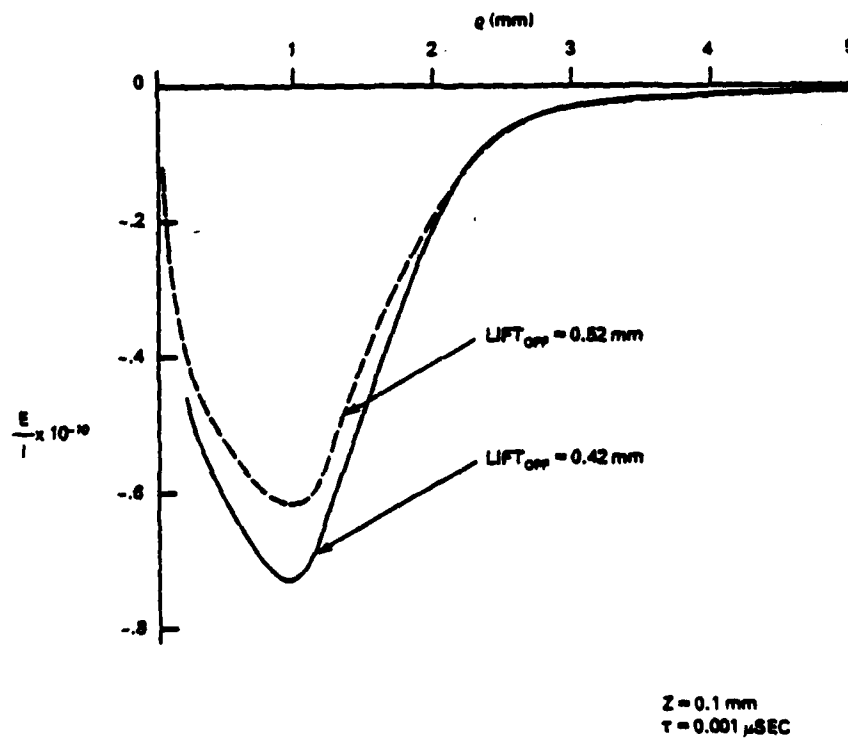


Figure 46. Effect of the Transmitter Liftoff

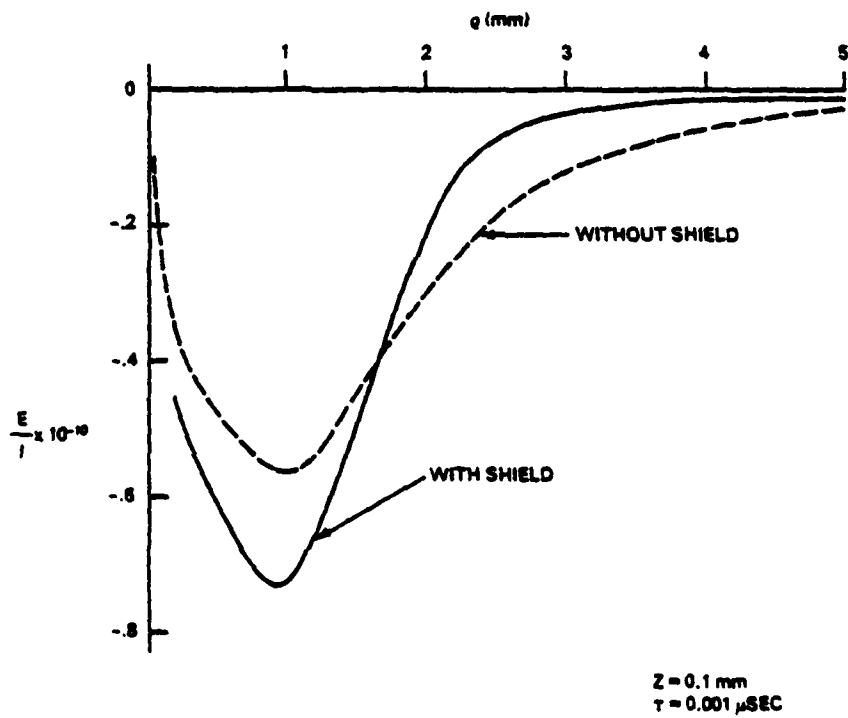


Figure 47. Effect of the Copper Shield

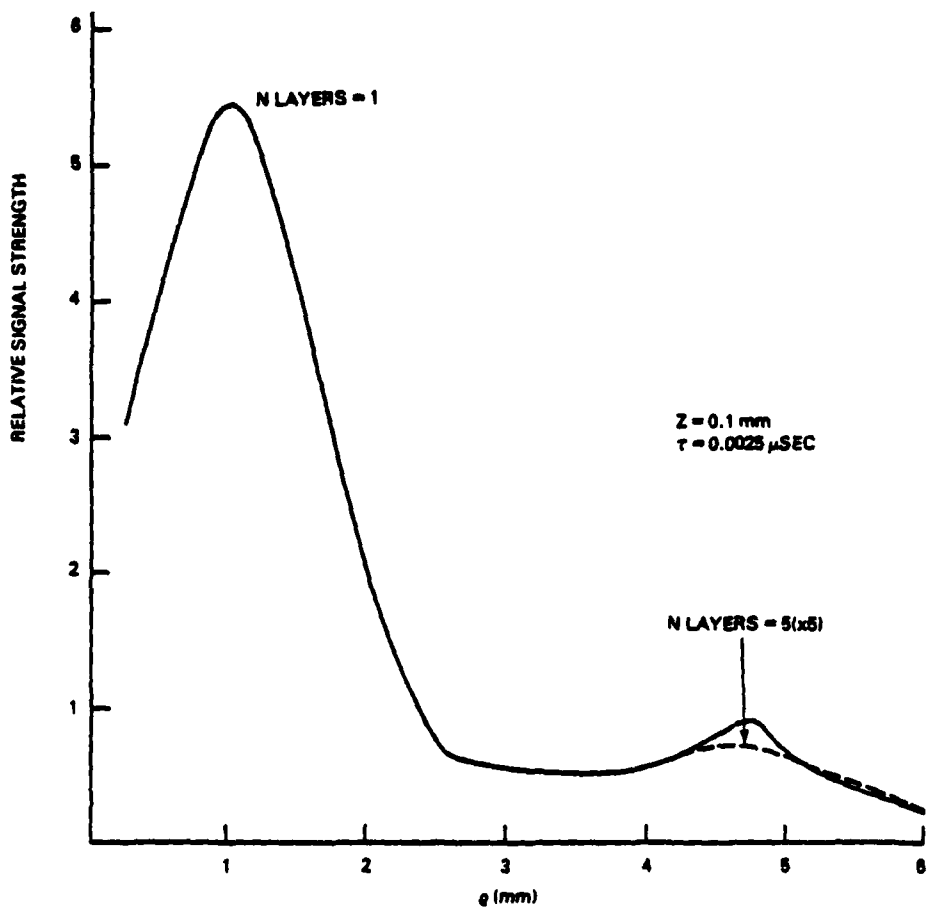


Figure 48. Flaw Response Functions for Differential Sensors

(NLAYERS = 1) and a coil with 5 such layers (NLAYERS = 5). As can be seen from these data, the principal effect of increasing the number of layers is to decrease the signal voltage (the NLAYERS = 5 curve has been multiplied by 5) with no improvement in flaw resolution. Another point illustrated here is that flaw response is greatest when the flaw is directly under the transmitter winding on the side nearest the detector ( $\rho \approx 1.0$  mm), in agreement with experimental observations. Similar calculations at different flaw depths show that the shape of the flaw response curve, as plotted in Figure 48, does not change significantly with flaw depth.

All calculations of the time-dependent signal produced in the receiver coil show certain common features, which are depicted in Figure 49. The impulse response signal is characterized by a very sharp positive peak followed by a series of secondary peaks of decreasing amplitude, increasing width, and alternating sign. Peak amplitudes and widths depend primarily on flaw depth and are not strongly influenced by  $\rho$ , the radial distance from the transmitter to the flaw. This behavior is illustrated by data presented in Figure 46 of the text for a short Gaussian excitation pulse. Peak arrival times showing the depth dependence are illustrated in Figure 47.

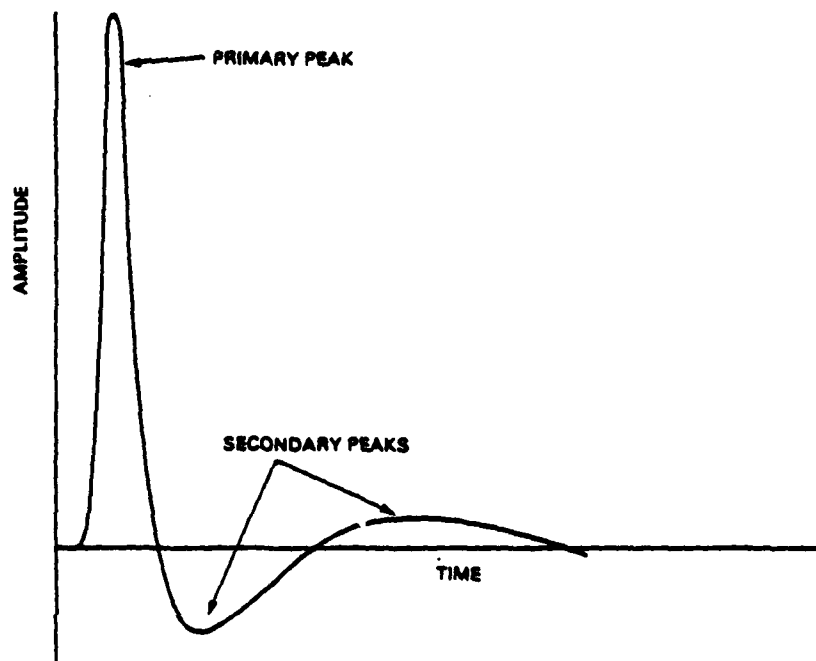


Figure 49. Schematic Illustration of Time-Dependent Signal Features

AD-A159 228

EXPLORATORY DEVELOPMENT ON ADVANCED EDDY CURRENT COIL  
EXCITATION AND SIGN. (U) SOUTHWEST RESEARCH INST SAN  
ANTONIO TX J L FISHER ET AL. APR 85 AFMAL-TR-85-4825

2/2

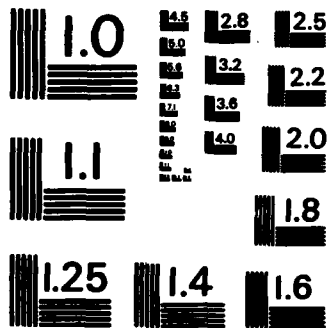
UNCLASSIFIED

F33615-81-C-5036

F/G 14/2

NL





MICROCOPY RESOLUTION TEST CHART  
NATIONAL BUREAU OF STANDARDS-1963-A

## APPENDIX D

### VOLTAGE TO CURRENT CONVERTER

The function of this circuit is to produce an output current whose amplitude is proportional to the amplitude of the input voltage. Figure 50 is a schematic diagram of the final version adapted for the pulse shaping experiments. Following is a brief description of the circuit.

The input voltage is amplified by amplifier AR1 and subsequently impressed on the base of transistor Q1. In the absence of a feedback current through resistor R13, the gain of AR1 is about 10; however, when an appropriate load is connected to the output of the circuit, a feedback current is generated that reduces the effective gain to about 5.

Transistor Q1 acts to convert the positive going voltage at its base into a negative going current in its collector circuit. The resistors connected in the emitter circuit perform a degenerative function that acts to make the conversion linear. The capacitor connected to the emitter enhances the high frequency response of transistor. The collector current passes through resistor R7 to produce a negative going voltage at the input of buffer amplifier AR2. AR2 is a unity gain, non-inverting amplifier with considerable drive capability. Its output drives the high susceptibility input gate of the HEXFET transistor Q2. The maximum drive voltage required at this point is about 10 volts (negative).

The HEXFET produces a current that is a function of the drive voltage at its gate. This current passes through the device connected between the output terminals and through the 2 ohm resistor R14. The output current of the HEXFET is not a linear function of its drive voltage. To correct for this non-linearity and, others that might be in the signal circuit, the voltage developed across R14 is used to produce a feedback current through R13. This current acts to modify the output of AR1 in a manner that will compensate for the circuit non-linearities and make the amplitude of the output current a proportional replica of the amplitude of the input voltage.

The circuit parameters have been chosen such that a two volt input pulse produces an output current pulse of approximately 2 amperes. The loop gain of the feedback circuit has been adjusted to give the nearest approach to a linear relationship between the input voltage and the output current that can be achieved without danger of oscillation or significant transient ringing. Better results might be achieved if the circuit is redesigned to use higher speed transistors.

#### NOTES:

- (1) The components connected in the source circuit of Q3 are carry-overs from the original circuit design and are of insignificant importance in its current application.

- (2) The transistor Q4 acts to provide a small bias current that overcomes and leakage current that might be present and assures that the voltage at the output terminals is zero under no drive conditions.
- (3) The transistors Q5 and Q6 act with associated circuitry to limit the high voltage current demand to approximately 20 mA.
- (4) Because Q2 acts as a current source, the value of the high voltage has no significant effect on the operation of the circuit.



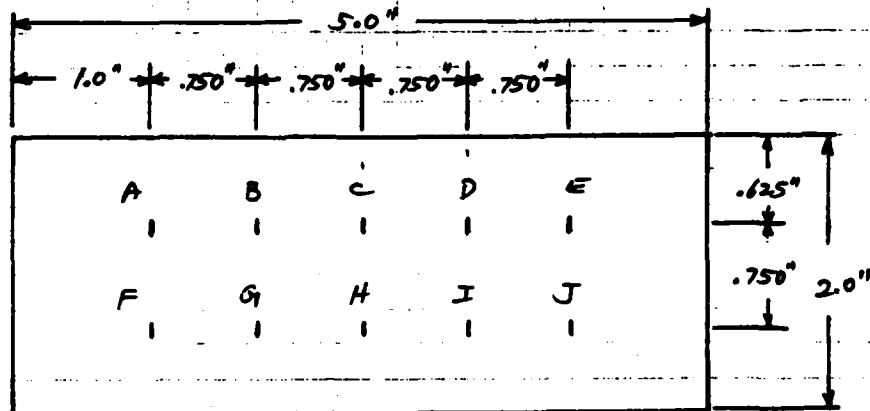
**APPENDIX E**  
**FLAW SPECIMENS**

**SOUTHWEST RESEARCH INSTITUTE  
DATA SHEET**

SUBJECT Ribbed Eddy Current  
Response Standards

SHEET NO. 1 OF 4 SHEETS  
PROJECT 17-6633-204  
DATE 11/17/81  
BY Z.J. Kay/w022

SURFACE FLAW DETECTION STANDARDS



- A - 0.050" L x 0.005" W x 0.005" D
- B - 0.040" L x 0.005" W x 0.005" D
- C - 0.030" L x 0.005" W x 0.005" D
- D - 0.020" L x 0.005" W x 0.005" D
- E - 0.010" L x 0.005" W x 0.005" D
  
- F - 0.010" L x 0.005" W x 0.003" D
- G - 0.020" L x 0.005" W x 0.010" D
- H - 0.030" L x 0.005" W x 0.015" D
- I - 0.040" L x 0.005" W x 0.020" D
- J - 0.050" L x 0.005" W x 0.025" D

MATERIALS : Zn 100 and Ti-64 (Specimen thickness of 0.250")

Quantity : One of each

PC-4



**SOUTHWEST RESEARCH INSTITUTE  
DATA SHEET**

SUBJECT Pulsed Eddy Current  
Reference Standards

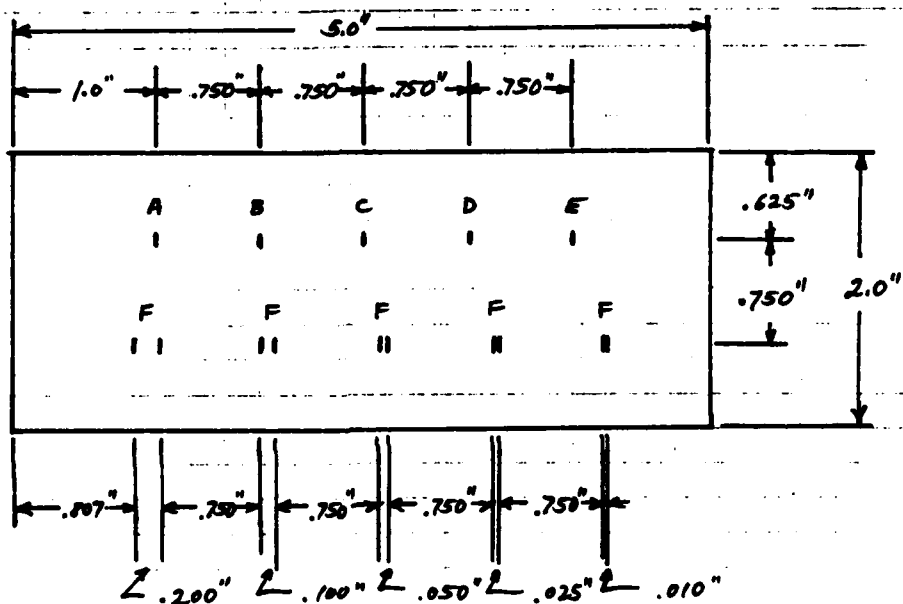
SHEET NO. 2 OF 4 SHEETS

PROJECT 17-6633-254

DATE 11/17/81

BY K.J. KREYWOSZ

SURFACE / SEPARATION RESOLUTION STANDARDS



- A - 0.010" L x 0.005" W x 0.050" D
- B - 0.010" L x 0.005" W x 0.035" D
- C - 0.010" L x 0.005" W x 0.020" D
- D - 0.010" L x 0.005" W x 0.005" D
- E - 0.010" L x 0.005" W x 0.003" D
- F - 0.050" L x 0.005" W x 0.035" D

NOTE: Separation distance is from edge-to-edge and not from center-to-center.

MATERIALS: In-100 and Ti-64 (Specimen thickness of 0.250")

Quantity: One of each

PC-4

THE MARK OF RELIABILITY



**APPLIED TEST SYSTEMS, INC.**

Saxonburg Blvd. • Saxonburg, Pa. 16056

Phone: 412/265-1546 • 265-3330

Telex: ATS SXBG 86-6727

**EDM NOTCH CERTIFICATION  
CERTIFICATE OF ACTUAL DIMENSIONS OF MACHINED DEFECTS**

Order No. 8541A

ITEM	STANDARD Surface/Separation Resolution	LOCATION	Notch Dimensions, (In.) MM					
			Length		Width		Depth	
			Nominal	Actual	Nominal	Actual	Nominal	Actual
		A	.010	.0104	.005	.0052	.050	.0517
		B	.010	.0106	.005	.0051	.035	.0354
		C	.010	.0107	.005	.0056	.020	.0186
		D	.010	.010	.005	.0052	.005	.0054
		E	.010	.0098	.005	.0048	.003	.0036
		F1	.050	.0502	.005	.0054	.035	.035
		F2	.050	.0501	.005	.0057	.035	.0331
		F3	.050	.0496	.005	.0056	.035	.0356
		F4	.050	.0496	.005	.0054	.035	.0357
		F5	.050	.0505	.005	.0056	.035	.0346
		F6	.050	.0504	.005	.0055	.035	.0335
		F7	.050	.0504	.005	.0056	.035	.035
		F8	.050	.0506	.005	.0053	.035	.0345
		F9	.050	.0486	.005	.0056	.035	.0336
		F10	.050	.0486	.005	.0057	.035	.0343

Customer Southwest Research Institute Purchase Order No. 142845W

Specification \_\_\_\_\_ Drawing No. 17-6633-204 Sheet 2 of 4

The above certified notches were machined using electrical discharge machining equipment. All measurements were arrived at using plastic compound replication, and optical techniques where applicable.

Date 1/19/82 Name John Currie Signature *John Currie*

zk

**SOUTHWEST RESEARCH INSTITUTE  
DATA SHEET**

SUBJECT Pulsed Eddy Current  
Reference Standards

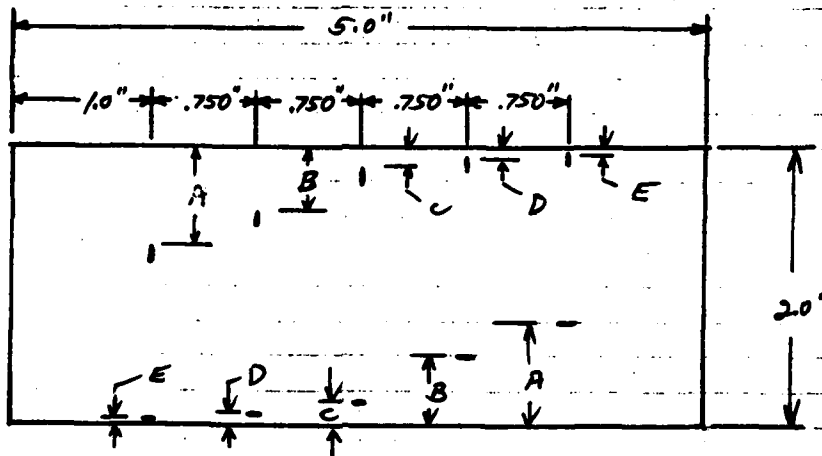
SHEET NO. 4 OF 4 SHEETS

PROJECT 17-6633-204

DATE 11/17/81

BY K.J. Keyworth

EDGE RESOLUTION STANDARD



All notch dimensions are 0.050" L x 0.005" W x 0.035" D

A	-	0.750"	} edge distance
B	-	0.500"	
C	-	0.200"	
D	-	0.100"	
E	-	0.050"	

NOTE: Specified edge distances are measured edge-to-edge

MATERIALS: Inconel 100 and Ti-64 (specimen thickness of 0.250")

Quantity: One of each

PC-4

THE MARK OF RELIABILITY



**APPLIED TEST SYSTEMS, INC.**

Saxonburg Blvd. • Saxonburg, Pa. 16056  
 Phone: 412/265-1546 • 265-3330  
 Telex: ATS SXBG 86-6727

**EDM NOTCH CERTIFICATION  
 CERTIFICATE OF ACTUAL DIMENSIONS OF MACHINED DEFECTS**

Order No. 8541A

ITEM	STANDARD	LOCATION	Notch Dimensions, In. MM						
			Length		Width		Depth		
			Nominal	Actual	Nominal	Actual	Nominal	Actual	
	Edge Resolution								
		A1	.050	.0496	.005	.005	.035	.0353	
		B1	.050	.0495	.005	.0051	.035	.0349	
		C1	.050	.0498	.005	.0055	.035	.034	
		D1	.050	.050	.005	.008	.035	.0365	
		E1	.050	.0505	.005	.0054	.035	.0347	
		A2	.050	.0506	.005	.0052	.035	.033	
		B2	.050	.0509	.005	.005	.035	.035	
		C2	.050	.0504	.005	.0054	.035	.0332	
		D2	.050	.0507	.005	.0053	.035	.0375	
		E2	.050	.050	.005	.0054	.035	.0342	

Customer Southwest Research Institute Purchase Order No. 14284SW

Specification \_\_\_\_\_ Drawing No. 17-6633-204 Sheet 4 of 4

The above certified notches were machined using electrical discharge machining equipment. All measurements were arrived at using plastic compound replication, and optical techniques where applicable.

Date 3/19/82 Name John Curtis Signature *John Curtis*

alk

**END**

**FILMED**

**10-85**

**DTIC**